Theoretical Investigations on the Electrochemical Fluorination Reaction in the Simons Process

Inaugural Dissertation

to obtain the academic degree
Doctor rerum naturalium (Dr. rer. nat.)

submitted to
the Department of Biology, Chemistry and Pharmacy
of Freie Universität Berlin

by
Stefan Mattsson
from Västerhaninge
2020

This work was conducted under the supervision of
Prof. Dr. Beate Paulus (Freie Universität Berlin)
from May 2016 until May 2020

First reviewer:	Prof. Dr. Beate Paulus
Second reviewer:	Prof. Dr. Sebastian Hasenstab-Riedel
Date of defense:	July 6, 2020

Selbstständigkeitserklärung

Hiermit bestätige ich, dass ich die vorliegende Arbeit selbständig und nur unter Verwendung der angegebenen Literatur und Hilfsmittel erstellt habe. Außerdem versichere ich, dass diese Arbeit bei keinem früheren Promotionsverfahren eingereicht wurde.

Today was a good day

– O'Shea "Ice Cube" Jackson

Abstract

Perfluorinated compounds are found in a wide array of technical applications associated with modern society. For instance, perfluorinated compounds are used as various surfactants, or as cooling agents in the production of electronics. The Simons process is applied in industry for the synthesis of such compounds. The experimental setup consists of a Ni anode, a cathode (often Ni or Fe) and anhydrous hydrogen fluoride (HF) as fluorine source and solvent, in which organic substrates are dissolved. A cell potential of around 4.5-6.0 V is applied, which drives the fluorination reaction.

Despite the prevalence in industrial applications, the chemical mechanism of the Simons process has still not been fully understood. There is evidence that the electrochemistry only involves the oxidation of the Ni anode and subsequent binding of fluoride ions from the solvent, leading to a reactive nickel fluoride film (Ni_xF_y) forming at the anode. The film is of unknown structure and chemical composition, although it is believed to include highly oxidized Ni^{3+} or Ni^{4+} centers.

In this thesis, the structure and formation of the Ni_xF_y film is considered. Using a model system involving Ni(111) surfaces and layers of explicit solvent molecules, results from DFT calculations indicate that a metallic Ni anode is easily oxidized at very low cell potentials. Furthermore, the work contains studies on the interface of a Ni(111) surface and a single HF molecule, in order to gain knowledge of the adsorption mechanism of the molecule in a non-electrochemical environment.

A good starting point for models of Ni_xF_y films are the already known binary nickel fluorides. Particularly NiF_3 is of interest because of its strongly oxidizing properties and proposed role in the Simons process. The series of magnetic 3d metal trifluorides from TiF_3 to NiF_3 is considered with hybrid DFT and DFT+U methods. NiF_3 is characterized as an antiferromagnetic wide-bandgap (3.3 eV) semiconductor. Hence, the compound is expected to be less electrically insulating than the Mott-Hubbard insulator NiF_2 (bandgap 5 eV). Anodes are typically passivized at cell potentials below ca. 3 V, due to the formation of an insulating NiF_2 film. In this thesis, the anode is structurally modeled as different NiF_2 surfaces. Using hybrid DFT calculations and thermodynamical considerations for the cell potential, the oxidation of surface Ni^{2+} to Ni^{3+} is calculated to proceed at potentials around 3.1 V, which is in good agreement with oxidation features in cyclic voltammetry experiments.

Kurzzusammenfassung

Perfluorinierte Verbindungen kommen in vielen technischen Anwendungen vor, die mit unserer modernen Gesellschaft verbunden sind. Perfluorinierte Verbindungen werden zum Beispiel als Tenside verwendet, oder als Kühlmittel, die bei der Herstellung elektronischer Geräte notwendig sind. Der Simons-Prozess wird häufig in der Industrie benutzt, um solche Verbindungen zu synthetisieren. Die experimentelle Einrichtung besteht aus einer Ni-Anode, einer Kathode (typisch Ni oder Fe) und wasserfreiem Fluorwasserstoff (HF), der als Fluor-Quelle und Lösungsmittel dient, in das die organischen Reaktanten aufgelöst werden. Es wird eine Zellspannung von 4.5-6.0 V benutzt, um die Fluorierungsreaktion voranzutreiben.

Trotz der Vielfalt an industriellen Anwendungen, ist der chemische Mechanismus des Simons-Prozesses nicht komplett aufgeklärt worden. Es ist bereits literaturbekannt, dass die elektrochemischen Schritte die Oxidation der Ni-Anode betreffen, mit folgendem Binden von Fluorid-Ionen aus dem Lösungsmittel, so dass ein reaktiver Nickel-Fluorid-Oberflächenfilm (Ni_xF_y) an der Anode gebildet wird. Die Struktur und chemische Zusammensetzung des Filmes sind immer noch unbekannt, obwohl hoch-oxidierte Ni^{3+}- oder Ni^{4+}-Stellen als mögliche Komponente des Filmes vorgeschlagen worden sind.

Diese Dissertation behandelt die Struktur und Entstehungsmechanismen des Ni_xF_y-Films. Mittels eines Grenzflächenmodells bestehend aus Ni(111)-Oberflächen und Schichten explizierter Lösungsmittelmoleküle, wird durch DFT-Berechnungen indiziert, dass eine metallische Ni-Anode einfach oxidiert wird, auch bei sehr kleinen Zellspannungen. Außerdem wird das Gränzflächensystem einer Ni(111)-Oberfläche und eines einzelnen HF-Moleküls untersucht, um Einsichten zu erhalten, über den Adsorptionsmechanismus des Moleküls in einer nicht-elektrochemischen Umgebung.

Ein guter Ansatzpunkt für Ni_xF_y-Modelle sind die schon bekannten binären Nickelfluoride. Besonders interessant ist NiF_3, wegen seiner stark oxidierenden Eigenschaften und vorgeschlagenen Rolle im Simons-Prozess. Die Serie der magnetischen 3d-Übergangsmetalltrifluoride wird mit hybrid-DFT und DFT+U Methoden untersucht. NiF_3 lässt sich als antiferromagnetischer Halbleiter mit einem breiten Bandabstand (3.3 eV) charakterisieren. Deswegen wird erwartet, dass NiF_3 weniger elektrisch isolierend wirkt, im Vergleich zu dem Mott-Hubbard-Isolator NiF_2 (Bandlücke 5 eV). Anoden werden typischerweise passiviert im Zellspannungsbereich bis zu etwa 3 V, wegen eines entstehenden isolierenden NiF_2-Films. In dieser Dissertation wird die Anodenstruktur als verschiedene NiF_2-Oberflächen dargestellt. Durch hybrid-DFT-Berechnungen und thermodynamische Modelle für die Zellspannung, wird berechnet, dass die Oxidation von Ni^{2+} an der Oberfläche zu Ni^{3+} bei der Zellspannung 3.1 V stattfindet, was gut mit Cyclovoltammetrieversuchen übereinstimmt.

List of publications

Paper A

"Density Functional Theory Calculations of Structural, Electronic, and Magnetic Properties of the 3d Metal Trifluorides MF_3 (M = Ti-Ni) in the Solid State"
Mattsson, S. and Paulus, B., *J. Comput. Chem.*, 2019, **40**, 1190–1197.
DOI: 10.1002/jcc.25777

Paper B

"A theoretical study on the binding and electrolytic splitting of hydrogen fluoride on Ni(111) and Ni(211)"
Mattsson, S. and Paulus, B., *Phys. Chem. Chem. Phys.*, 2020, **22**, 4407–4415.
DOI: 10.1039/c9cp06348j

Paper C

"Combining theory and experiment to characterize the voltammetric behavior of nickel anodes in the Simons process"
Mattsson, S.; Senges, G.; Riedel, S. and Paulus, B., *Chem. Eur. J.*, 2020, accepted manuscript.
DOI: 10.1002/chem.202000881

Paper D

"Ab initio molecular dynamics studies on the adsorption of hydrogen fluoride on Ni(111)"
Mattsson, S. and Paulus, B., submitted manuscript.

Contents

Chapter 1

Introduction

Fluorine is very special among the elements, which is reflected in its entry of the Merriam-Webster's Collegiate Dictionary: "a nonmetallic gaseous chemical element of the halogen group with atomic number 9 that readily forms compounds with almost all other elements including some noble gases".[1] The most electonegative of all elements, fluorine has the unique property of stabilizing some extreme oxidation states such as Au^{6+}, Ag^{3+} and Kr^{2+}.[2,3] Well reduced, fluorine forms some of the strongest single bonds in chemistry, with the C–F bond as an important example.[4] The chemistry of fluorine-containing compounds is rich, and applications are found in many areas such as pharmaceutics, material sciences, agricultural chemistry and electronics.[5,6]

The field of organofluorine chemistry considers synthesis, reactivity and properties of organic compounds that include one or more fluorine atoms. If all C–H bonds in a molecule are replaced with C–F bonds, the molecule is said to be perfluorinated. Perfluorinated molecules are generally highly stable, and, due to their particular hydro- and lipophobic properties, are widely used as for example surfactants, lubricants, artificial blood substitutes and solvents.[7,8] Although in principle realizable, perfluorination reactions with elemental F_2 often involve issues with respect to selectivity and product decomposition, and are affiliated with high risks due to the strongly oxidizing properties of F_2. Therefore, perfluorination reactions are often performed with an intermediate reagent with which the organic substrate reacts in a more controlled manner. The fluoride ligand is capable of stabilizing high oxidation states of *e.g.* cobalt or nickel,[2] forming metal fluorides which are reactive with respect to perfluorination but easier to handle. In the Fowler process, perfluorination reactions with CoF_3 are performed in two steps: 1) oxidation of CoF_2 with gaseous F_2 and 2) perfluorination of the organic substrate in a controlled manner with CoF_3.[9] However, the usage of F_2 is not completely eliminated.

In 1949, in a series of papers, Joseph H. Simons and coworkers reported a new method of electrochemical fluorination (ECF) which completely left out F_2 from the

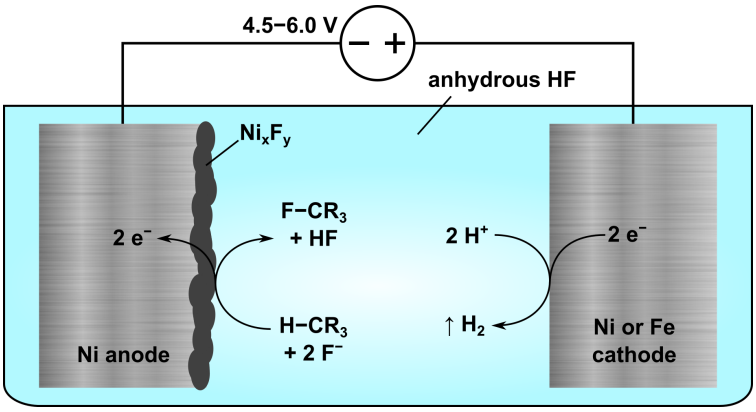

Figure 1.1: Reaction scheme of an electrochemical fluorination cell according to Simons. The reaction stoichiometry refers to the fluorination of one C–H bond. The substituents R are not specified, but often include heteroatoms.[8] A Ni_xF_y film is formed on the anode as an intermediate in the perfluorination reaction.

reaction scheme.[10–14] The method was named the Simons process and quickly became the workhorse in industry for the production of perfluorinated molecules.[15] A schematic of the overall reaction in a Simons cell is shown in Fig. 1.1. The key feature is the Ni anode where the fluorination takes place. Essentially, the oxidation of the organic substrate with elemental F_2 has been replaced by oxidation by the electric current. The fluorine source is due to the electrolysis of anhydrous HF (aHF). Cell potentials around 4.5-6.0 V are typically used in industry, but the cell may function also outside this potential window.[8] The cathode material is of lesser importance, as it simply catalyzes the hydrogen evolution reaction. Typically, Ni or Fe is used.

The mechanism of the Simons process has been subject to debate ever since its invention. Especially the oxidation step has been discussed extensively, in particular the role of the organic substrate. In addition, the microscopic structure of the Ni anode in a working Simons cell still to this day has not been fully resolved. Contributions to the debate on the mechanism include

a) Oxidation of F^- to atomic F or molecular F_2 at the anode, which subsequently fluorinates the organic substrate[16]

b) Formation of highly oxidized nickel (III) or (IV) fluorides as intermediates. The fluorination of the substrate occurs in a second, non-electrochemical step from the reactive fluorides[17]

c) Formation of an unreactive NiF_2 film with F or F_2 weakly coordinated to it. These activated fluorine centers react with the substrate in a second step[18]

d) Direct single-electron oxidation of the organic substrate on the Ni surface leading to the formation of an organic radical cation. After deprotonation of the radical cation, a second oxidation step takes place, forming a carbocation. Finally, F^- binds to the carbocation.[19]

In 1995, Sartori *et al.* reported the crucial finding that the fluorination of the organic substrate occurred even after the external potential had been disconnected.[20] The cell was pre-electrolyzed at 5 V in pure aHF. This suggests that the electrochemical steps do not involve the organic substrate, but rather lead to the formation of an strong fluorinating agent as an intermediate (*cf.* CoF_3 in the Fowler process). Hence, mechanisms a) and d) may be discarded.

Typically, in an operating ECF cell, a black or brown film is formed on the surface of the anode, with or without organic molecules in the electrolyte (see Fig. 1.1).[21] If the experiment is aborted, the film decomposes to NiF_2, more rapidly so when exposed to air. Because of its instability, the film has never been structurally characterized, why I will label it Ni_xF_y. The dark color and low crystallinity indicate some degree of amorphicity in the film. In accordance with the aforementioned experiment by Sartori *et al.*, Ni_xF_y is the active fluorinating agent in the Simons process. Hence, if the reaction mechanism is to be fully understood, the structure of the Ni_xF_y film must be further elucidated. Of the two remaining mechanisms, b) is most widely accepted, although only indirect arguments have been made, based on cyclovoltammetry (CV) measurements,[18,22–24] reactivities and stabilities of known nickel fluorides,[8,21,25] or analyses of the perfluorinated products.[26,27]

The aim of this thesis is to gain insight on the structure of the Ni_xF_y film, using theoretical arguments. Through density functional theory (DFT) methods, calculations of many-body quantum systems are possible in an approximate fashion, at affordable computational costs.[28] DFT is widely applied in calculations of electronic structures – a principal quantity in the description of the chemical phenomena of matter. Unfortunately, direct atomistic-scale simulations on amorphous systems are affiliated with the necessity of a large number of atoms, due to the low degree of translational symmetry. Furthermore, each Ni center may exhibit different spin configurations (high or low) and magnetic couplings between Ni centers need to be considered explicitly. The large number of degrees of both nuclear and electronic freedom means straightforward simulations are either too expensive or numerically complex to be treated by quantum-chemical methods.

This work is built around two approaches for the construction of Ni_xF_y models, with structurally known compounds as starting point (see Fig. 1.2). The approaches consider the film structure at different stages in the process. Here, an analogy to reported cyclovoltammograms is useful to distinguish between the two. At anodic cell potentials below 3 V, no current is detected, except for a small peak around 0.1

V which is reported in some studies.[22,23] In this low-potential region, the film is not active with respect to perfluorination. In the first approach, interfaces of metallic Ni surfaces with F and/or HF adsorbates are considered. The lower degree of fluorination means these Ni/F/HF systems are possible representations of the initial oxidation of the Ni anode, and hence the low-potential region of the CV experiments. The first approach is closely related to heterogeneous catalysis and chemistry at metal surfaces, a field where DFT is routinely employed for metal/small molecule interfaces.[29–33] The Ni/F/HF approach is employed in **Paper B**, which considers the electrochemical interfaces at the metallic electrodes in a Simons cell. The electrolytic splitting of HF is modeled as a function of cell potential. Furthermore, **Paper D** considers the six-dimensional potential energy surface of a single HF molecule on a Ni(111) surface, and pathways for non-electrochemical adsorption of the molecule.

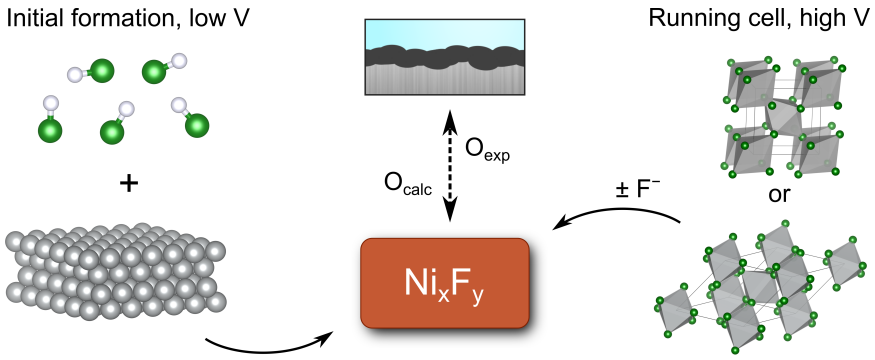

Figure 1.2: The two general approaches made to construct models for Ni_xF_y. The lower amount of fluorine at the initialization of the process is represented by fluorination of metallic Ni surfaces (left). The higher fluorine content in the active fluorinating film of a running cell is modeled by considering known nickel fluorides and varying the amount of fluorine (right). In a CV experiment, left and right correspond to the low- and high-potential region, respectively. The Ni_xF_y models are evaluated by comparison of calculated and experimental observables (O).

CV experiments consistently include sharp increases in current at cell potentials above 3 V, after which the active film may be visually observed.[18,22–24] The fluorine content increases in the higher oxidized films and deems the previous model improper. Instead, known crystalline nickel fluorides constitute the starting point for Ni_xF_y models. For this, NiF_2 and NiF_3 are the best candidates since the crystal structures are available fully for the former,[34] and partially for the latter.[35] NiF_4 and Ni_2F_5 have also been synthesized, but are structurally unknown.[35,36] By construction of supercells of the stoichiometric compounds, the number of fluorine atoms may be varied, resulting in various Ni_xF_y structures with Ni centers of different valency. This allows for a detailed assessment on the electronic and magnetic degrees of freedom.

Due to the open-shell nature and localized electrons of the metal ions in these compounds, special care must be taken regarding the selection of the exchange-correlation functional. Functionals with a Hubbard-like correction term for correlated Coulomb interaction (DFT+U) or hybrid functionals are necessary even for qualitatively correct band structures.[37] The DFT methods employed are often found in studies on strongly correlated magnetic insulators or semiconductors,[38–40] and heterogeneous metal oxide or fluoride catalysis.[41–44] In **Paper A**, we start off by proposing complete structural parameters for NiF_3 from DFT calculations. Furthermore, the electronic and magnetic properties of the compound are evaluated and serve as reference for further Ni^{3+} motifs. In **Paper C**, surface Ni_xF_y models are constructed from NiF_2 surfaces. Addition of fluorine means the surfaces are of mixed valence between Ni^{2+} and Ni^{3+}. Through thermodynamical arguments, cell-potential-dependent stabilities of trivalent Ni are calculated.

This thesis summarizes the first computational efforts for the description of the Ni_xF_y film as it occurs in the Simons process. The various aspects of the film and its formation, as discussed above, require significantly different quantum-chemical methods, ranging from dispersively bound single molecules to strongly correlated magnetic insulators and semiconductors. In Chapter 2, I discuss the theoretical foundations and their affiliated possibilities and limitations. Several of the methods are conceivably scalable to more complex representations of Ni_xF_y, with the limiting factor being the accuracy or applicability of the quantum-chemical method itself. Further on, Chapter 3 contains references to the results, in the form of the published **Papers A**, **B**, the accepted manuscript of **Paper C**, as well as the submitted manuscript for **Paper D**. In the papers and the submitted manuscript, the reader finds details regarding structural models, calculated properties, discussion of the results as well as computational specifications. Finally, I summarize the findings during this work in Chapter 4.

Chapter 2

Theory and methods

Chemical processes – whether occurring in laboratories, industries, biological systems or in everyday devices – often involve a number of atoms in the order of Avogadro's constant (10^{23}). For example, the electrochemical cells that are the topic of this thesis are macroscopic objects. We know, however, that the prerequisites for chemical processes to occur must be understood in terms of electrons, be it their distribution or motion in a molecule, or their transfer between molecules, leading to a chemical reaction. The nature of electrons as microscopic particles implies that the scale needs to be reduced greatly in order to gain the fundamental knowledge of chemical reactions, which are typically observed in the greater ensemble of particles. Also important for the understanding of chemical reactions is the motion of nuclei, which may, for example, be involved in transfers between molecules or in vibrational motion. Depending on nuclear mass and specific situation, nuclear motion may be treated approximately quantum-mechanically (*e.g.* the quantum harmonic oscillator approximation) or be treated simply as static point charges.

The mass of an electron is approximately two thousands to that of the lightest atomic nucleus, and this fact has a great consequence on the theories needed to describe the elemental physics of electrons. Due to its small mass and spin, an electron displays a significant wave-like behavior and must be described by quantum theory. If the scientific question asked involves chemistry (molecules, crystals, surfaces *etc.*), the quantum mechanical approach is often referred to as quantum chemistry. Through quantum chemical methods, electronic structures of atomistic-scale systems may be calculated with ever-increasing accuracy, especially since the advent of high-performance computing. In the following Section 2.1, I describe the fundamentals of quantum-chemical electronic structure calculations. This is built upon in Section 2.2 in the case of periodic systems, such as solids and surfaces.

The broader discipline of theoretical chemistry deals with the construction of models for various problems in chemistry. All such models in this thesis are founded

in, and extend on quantum chemical calculations. In Sections 2.3 and 2.4, I present methods for the treatment of the complex electronic and magnetic structures that are present in the chemical species that play a role in the Simons process. Further on, in Section 2.5, I describe the necessary set-up of quantum chemical calculations in order to model surface reactions and structures, with macroscopic effects treated by thermodynamics. This is extended on for specific electrode processes, in Section 2.6, where environment effects are treated with electrochemical models in coherence with the underlying quantum-chemical calculations.

2.1 Electronic structure methods

2.1.1 Hartree-Fock theory

The formalism of quantum mechanics is founded in the Schrödinger equation.[45] It introduces the wave function as a function that contains all information about a system. The time-dependent Schrödinger equation has the illusively simple form

$$\hat{H}\Phi_j(t) = i\hbar\frac{\partial}{\partial t}\Phi_j(t) \tag{2.1}$$

which contains the Hamilton operator $\hat{H}$, the time-dependent wave function $\Phi_j(t)$ of the state j, the time t, the imaginary unit i and the reduced Planck constant $\hbar$. If the system is static with respect to time, the time-independent Schrödinger equation may be written, in atomic units, as

$$\begin{aligned}\hat{H}\Psi_j = -\sum_{i=1}^{N}\frac{1}{2}\nabla_i^2 - \sum_{A=1}^{M}\frac{1}{2m_A}\nabla_A^2 - \sum_{i=1}^{N}\sum_{A>i}^{M}\frac{Z_A}{r_{iA}} + \sum_{i=1}^{N}\sum_{j>i}^{N}\frac{1}{r_{ij}} + \sum_{A=1}^{M}\sum_{B>A}^{M}\frac{Z_A Z_B}{R_{AB}} \\ = (\hat{T}_\mathrm{e} + \hat{T}_\mathrm{N} + \hat{V}_\mathrm{eN} + \hat{V}_\mathrm{ee} + \hat{V}_\mathrm{NN})\Psi_j = E_j\Psi_j\end{aligned} \tag{2.2}$$

Ψ_j denotes the time-independent (static) wave function. In quantum chemistry, its elements are typically coordinates of electrons, $\mathbf{r}_i$, and nuclei, $\mathbf{R}_A$, as well as electron spin variables ω_i (if hyperfine coupling effects are neglected, nuclear spin variables are usually omitted). For most systems of interest, this results in a high-dimensional function Ψ_j. In eq. (2.2), r and R refer to particle distances, where subscripts i/j, A/B denote electrons and nuclei, respectively. m_A and Z_A are the mass and charge of nucleus A relative to an electron and ∇ is the Laplacian of a particle. Contributions of kinetic and potential energies to the Hamiltonian are divided into kinetic energies $\hat{T}$ of electrons (e) and nuclei (N) and potential energy $\hat{V}$ of all possible Coulomb

interactions (eN, ee, NN). The eigenvalue of the equation is the energy E_j of the state.

Finding analytic solutions to the differential equation (2.2) is possible only for systems with either one particle or two-particle systems that may be described in terms of a reduced mass (*e.g.* particle in a box, H, He^+, Li^{2+}, the quantum harmonic oscillator in specific coordinates). In the Born-Oppenheimer approximation, the large mass difference between electrons and nuclei is exploited.[46] The nuclear and electronic degrees of freedom are separated and an electronic wave function $\Psi_{\text{elec}}(\mathbf{r};\mathbf{R})$ is formulated, which contains the electronic coordinates $\mathbf{r}$ explicitly and the nuclear coordinates $\mathbf{R}$ parametrically

$$\hat{H}_{\text{elec}}\Psi_{\text{elec}} = (\hat{T}_{\text{e}} + \hat{V}_{\text{eN}} + \hat{V}_{\text{ee}})\Psi_{\text{elec}} = E_{\text{elec}}\Psi_{\text{elec}} \tag{2.3}$$

The nuclei are considered static ($\hat{T}_{\text{N}} = 0$) when solving for Ψ_{elec}. Within the Born-Oppenheimer approximation, potential energy surfaces (PES) are often sampled for varying $\mathbf{R}$ through static calculations, according to eq. (2.3), in order to calculate *e.g.* (ro)vibrational properties or minimum energy paths in chemical reactions.

The electronic wave function (from now on simply Ψ) still has a dependence on all N electronic degrees of freedom and requires further simplification. Ψ is divided into N single-electron functions $\chi(\mathbf{x})$, *i.e.* spin orbitals.[47] According to Pauli, any wave function needs to fulfill the condition of antisymmetry upon the exchange of two electrons, due to electrons being fermions ($\Psi(\mathbf{x}_1,\mathbf{x}_2) = -\Psi(\mathbf{x}_2,\mathbf{x}_1)$).[48] $\mathbf{x}$ is referred to as the spin-coordinate and contains information of the spatial coordinate and spin of an electron. This requirement is satisfied by approximating Ψ as a determinant of spin orbitals, according to Slater[49]

$$\Psi(\mathbf{x}_1,\mathbf{x}_2,...,\mathbf{x}_N) = \frac{1}{\sqrt{N!}}\begin{vmatrix} \chi_1(\mathbf{x}_1) & \chi_2(\mathbf{x}_1) & \cdots & \chi_N(\mathbf{x}_1) \\ \chi_1(\mathbf{x}_2) & \chi_2(\mathbf{x}_2) & \cdots & \chi_N(\mathbf{x}_2) \\ \vdots & \vdots & \ddots & \vdots \\ \chi_1(\mathbf{x}_N) & \chi_2(\mathbf{x}_N) & \cdots & \chi_N(\mathbf{x}_N) \end{vmatrix} = |\Psi\rangle \tag{2.4}$$

$|\Psi\rangle$ denotes a wave function in bra-ket notation.

In order to solve for the many-body wave function, we introduce the concept of a trail wave function which depends on a set of parameters, $\tilde{\Phi}(c_k)$. According to the variational principle, for some given parameter c_k, the energy of the trail wave function is minimized

$$\frac{\partial}{\partial c_k}\langle\tilde{\Phi}|\hat{H}|\tilde{\Phi}\rangle = \frac{\partial}{\partial c_k}\tilde{E} = 0 \tag{2.5}$$

The energy of the trail wave function is an upper limit to the exact energy, $\tilde{E} \geq E_{\text{exact}}$. As we will see, the calculation of the Hartree-Fock energy will eventually become a

numerical minimization problem with the chosen set of parameters c_k.

In analogy to eq. (2.2), a time-independent eigenvalue equation may be constructed using the orbital as eigenfunction.[50,51]

$$\hat{f}(\mathbf{x}_i)\chi_a(\mathbf{x}_i) = \left[-\frac{1}{2}\nabla_i^2 - \sum_{A=1}^{M}\frac{Z_A}{r_{iA}} + \hat{v}^{\mathrm{HF}}(\mathbf{x}_i)\right]\chi_a(\mathbf{x}_i) = \varepsilon_a\chi_a(\mathbf{x}_i) \tag{2.6}$$

$\hat{f}(\mathbf{x}_i)$ is the Fock operator which operates on electron i. The first and second terms in the brackets depend only on electron i and correspond to the kinetic energy of the electron and the attractive Coulomb interactions with all M nuclei with charge Z_A, r_{iA} being the distance to a nucleus. The final term is the Hartree-Fock potential and contains the average of interaction with all other electrons. It takes the form

$$\hat{v}^{\mathrm{HF}}(\mathbf{x}_i)\chi_a(\mathbf{x}_i) = \left(\sum_{b}^{N}\hat{J}_b(\mathbf{x}_i) - \hat{K}_b(\mathbf{x}_i)\right)\chi_a(\mathbf{x}_i) \tag{2.7}$$

where $\hat{J}_b$ and $\hat{K}_b$ are the Coulomb and exchange operators, respectively

$$\hat{J}_b(\mathbf{x}_i)\chi_a(\mathbf{x}_i) = \int \chi_b^*(\mathbf{x}_j)\frac{1}{r_{ij}}\chi_b(\mathbf{x}_j)d\mathbf{x}_j\chi_a(\mathbf{x}_i) \tag{2.8}$$

$$\hat{K}_b(\mathbf{x}_i)\chi_a(\mathbf{x}_i) = \int \chi_b^*(\mathbf{x}_j)\frac{1}{r_{ij}}\chi_a(\mathbf{x}_j)d\mathbf{x}_j\chi_b(\mathbf{x}_i) \tag{2.9}$$

The Coulomb operator $\hat{J}_b(\mathbf{x}_i)$ operates on electron i, which occupies χ_a, and its eigenvalue corresponds to the Coulomb repulsion with electron j, which occupies χ_b. The exchange operator is due to the anti-symmetric many-body wave function (eq. (2.4)). It may be understood as a contribution arising from the exchange of the indistinguishable electrons i and j. Note that the sum in eq. (2.7) also may run over a ($b = a$). In that case, $\hat{J}_a(\mathbf{x}_i)\chi_a(\mathbf{x}_i) = \hat{K}_a(\mathbf{x}_i)\chi_a(\mathbf{x}_i)$; Coulomb and exchange interactions cancel each other out. This cancellation of self-interaction is an advantage of Hartree-Fock theory. In contrast, self-interaction is prominent in density functional theory methods, which gives rise to problems discussed in Section 2.1.2.

The total Hartree-Fock energy is calculated according to

$$E_{\mathrm{HF}} = \sum_{a}^{N}\left(\varepsilon_a - \frac{1}{2}\langle\chi_a^*|\hat{v}^{\mathrm{HF}}|\chi_a\rangle\right) \tag{2.10}$$

where the second term is necessary to avoid double counting of the electron-electron interaction. The spin orbital consists of two parts

$$\chi_i(\mathbf{x}) = \psi_i(\mathbf{r})\alpha(\omega) \quad (2.11)$$
$$\chi_i(\mathbf{x}) = \psi_i(\mathbf{r})\beta(\omega) \quad (2.12)$$

where ψ_i denotes a spatial orbital and $\alpha(\omega)$ and $\beta(\omega)$ are spin functions. The spatial orbitals are expanded in a set of basis functions in order to practically solve the Schrödinger equation. In the Roothaan-Hall approach, the expansion is a linear combination of K atom-centered hydrogen-like atomic orbital (AO) functions.[52,53]

$$\psi_i = \sum_{\mu}^{K} C_{\mu i}\phi_\mu(\mathbf{r}) \quad (2.13)$$

where $\phi_\mu(\mathbf{r})$ is an AO basis function. $C_{\mu i}$ is the coefficient of an AO contributing to the spatial orbital of index i. In numerical calculations, the coefficients are effectively the parameters that are varied during an optimization procedure.

Alternatively, the expansion could be done in a plane wave basis set, which is more common in calculations with periodic boundary conditions due to efficient implementation and excellent transferability of PW basis sets. See Section 2.2.2 for a more detailed discussion on basis sets in the framework of periodic calculations.

Upon substitution of the spin orbitals in eq. (2.6), the Roothaan-Hall equations are acquired which naturally take the form of a matrix eigenvalue equation

$$\mathbf{FC} = \varepsilon\mathbf{SC} \quad (2.14)$$

where $\mathbf{C}$ are the AO coefficients in the $K \times K$ matrix form. $\mathbf{F}$ denotes the Fock matrix

$$\mathbf{F} = F_{\mu\nu} = \int \phi_\mu^*(\mathbf{r_1})\hat{f}(\mathbf{r_1})\phi_\nu(\mathbf{r_1})d\mathbf{r_1} \quad (2.15)$$

and $\mathbf{S}$ the overlap matrix

$$\mathbf{S} = S_{\mu\nu} = \int \phi_\mu^*(\mathbf{r_1})\phi_\nu(\mathbf{r_1})d\mathbf{r_1} \quad (2.16)$$

ε is a diagonal matrix containing the orbital eigenvalues.

Eq. (2.14) is non-linear ($\mathbf{F}$ depends on $\mathbf{C}$) and must therefore be solved iteratively. Initial coefficients $\mathbf{C}_0$ are provided through a starting guess, and upon solving eq. (2.14), an updated coefficient matrix $\mathbf{C}_1$ is acquired. $\mathbf{C}_1$ is fed into the equation again and when the total energy between coefficient matrices $\mathbf{C}_n$ and $\mathbf{C}_{n-1}$ is smaller than a chosen threshold, the energy and wave function are considered to be converged. This iterative method is referred to as the self-consistent field (SCF) method. Because of its foundation in the wave function, the Hartree-Fock method is labeled a wave function

method. From the wave function, a multitude of properties may be extracted: most importantly the electronic energy, but also *e.g.* dipole moments, ionization potentials or dielectric constants and polarizabilities from linear response methods.[54]

An advantage of Hartree-Fock theory is its *ab initio* formulation and the direct connection to the Schrödinger equation. Furthermore, the non-classical exchange interaction is described exactly. However, the theory employs one approximation that is proven critical for most practical uses in chemistry. The interaction of one electron with the remaining $N-1$ electrons is calculated as a mean field interaction of the $N-1$ occupied orbitals, according to eq. (2.7). This problem arises from the assumption that the electrons occupy the N spin orbitals of a single Slater determinant. As a result, the correlated motion of electrons due to Coulomb repulsion is lost.

Since the Hartree-Fock wave function does not consider correlated electrons, the Hartree-Fock energy will always be higher than the exact energy, in accordance with the variational principle, even if an infinitely large basis set were to be used. By convention, a correlation energy

$$E_{\text{corr}} = E_{\text{exact}} - E_{\text{HF}} \tag{2.17}$$

is defined as the systematic error in the Hartree-Fock energy.[55] Chemical problems often require a high degree of accuracy, which typically means that the neglection of electron correlation introduces an error too large for quantitative (and sometimes even qualitative) results.[56] Several methods exist to either approximately or exactly calculate E_{corr}. As such methods are extensions to Hartree-Fock theory, they are also wave function methods and jointly referred to as post-Hartree-Fock methods. Examples are Möller-Plesset perturbation theory,[57] coupled-cluster theory[58] or the configuration interaction method.[59] Here the most relevant advantage of wave function methods is found: Since the accuracy is systematically improvable through 1) larger basis sets and 2) more exhaustive methods of calculating E_{corr}, the exact energy is possible to acquire, although at high (and as for now, often unrealistic) computational cost. Unfortunately, the availability of post-Hartree-Fock methods for calculations employing periodic boundary conditions is scarce due to their difficult implementation.[60,61]

2.1.2 Density functional theory

Due to the serious shortcoming of Hartree-Fock theory to describe electron correlation and the expensiveness of post-Hartree-Fock methods, density functional theory (DFT) is widely applied as a cost-effective quantum chemical method. Here, the working quantity is the electron density $\rho(\mathbf{x})$ ($\rho(\mathbf{r})$ for the closed shell systems) rather than the wave function. As explained below, electron correlation is accounted for in an approximate fashion.

The study of quantum phenomena with the electron density as starting point was first introduced in the Thomas-Fermi model during the formative years of quantum mechanics.[62,63] It was not, however, until the publication of two theorems by Hohenberg and Kohn that a foundation for DFT was laid.[64] First, they proved that the ground state energy of a system is a unique functional of the ground state electron density ρ_0

$$E_0[\rho_0] = T_\mathrm{e}[\rho_0] + V_\mathrm{ee}[\rho_0] + V_\mathrm{ext}[\rho_0] \tag{2.18}$$

The constituents of the energy are themselves functionals of ρ_0. The electronic kinetic energy and Coulomb repulsion functionals are universal whereas the external potential V_ext accounts for all system-specific interactions. The nuclear Coulomb repulsion is treated according to the Born-Oppenheimer approximation and is hence not a functional of ρ_0 when solving eq. (2.18). V_ext is general but typically contains the Coulomb attraction of the electron density with nuclei. Second, Hohenberg and Kohn showed that any energy calculated from a trail electron density ρ_tr is an upper bound to the exact energy of a system

$$E[\rho_\mathrm{tr}] \geq E_\mathrm{exact} \tag{2.19}$$

which is in accordance with the variational principle.

The universal parts of the energy functional (eq. (2.18)) make out the Hohenberg-Kohn functional, $F_\mathrm{HK}[\rho]$ $(= T_\mathrm{e}[\rho] + V_\mathrm{ee}[\rho])$. Unfortunately, the true form of F_HK is unknown. However, parts of it may be obtained through the formalism introduced by Kohn and Sham.[65] They introduced a non-interacting system of fermions described exactly, using one single Slater determinant of so called Kohn-Sham (KS) orbitals.

The kinetic energy of the non-interacting system is simply the sum of the non-interacting orbitals

$$T_\mathrm{n\text{-}i}[\rho] = -\frac{1}{2}\sum_a^N \langle \varphi_a^* | \nabla^2 | \varphi_a \rangle \tag{2.20}$$

where φ denotes a KS orbital. The correction of the kinetic energy, $T_\mathrm{c}[\rho]$, is added to acquire the exact kinetic energy of the interacting system.

$$T_\mathrm{e}[\rho] = T_\mathrm{n\text{-}i}[\rho] + T_\mathrm{c}[\rho] \tag{2.21}$$

The exact calculation of the non-interacting kinetic energy from the electron density expanded in the KS orbitals is trivial. Therefore, a large part of the total kinetic energy is calculated exactly in the KS formalism.[28]

For the electron-electron potential energy, a part is expressed for the classical mean-field Coulomb repulsion of the electron density integrated over space

$$J[\rho] = \frac{1}{2}\iint \frac{\rho(\mathbf{r}_1)\rho(\mathbf{r}_2)}{r_{12}} d\mathbf{r}_1 d\mathbf{r}_2 \tag{2.22}$$

and is typically referred to as the Hartree energy. $J[\rho]$ is calculated exactly from the electron density and the quantum mechanical contributions, $V_{\mathrm{qm}}[\rho]$ are bundled into a correction term to the exact potential energy

$$V_{\mathrm{ee}}[\rho] = J[\rho] + V_{\mathrm{qm}}[\rho] \tag{2.23}$$

It is important to point out that since $J[\rho]$ is a functional of $\rho(\mathbf{r})$, the *total* electron density in the three dimensions, the Hartree energy contains an unphysical self-interaction of an electron with itself, which also needs to be corrected for and which is discussed later in this section.

The expression of the total electronic energy in eq. (2.18) may be modified with the above definitions to give

$$E[\rho] = T_{\text{n-i}}[\rho] + J[\rho] + E_{\mathrm{XC}}[\rho] + V_{\mathrm{ext}}[\rho] \tag{2.24}$$

where the only unknown functional is the exchange-correlation (XC) functional $E_{\mathrm{XC}}[\rho]$, which contains the corrections to the kinetic energy for the correlated system and the quantum-mechanical effects of electron correlation and exchange interaction.

$$E_{\mathrm{XC}}[\rho] = (T_{\mathrm{e}}[\rho] - T_{\text{n-i}}[\rho]) + (V_{\mathrm{ee}}[\rho] - J[\rho]) = T_{\mathrm{c}}[\rho] + V_{\mathrm{qm}}[\rho] \tag{2.25}$$

At this point, a large fraction of the total energy may be calculated exactly. Approximations are needed only for the XC functional which I will discuss in the following section. Eq. (2.24) is solved iteratively though the SCF method until the DFT energy is converged to within a predefined threshold.

In the following section, I discuss the form of the XC functionals commonly used in quantum chemistry. Before this, it is useful to bring up a different viewpoint that is closely related to the correlated motion of electrons. In the restricted formulation of DFT, the pair density $\rho_2(\mathbf{r}_1, \mathbf{r}_2)$ is the probability density of finding an electron 2 at position $\mathbf{r}_2$ given that the position of an electron 1 is $\mathbf{r}_1$. A description on the treatment of spin-polarized systems will be included shortly. In any many-electron system, repulsion due to Coulomb interactions (all electrons) and Pauli repulsion (only electrons of the same spin) lead to a hole around electron 1, where electron 2 is less likely to reside. The hole is referred to as the exchange-correlation hole and is defined as

$$h_{\mathrm{XC}}(\mathbf{r}_1, \mathbf{r}_2) = \frac{\rho_2(\mathbf{r}_1, \mathbf{r}_2)}{\rho(\mathbf{r}_1)} - \rho(\mathbf{r}_2) = h_{\mathrm{X}}(\mathbf{r}_1, \mathbf{r}_2) + h_{\mathrm{C}}(\mathbf{r}_1, \mathbf{r}_2) \tag{2.26}$$

where $\rho(\mathbf{r}_1)$ and $\rho(\mathbf{r}_2)$ are one electron densities. The exchange and correlation parts are further divided into $h_{\mathrm{X}}(\mathbf{r}_1, \mathbf{r}_2)$ and $h_{\mathrm{C}}(\mathbf{r}_1, \mathbf{r}_2)$. In principle, if $E_{\mathrm{XC}}[\rho]$ were known, it would give the correct correlated electron motion and hence the correct shape of the XC hole.

Importantly, $h_{\mathrm{X}}(\mathbf{r}_1, \mathbf{r}_2)$ contains the interaction of an electron with itself (which is an identical particle with the same spin). It can be shown that its integral must fulfill the condition

$$\int h_{\mathrm{X}}(\mathbf{r}_1, \mathbf{r}_2) d\mathbf{r}_2 + \int h_{\mathrm{C}}(\mathbf{r}_1, \mathbf{r}_2) d\mathbf{r}_2 = -1 + 0 \tag{2.27}$$

which corresponds to the removal of one electron, in order to cancel its interaction with itself.[28] In analogy to Hartree-Fock theory (eq. (2.7)), where the Coulomb and exchange operators cancel out the self-interaction, in DFT, the self-interaction contained in the Hartree energy must be canceled by the exchange energy in the exact XC functional

$$J[\rho] = -E_{\mathrm{X}}[\rho_\alpha, 0] \tag{2.28}$$

For a closed shell system, only α spin density is considered as exchange occurs only between electrons of the same spin. To treat open-shell systems, an unrestricted formulation of the KS approach is also available, where the total density is split into spin densities, $\rho(\mathbf{r}) = \rho(\mathbf{r})_\alpha + \rho(\mathbf{r})_\beta$, where the density functionals instead depend on $\rho_\alpha(\mathbf{r})$ and $\rho_\beta(\mathbf{r})$ (see *e.g.* eq. (2.31)).

2.1.3 Exchange-correlation functionals

For practical applications of DFT, the choice of the XC functional is an important one. Conventionally, the functional is separated into the correlation and exchange parts which have been developed separately

$$E_{\mathrm{XC}}[\rho] = E_{\mathrm{X}}[\rho] + E_{\mathrm{C}}[\rho] \tag{2.29}$$

An example is an exchange functional by Becke (B88 or simply B)[66] which is often used in junction with the correlation functional by Lee, Yang and Parr (LYP)[67] to give the XC functional BLYP.

The different approximations and parametrizations mean a plurality of functionals have been developed and implemented in quantum chemical software.[54] Different XC functionals have different parametrization schemes which may be divided into two general types:

- Empirical parametrization schemes employing fitting to a set of reference data, experimental or from calculation. These functionals typically perform better for systems similar to the dataset to which they have been fitted, but sometimes show poor transferability to other systems. Examples are the aforementioned BLYP functional and the B3LYP functional.[68]

- Non-empirical parametrization schemes where the fitting is done to fulfill physical criteria such as asymptotic behaviors and scaling requirements.[69] Typically, these functionals are employed for their straightforward, physically motivated construction, more often so in periodic systems. Examples are the PBE[70] and TPSS[71] functionals.

Commonly, approximations to the XC functional start in the uniform electron gas model, *i.e.* electrons moving and feeling the potential of a homogeneous positive background charge. This is of course not true in a molecular system where positive charge is highly localized at the nuclei. Nevertheless, it is approximated that exchange and correlation effects may be described locally with an XC functional derived from the uniform electron gas model. This local treatment of the exchange and correlation effects gives rise to the common name of the approach: the local density approximation (LDA). The functional form is

$$E_{\mathrm{XC}}^{\mathrm{LDA}}[\rho] = \int \rho(\mathbf{r})\varepsilon_{\mathrm{XC}}[\rho(\mathbf{r})]d\mathbf{r} \tag{2.30}$$

where $\varepsilon_{\mathrm{XC}}[\rho(\mathbf{r})]$ is the XC energy per particle for a uniform electron gas. The advantage with the LDA is that the form of $\varepsilon_{\mathrm{XC}}[\rho(\mathbf{r})]$ is known either exactly (exchange) or may be efficiently interpolated (correlation) from exact solutions at the low and high electron density limits, as found *e.g.* in the Vosko-Wilk-Nusair parametrization.[72]

The electron density may be divided into spin densities corresponding to α and β electrons in the local spin density approximation (LSDA)

$$E_{\mathrm{XC}}^{\mathrm{LSDA}}[\rho_\alpha, \rho_\beta] = \int \rho(\mathbf{r})\varepsilon_{\mathrm{XC}}[\rho_\alpha(\mathbf{r}), \rho_\beta(\mathbf{r})]d\mathbf{r} \tag{2.31}$$

Note that $\varepsilon_{\mathrm{XC}}[\rho_\alpha(\mathbf{r}), \rho_\beta(\mathbf{r})]$ refers to the LSDA XC energy per electron. The integrand $\rho(\mathbf{r})$ is the total electron probability distribution (or density) with which $\varepsilon_{\mathrm{XC}}[\rho_\alpha(\mathbf{r}), \rho_\beta(\mathbf{r})]$ is weighted.[28] This unrestricted DFT formulation is commonly used in studies on open-shell systems, and is not limited to the LSDA.

At each point in space, the XC hole is spherical due to the isotropic nature of the model. In contrast, electron densities in real molecular systems are highly anisotropic, and the LDA functional is commonly used for systems with a high degree of homogeneity in the electron density, more specifically delocalized as in metals. LDA energetically favors cases with a homogeneous electron density; typically, the smoother ρ curvature in a chemical bond, is better described compared to the steep ρ curvature at atoms.[28] This leads to a general favoring of bound systems, giving rise to the overestimation of binding energy and vibrational frequencies as well as underestimation of bond lengths.

A second issue with the LDA/LSDA functionals is the high degree of self-interaction. The spherical LDA exchange hole is often a poor approximation to the exact exchange hole and, as a consequence, LDA tends to severely underestimate the exchange interaction energy.[54] Hence, self-interaction is not canceled completely (*i.e.* eq. (2.28) does not hold), giving rise to two important consequences: First, the electron density tends to become more delocalized to minimize self-interaction. Second, the eigenvalues of occupied orbital levels increase. For metals, both points are only of minor importance due to the delocalized electrons and the lack of a band gap (see Section 2.2.1). However, in systems with localized electrons and/or a band gap, the LDA often performs unsatisfactorily.

Nevertheless, the LDA is almost universally used as starting point for more accurate functionals. To discuss the capabilities of further XC functionals, I will use the well-characterized crystalline (rock salt) phase of NiO as an example system, due to its chemical resemblance to nickel fluorides. NiO is an antiferromagnetic insulator with a band gap of 4 eV,[73] and with the d electrons highly localized on the Ni^{2+} centers. The localization may be probed against the experimental Ni^{2+} spin magnetic moment 1.9 μ_B (Bohr magnetons) coming from the two unpaired d electrons.[74] NiO is labeled a strongly correlated material, due to the failure of mean field theory to describe the localized d electrons.

In a study by Rohrbach *et al.* employing the LDA functional, the band gap of NiO was found to be closed, falsely predicting a metallic compound.[75] The failure to localize electrons was also evident, for example in an underestimation of the magnetic moment at only 1.1 μ_B.

A popular extension to the LDA is the generalized gradient approximation (GGA). To account for the non-homogeneous nature of the electron density in molecular systems, GGA XC functionals also depend on the gradient of the electron density

$$E_{XC}^{GGA}[\rho_\alpha, \rho_\beta] = \int f_{XC}[\rho_\alpha, \rho_\beta, \nabla\rho_\alpha, \nabla\rho_\beta] d\mathbf{r} \tag{2.32}$$

here written in the spin-polarized form. Unfortunately, there is no analytic form for f_{XC}. Instead, the literature provides various parametrizations and implementations of the GGA for exchange[66,70,76–78] and correlation[67,70,77,79–82] functionals. Especially the Perdew-Burke-Ernzerhof exchange and correlation functionals used in junction make out the PBE XC functional[70] which is a popular choice for periodic systems such as metals, together with its revised forms for solids: revPBE, RPBE and PBEsol.[80–82]

GGA functionals often give improved results in comparison to the LDA with respect to binding energies and lattice constants.[83] Due to the non-homogeneous XC hole in the GGA, the unphysical bias towards binding found in the LDA is partially remedied. However, the self-interaction problem is still present and a proper description of band gaps is lacking, which is why GGA functionals are most commonly used

for metals or narrow-gap semiconductors. An important field where GGA XC functionals are preferred is the study of metal-molecule interfaces, such as in heterogeneous catalysis.[84,85]

Returning to our example system NiO, in the study by Rohrbach et al., employing the PW91 XC functional, a band gap is opened but remains severely underestimated at 0.5 eV.[75] Although the Ni^{2+} spin magnetic moment is improved to 1.3 μ_B, it is clear that the inclusion of the $\nabla\rho$ dependency is not sufficient to describe highly localized electrons.

A different but popular idea is to use the exact exchange functional, which is calculated analogously to the Hartree-Fock method (eqs. (2.7) and (2.8)). Instead of Hartree-Fock orbitals, the KS orbitals (eq. (2.20)) are used from which the exchange integrals may be calculated exactly. Typically, a fraction of exact exchange is included and mixed with a GGA exchange functional, for example as in the PBE0 functional[86]

$$E_{XC}^{PBE0} = 0.75E_X^{PBE} + 0.25E_X^{exact} + E_C^{PBE} \tag{2.33}$$

which utilizes 25 % exact exchange together with the PBE exchange and correlation functionals. XC functionals with inclusion of exact exchange are referred to as hybrid functionals.

Only a fraction is used, as taking simply the exact exchange functional typically leads to an error: In the KS method, the using the non-interacting system as reference leaves a highly localized XC hole. However, the exact exchange interaction is a fully delocalized property (eq. (2.8)). The assumption that the XC hole may be divided into is exchange and correlation parts leads to a mismatch between a localized correlation hole and a delocalized exchange hole.[28] The fraction in the PBE0 functional has been determined through a perturbative approach and the functional is hence free of empirical parameters. Alternatively, the fraction may be fitted to reference data, as is the case in the B3LYP hybrid functional.[68]

The calculation of exact exchange includes performing an extra step throughout the SCF procedure, in calculating non-local exchange integrals (see eq. (2.8)). The calculation effort scales particularly poorly for calculations employing PW basis sets, where hybrid functionals typically require about one more order of calculation time compared to GGA functionals.[54] However, with higher computational capacities, hybrid functionals are finding an increasingly wide usage in PW basis set calculations, especially for electronic properties of strongly correlated materials, although such hybrid calulations are often resticted to relatively small unit cells.[38–40,87] To reduce calculation efforts with only a small loss of accuracy, range-separated hybrid functionals may be used, for example in the formulation by Heyd, Scuseria and Ernzerhof (HSE), which exploit the short-range nature of exchange interaction due to Coulomb screening[88]

$$E_{\mathrm{XC}}^{\mathrm{HSE0x}} = 0.75E_{\mathrm{X}}^{\mathrm{PBE,SR}}(\omega) + 0.25E_{\mathrm{X}}^{\mathrm{exact,SR}}(\omega) + E_{\mathrm{X}}^{\mathrm{PBE,LR}}(\omega) + E_{\mathrm{C}}^{\mathrm{PBE}} \tag{2.34}$$

where the new parameter ω is the screening parameter. The exchange functional is divided into a short-range (SR) PBE0 part and a long-range (LR) PBE part without exact exchange. For example, $\omega = 0.2$ corresponds to the HSE06 functional, whereas for $\omega = 0$, the functional reduces to PBE0.

2.1.4 Dispersion interaction

I have already discussed the approximate inclusion of electron correlation effects in the XC functional, $E_{\mathrm{XC}}[\rho]$ (eq. (2.24)). An important part of the correlation energy stems from long-range dispersion interaction. In some systems, such as noble gases[89,90] or molecules without permanent (*i.e.* static) dipole moments,[91–93] dispersion accounts for the largest part of the binding energy. Also in many other systems, which involve *e.g.* inter-molecular interactions or molecule-surface interfaces,[94–96] dispersion contributes to the binding significantly, and may not be neglected. For adsorption processes of HF on Ni surfaces, physisorption of molecules could give rise to non-covalently bound reaction intermediates, which may effectively raise the activation barrier.[97]

Dispersion interaction arises due to electrostatic interactions between instantaneous, induced multipoles. In principle, the induced multipoles may be of any order, but the largest contribution is generally due to London dispersion, which includes the attractive interaction between two induced dipoles at two bodies.[98] For two atoms i and j, the London dispersion potential has the approximate analytic form[99]

$$V_{\mathrm{disp}} = -\frac{3}{2}\frac{I_i I_j}{I_i + I_j}\frac{\alpha_i \alpha_j}{r_{ij}^6} \tag{2.35}$$

where I_i and I_j are the ionization potentials of the atoms, α_i and α_j are the polarizabilities and r is the distance between the atoms.

Calculations considering London dispersion interaction (or any other type of dispersion) present a problem for standard DFT functionals. As briefly mentioned above, the induced dipole interactions are by nature a phenomenon of the correlated motion of electrons. Furthermore, dispersion effects are most important for long-range (approx. $r > 3$ Å) interactions. LDA and GGA functionals are constructed from the approximation that electron correlation may be treated as a local phenomenon (eqs. (2.30) and (2.32)). Although GGA functionals also include the gradient of the electron density, this is insufficient for the long-range interaction.[28] Also hybrid functionals are incapable of the task. Although the inclusion of exact exchange is indeed

non-local, dispersion interaction is a phenomenon due to (Coulomb) correlation which is still treated locally. Due to the shortcomings of the common approximations to the XC functional, methods for including dispersion interaction have been developed, of which I will describe two conceptually different methods that are applied in many of the calculations in this thesis.

The first method, commonly referred to as DFT-D involves a dispersion correction term to the DFT energy, as proposed by Grimme[100–102]

$$E_{\mathrm{DFT-D}} = E_{\mathrm{DFT}} + E_{\mathrm{D}} \tag{2.36}$$

where E_{DFT} is calculated self-consistently and the correction term E_{D} is added *a posteriori*. E_{D} involves a sum of all pair-wise atom-centered London dispersion interactions, where the only input variables are the nuclear coordinates of the system. A popular application is the D3(BJ) dispersion correction,[102] which builds upon the earlier D2 and D3 schemes.[100,101] In it, the dispersion correction term has the form

$$E_{\mathrm{D3(BJ)}} = -\frac{1}{2}\sum_{i\neq j}\sum_{n=6,8} s_n \frac{C_n^{ij}}{r_{ij}^n + \left[f_{\mathrm{D3(BJ)}}^{\mathrm{damp}}(r_{\mathrm{D3(BJ)}}^{ij})\right]^n} \tag{2.37}$$

where C_n^{ij} is the specific n-order pair coefficient for the interaction between atoms i and j at distance r_{ij}. Unlike the simpler D2 scheme, which only includes sixth-order interaction, the D3 and D3(BJ) schemes consider also an eight-order attractive term, since this was found to improve the description of mid-range dispersion.[102] In general, a challenge in developing such correction schemes is to avoid over-binding due to a too attractive E_{D} at short and mid-range distances, since the E_{DFT} term is expected to account for electron correlation at these distances. Therefore, the factor s_n is included which is scaling factor specific for each XC functional. Furthermore, the damping function developed by Becke and Johnson (BJ) serves the purpose to improve the short-range description and prevent the asymptotic limit of an infinite negative energy for $r \to 0$.[103] The BJ damping function is the main difference between D3(BJ) and D3, which employs a different function.[101] The BJ damping function has the form

$$f_{\mathrm{D3(BJ)}}^{\mathrm{damp}}(r_{\mathrm{BJ}}^{ij}) = a_1 r_{\mathrm{BJ}}^{ij} + a_2 \tag{2.38}$$

where a_1 and a_2 are parameters fitted for each functional. r_{BJ}^{ij} is the ij atom pair specific cutoff radius which is calculated from the pair coefficients

$$r_{\mathrm{BJ}}^{ij} = \sqrt{\frac{C_8^{ij}}{C_6^{ij}}} \tag{2.39}$$

In the D2 correction, they are calculated in a simple way from atomic polarizabilities and ionization potentials from time-dependent DFT calculations with the PBE0

functional.[100] The D3 and D3(BJ) schemes aim to take into consideration differences in polarizabilities for atoms in different chemical environments. Therefore, the coefficients are calculated from differences in polarizabilities of atoms with various numbers of ligands. Hence, in the D3 and D3(BJ) schemes, the C_n^{ij} coefficients depend on the coordination numbers of atoms i and j. C_n^{ij} coefficients were provided by Grimme *et al.* for all elements until Pu, and were calculated using time-dependent DFT and the PBE0 functional.[101] By including atom pairs in neighboring periodic cell images, the DFT-D method may be applied also for periodic systems.[104] In practical calculations, implementations of these dispersion correction schemes perform a connectivity analysis using the nuclear coordinates and select the proper coefficients. In periodic plane-wave calculations of surfaces with slab models (see Section 2.5), a distance cut-off must be set for the coefficients, so that unwanted dispersive interactions between vacuum-separated slabs is avoided.

The DFT-D3 and DFT-D3(BJ) schemes are growing increasingly popular, much due to their cost-efficiency and robustness of the provided C_n^{ij} coefficients.[105,106] The calculation time of all pair-wise interactions is essentially negligible compared to the SCF calculation. The main weakness of the DFT-D methods is the semi-empirical formulation itself. This means the method should, if possible, be bench-marked against a higher level treatment (*e.g.* coupled-cluster theory), especially for weakly bound systems. Furthermore, the separation of dispersion interaction from the *ab initio* calculation means that influences on the dispersion interaction by *e.g.* an external electric field are neglected.[107] On the other hand, this separation provides for free a rough method for energy decomposition analysis, and we are able to estimate the contribution of dispersion interaction to the total binding energy of two species. Additionally, the C_n^{ij} coefficients may perform worse for systems far from equilibrium, such as crystals under high pressure,[108] since the coefficients are optimized for atoms with equilibrium bond lengths.

The second method for the inclusion of dispersion effects in DFT considers the instantaneous dipoles as plasma oscillations. The class of van der Waals (vdW) density functionals are based on the ansatz

$$E_{\mathrm{XC}}^{\mathrm{vdW}}[\rho] = E_{\mathrm{XC}}^{0}[\rho] + E_{\mathrm{C}}^{\mathrm{nl}}[\rho] \tag{2.40}$$

where the first term $E_{\mathrm{XC}}^{0}[\rho]$ is a local XC functional (typically with the GGA) and $E_{\mathrm{C}}^{\mathrm{nl}}[\rho]$ is a correction term for non-local correlation. Here, in contrast to Grimme's method, the correction term is a proper functional of the electron density. The non-local correlation term has the general form

$$E_{\mathrm{C}}^{\mathrm{nl}}[\rho] = \frac{1}{2}\int \mathrm{d}^3r\mathrm{d}^3r'\rho(\mathbf{r})\phi(\mathbf{r},\mathbf{r}')\rho(\mathbf{r}') \tag{2.41}$$

where ρ is the electron density and $\mathbf{r}$ and $\mathbf{r}'$ refer to two points in space. $\phi(\mathbf{r},\mathbf{r}')\rho(\mathbf{r}')$

is a kernel depending on the two coordinates as well as the electron density.[109] The purpose of $\phi(\mathbf{r},\mathbf{r}')\rho(\mathbf{r}')$ is to quantify the interaction strength between plasma oscillations separated by the distance $\mathbf{r}-\mathbf{r}'$. Practical expressions for this function contain approximations, which vary between different vdW functionals, and the expressions are typically complicated.

The vdW-DF functional, developed by Lundqvist and coworkers, employs the revPBE GGA functional as $E_{\mathrm{XC}}^{0}[\rho]$.[110] The dispersion part is centered around the so-called plasmon-response description[111]

$$S_{\mathrm{XC}}(\mathbf{r},\mathbf{r}';iu) = \langle \mathbf{r}| \ln \epsilon(iu)|\mathbf{r}'\rangle \tag{2.42}$$

where ϵ is the dielectric tensor as a function of imaginary frequency iu. From a Taylor expansion of $e^{S_{\mathrm{XC}}}$ until second order, the non-local part is approximated as

$$E_{\mathrm{C}}^{\mathrm{nl}}[\rho] = \int \frac{\mathrm{d}u}{4\pi} \mathrm{Tr}\Big\{ S_{\mathrm{XC}}^{2} - \left(\frac{\nabla S_{\mathrm{XC}} \nabla V}{4\pi} \right)^{2} \Big\} \tag{2.43}$$

where V comes from the Coulomb coupling term in the well-known adiabatic ansatz with the coupling parameter λ

$$H_{\lambda} = T + V_{\mathrm{ext},\lambda} + \lambda V \tag{2.44}$$

In the vdW-DF functional, a model for S_{XC}^{2} is constructed under a number of constraints, most importantly with regards to asymptotic behaviors of certain variables. The specific constraints and shape of the function is given in a contribution by Schröder *et al.*[109] A fitting to empirical data was avoided, although the asymptotic limits were considered for dimers of noble gases.[110] The vdW-DF functional gave reasonable C_{6}^{ij} coefficients from calculated potential energy curves of the noble gas dimers.

vdW functionals could generally be considered to be more "in the spirit" of the first principles approach, since they are explicit functionals of the electron density, with well understood approximations to the functional, much like the standard LDA or GGA functionals themselves. The vdW-DF implementation has been shown to come at little extra calculation cost.[112] An advantage over the DFT-D dispersion correction is that vdW functionals qualitatively correctly describe the asymptotic limit of the dispersion energy as $r_{ij} \to 0$, where r_{ij} is the distance between two atoms.[113] Therefore, one might expect vdW functionals to give a more consistent description of dispersion effects for atoms not at equilibrium bond lengths (*e.g* atoms in vibrational motion) compared to the DFT-D methods which rely on damping functions.

Unfortunately, a rather significant dependence on the local GGA functional (eq. (2.40)) has been noted by Reimer *et al.*, for various vdW functionals applied on

interfaces involving metallic surfaces.[113] Also DFT-D methods were described as overestimating the binding of molecules to metallic surfaces. If a more robust, explicitly quantum mechanical treatment of dispersion interaction is to be done, one would require wave function methods such as Möller-Plesset perturbation theory,[57] or coupled-cluster theory.[58] However, implementations of such methods for periodic systems are still rare,[60,61] even more so for metallic systems. An alternative solution readily available for periodic systems are perturbative methods, such as the random phase approximation,[114] although this method suffers from unfavorable scaling with system size.[113]

Dispersion interactions in DFT remains an active field in research, and often are the approximate methods (*e.g.* DFT-D and vdW functionals) tested against a benchmark calculation or evaluated with respect to some physical property, such as a binding energy. In DFT calculations involving non-covalent interactions, for example the HF/Ni interfaces considered in this work, including some form of dispersion correction is absolutely necessary. One reason for this is that simply a GGA functional would not be able to correctly describe even the simplest adsorption reaction of a single HF molecule on a surface, since the physisorption binding would be predicted by GGA functionals as either too weakly bound or even unbound.

2.2 Periodic systems

The foundation of our understanding of crystalline systems dates back to the discovery of X-ray diffraction by von Laue in 1912.[115] Crystals are defined as condensed matter with a periodic arrangement of atoms. Although real crystals are terminated at their edges (finite) and have various defects, when studying a crystalline system, it is usually assumed that it can be approximated as infinite, perfect crystals. Formally this is expressed as the crystal being identical viewed from two points $\mathbf{r}'$ and $\mathbf{r}$ which are related by

$$\mathbf{r}' = \mathbf{r} + u_1\mathbf{a}_1 + u_2\mathbf{a}_2 + u_3\mathbf{a}_3 = \mathbf{r} + \mathbf{T} \tag{2.45}$$

where $\mathbf{a}_1$, $\mathbf{a}_2$ and $\mathbf{a}_3$ are vectors describing the periodically repeating unit cell and u_1, u_2 and u_3 are integers. These quantities are bundled together in the real space translation vector $\mathbf{T}$. Hence, the vectors make up a lattice as shown in the left part of Fig. 2.1 as a two-dimensional case with $\mathbf{a}_1$ and $\mathbf{a}_2$. In two dimensions, there are five possible combinations of $\mathbf{a}_1$ and $\mathbf{a}_2$ with respect to their absolute values being identical or not, and their angle being 90°, 60° or none of the two.[116] In three dimensions including also $\mathbf{a}_3$, there are 14 combinations which are referred to as the Bravais lattices.

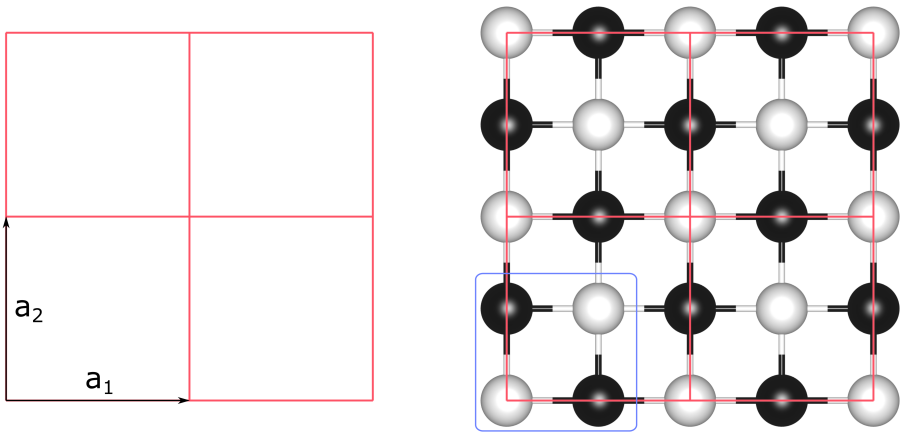

Figure 2.1: Two-dimensional view of a diatomic crystal in the cubic NaCl structure. Left: The empty lattice (red) as constructed from lattice vectors $\mathbf{a}_1$ and $\mathbf{a}_2$. Four unit cells are depicted. Right: The basis (blue square) is added to the unit cell which fills up the lattice with atoms.

If all points $\mathbf{r}$ in a unit cell are described with respect to some property, all points in its infinite Bravais lattice are equally well described. Let that property be the atomic coordinates in the crystal and we quickly realize that only the coordinates

within the unit cell are needed to describe the structure of the entire crystal. This translational symmetry constraint greatly reduces the number of atoms in a crystal from a number in the order of 10^{23} to the number of atoms within the unit cell. The atoms in the unit cell are referred to as the basis (not to be confused with basis sets). In the right hand side of Fig. 2.1, the basis (marked in blue) has been added to the lattice and a crystal has taken shape.

The periodic symmetry introduced in eq. (2.45) has the consequence that any local property of the (idealized) crystal follows the same symmetry. Such a property is *e.g.* the electron density $\rho(\mathbf{r})$. Because of the periodic symmetry, real space-depending functions such as orbitals or $\rho(\mathbf{r})$ may be subject to Fourier analysis. The transformation from real space coordinates to reciprocal coordinates has been proven very useful to describe properties of crystals. The Fourier expansion takes the shape

$$\rho(\mathbf{r}) = \sum_{\mathbf{G}} \rho_{\mathbf{G}} e^{i\mathbf{G}\cdot\mathbf{r}} \tag{2.46}$$

where $\mathbf{G}$ is a set of vectors such that the equation is invariant under all real space translation vectors $\mathbf{T}$. It can be shown that $\mathbf{G}$ is the reciprocal space analog of $\mathbf{T}$[116]

$$\mathbf{G} = v_1\mathbf{b}_1 + v_2\mathbf{b}_2 + v_3\mathbf{b}_3 \tag{2.47}$$

where v_1, v_2 and v_3 are integers and $\mathbf{b}_1$, $\mathbf{b}_2$ and $\mathbf{b}_3$ are the reciprocal lattice vectors. The length of a reciprocal lattice vector i is related to the inverse length of the corresponding real space lattice vector

$$|\mathbf{b}_i| = \frac{2\pi}{|\mathbf{a}_i|} \tag{2.48}$$

where the factor of 2π comes from the Fourier expansion. As a consequence, a small real space unit cell will have a large reciprocal space unit cell and *vice versa*.

Any real space lattice may be Fourier-transformed into a reciprocal one. In the case of the two-dimensional square lattice in Fig. 2.1, the Fourier transform yields another square lattice. This need not be the case; for instance, the fcc crystal lattice of Ni is transformed into a bcc reciprocal lattice.

$\mathbf{T}$ and $\mathbf{G}$ are related through

$$e^{i\mathbf{G}\cdot\mathbf{T}} = 1 \tag{2.49}$$

and both correspond to invariant translations between lattice points in real and reciprocal space, respectively. Now, let

$$\mathbf{k} = h\mathbf{b}_1 + k\mathbf{b}_2 + l\mathbf{b}_3 \tag{2.50}$$

where h, k and l are real numbers. $\mathbf{k}$ then corresponds to a point in reciprocal space. Because to the periodicity, only a limited reciprocal volume is necessary to describe all possible values of $\mathbf{k}$. This volume is often constructed as a Brillouin zone (BZ). Fig. 2.2 shows the construction of the BZ for the previous two-dimensional square lattice, although the same principles apply in three dimensions. A reference point in the center of the figure is picked, from which vectors are drawn to all neighboring lattice points (black arrows in Fig. 2.2). Each vector is the normal vector of a one-dimensional line which is drawn halfway between the lattice points (dotted lines in Fig. 2.2). The dotted lines intersect and enclose the first BZ, which is the smallest possible unit required to fully describe the reciprocal lattice. In this two-dimensional example, the BZ is a square-shaped reciprocal area; in three-dimensional systems the BZ is a reciprocal volume which may take on 14 different shapes, analogous to the set of possible Bravais lattices.[116]

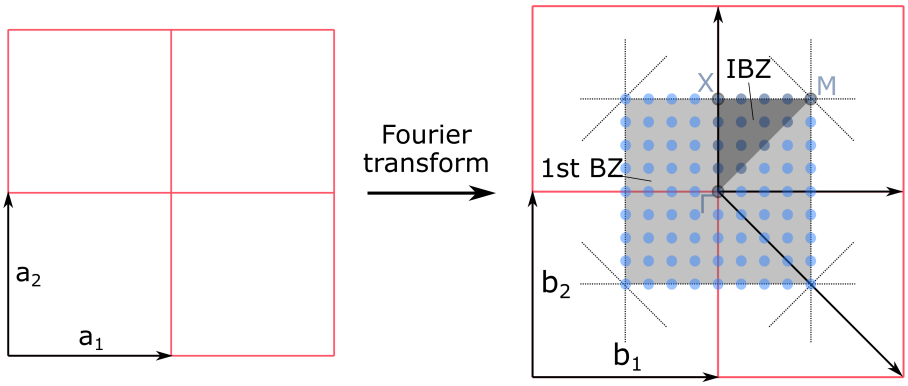

Figure 2.2: The real space two-dimensional square lattice Fourier transformed to the reciprocal space lattice. To the right, a BZ is constructed around the central lattice point. Arrows are drawn from the reference point to all neighboring lattice points. For clarity, only three arrows (one horizontal, one vertical, one diagonal) are shown. Each dotted lines is a normal to an arrow. The first BZ is shown in light gray whereas the IBZ is shown in a darker shade. The blue points correspond to a discrete 8×8 Monkhort-Pack grid of $\mathbf{k}$ points. Due to the crystal symmetry, only the dark blue points within the IBZ must be considered. Also shown are the high-symmetry points Γ, X and M.

Furthermore, depending on the internal symmetry of the Brillouin zones – *e.g.* if atoms of the same element are related by symmetry operations in the crystallographic space groups – an irreducible Brillouin zone (IBZ) may be used in order to reduce the calculation effort further. In Fig. 2.2, the first BZ (lighter gray area) is reduced to an eight of its size (darker gray area) due to the symmetry of the two-dimensional NaCl structure.

Up until now, only strictly geometrical arguments have been used. If a crystal property such as the electron density is to be described, its corresponding wave function needs to fulfill the boundary conditions set by the translational symmetry of the lattice. This is expressed by the Bloch theorem

$$\psi_n(\mathbf{r}+\mathbf{T},\mathbf{k}) = e^{i\mathbf{k}\cdot\mathbf{T}}e^{i\mathbf{k}\cdot\mathbf{r}}u_n(\mathbf{r}+\mathbf{T}) = e^{i\mathbf{k}\cdot\mathbf{T}}\psi_n(\mathbf{r},\mathbf{k}) \tag{2.51}$$

where $\psi_n(\mathbf{r},\mathbf{k})$ is a Bloch function of wave function index n with $u_n(\mathbf{r})$ as the spatial one-electron wave function and the factor $e^{i\mathbf{k}\cdot\mathbf{r}}$.[117] If $u_n(\mathbf{r})$ is constant with respect to $\mathbf{r}$, *e.g.* if there are no nuclei present, the wave function becomes that of a free electron $\psi_n(\mathbf{r},\mathbf{k}) = e^{i\mathbf{k}\cdot\mathbf{r}}$. From free particle theory, we know that $\mathbf{k}$ corresponds to momentum and it is sometimes referred to as crystal momentum in periodic systems, since it is related to the momentum according to de Broglie's formula[118]

$$\mathbf{p} = \frac{h}{\lambda} = \frac{h}{2\pi}\mathbf{k} = \hbar\mathbf{k} \tag{2.52}$$

where $\mathbf{p}$ is the momentum vector of a propagating matter-wave, h ($\hbar$) is the (reduced) Planck constant and λ is the wave length of the propagating wave. More generally, since $\mathbf{r}$ and $\mathbf{k}$ form a Fourier pair, they form complementary variables that obey the uncertainty principle.[119] Bloch wave functions may hence be expressed in terms of $\mathbf{r}$ (real space) or $\mathbf{k}$ (reciprocal or momentum space).

Consider an infinite one-dimensional chain of hydrogen atoms with 1s orbitals as wave functions. $\lambda \to \infty$ corresponds to the sign of the orbitals in all neighboring unit cells being in phase, which leads to no nodes and no crystal momentum. In the case of $\lambda = 2|\mathbf{a}|$, where $\mathbf{a}$ is the lattice vector of the propagation direction, all unit cells are perfectly out of phase with nodes exactly at the cell boundaries.

Both cases correspond to one electronic state each. Crystal momenta between these boundaries are also possible and, in a crystal with the number of electrons in the order of Avogadro's constant, a continuum of states with varying $\mathbf{k}$ and corresponding energies $E(\mathbf{k})$ forms. In band theory, the continuum is referred to as an energy band which is illustrated in Fig. 2.3.

With the dispersion relation in reciprocal space taking the form of a free electron, what is left to address is the deviation from that efficient but unrealistic model. More specifically, $u_n(\mathbf{r})$ must capture the physics of the attractive potential applied by the nuclei as well as electron-electron Coulomb and exchange interactions discussed in Section 2.1.1. Bands in crystals are analogous to orbitals in molecules and with the dispersion relation formulation, an infinite amount of orbitals has been reduced to only the orbitals in the unit cell. $u_n(\mathbf{r})$ is calculated using quantum chemical methods such as Hartree-Fock or DFT, where the latter is by far more popular due to the (approximate) inclusion of electron correlation.

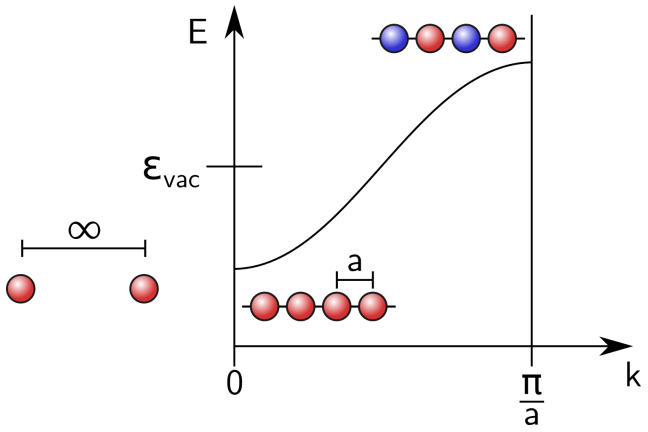

Figure 2.3: Schematic plot of an energy band of a one-dimensional hydrogen chain with the lattice constant a. The 1s orbitals are depicted as spheres and overlap constructively or destructively in the chain. Only the center and border of the BZ are shown. The case for infinitely separated atoms is also included, for which the electronic state is truly discrete and corresponds to one energy level ε_{vac} (arbitrarily set in the graph).

The band eigenvalues depend on $\mathbf{k}$ and this dependence must be numerically considered by discrete sampling of the IBZ. In the example of Hartree-Fock theory, this means

$$\mathbf{F}^{\mathbf{k}}\mathbf{C}^{\mathbf{k}} = \varepsilon^{\mathbf{k}}\mathbf{S}^{\mathbf{k}}\mathbf{C}^{\mathbf{k}} \tag{2.53}$$

where the $\mathbf{k}$-dependence means that one SCF calculation per $\mathbf{k}$ point is necessary to acquire the electronic wave function (Hartree-Fock theory) or electron density (DFT) of an periodic system. For the calculation of properties that do not explicitly depend on the curvature of $E(\mathbf{k})$ along certain directions (*e.g.* structure relaxations, total energy, vibrational frequencies, density of states) a grid of $\mathbf{k}$ points is often used to sample the IBZ (see Fig. 2.2) volume, according to the Monkhorst-Pack scheme.[120] The fineness of the Monkhorst-Pack grid is usually improved until the calculated property of interest convergence with respect to the number of $\mathbf{k}$ points.

If the curvature of $E(\mathbf{k})$ is of importance (*e.g.* band structures, optical properties, anisotropic electric properties) $\mathbf{k}$ points are usually sampled along lines between high symmetry points in the IBZ for band structure plots in two dimensions. In Fig. 2.2, the points are labeled as Γ (by convention at $\mathbf{k} = [0, 0, 0]$), X and M, and a typical trajectory between them is X–Γ–M–X.

2.2.1 Band structures

In this section, I will discuss features of electronic band structures and their usefulness in the analysis of phenomena related to electrons in the valence region such as conduc-

tivity, ionization potentials and electron affinities (redox chemistry) and the study of surface-catalyzed reactions. Some of the systems studied in this thesis provide useful examples for points of discussion regarding the characteristics of various band structures. Especially, the division between metals and insulators is crucial and the two classes typically require different quantum chemical methods for the description of their electronic structure.

Consider an idealized crystal with a number of atoms in the order of Avogadro's constant. The symmetry-consistent reduction of the crystal to its unit cell means the elementary composition of the whole crystal must be retained in the unit cell. Consequently, the number of electrons per cell is exactly the number of electrons of the elements enclosed within the cell. Since electrons are fermions with the intrinsic spin magnetic moment, $s = \frac{1}{2}$, one band may be occupied by zero or two (one α and one β) electrons in a restricted calculation, whereas the unrestricted formulation (see eq. (2.31)) only allows for one electron per band. The bands are populated according to the aufbau principle at any given point k in the BZ, corresponding to a Fermi-Dirac distribution at 0 K.[121] The Fermi energy, E_F, is equivalent to the symmetry point from Fermi-Dirac statistics and corresponds to the highest eigenvalue of the occupied bands at any point $\mathbf{k}$. The highest-energy occupied bands are referred to as valence bands, and contain electron density that is most likely to be donated to a suitable external species, such as an adsorbed molecule. The lowest-energy unoccupied bands are the conduction bands, which correspond to states in the material that are most likely to receive electron density from a suitable molecule.

If the valence electron shells are unfilled, for example in a metal like Ni, looking at one point in k space, there exist low-energy electronic states that are unoccupied at 0 K. This is depicted in Fig. 2.4, left hand side, for Ni. The conduction bands may be partially populated with only little thermal energy, which increases electron mobility, and consequently electric conductivity. Furthermore, since the density of states (DOS) around E_F is continuous in such metallic phases, E_F may be shifted by an external bias, such as a voltage. Two different metals in contact (*e.g.* through a conducting copper wire in an electrochemical cell) with different Fermi energies, will undergo a transfer of electrons from the metal with the higher E_F^hi to the metal with the lower E_F^lo, such that $E_\mathrm{F}^\mathrm{hi} = E_\mathrm{F}^\mathrm{lo}$ after equilibration. E_F is closely related to the chemical potential of electrons in a material, and the usefulness of band structure calculations in understanding electron transfer reactions at electrodes is discussed in more detail in Section 2.6.

The continuity of states around E_F is not present in the other example of NiF_2, in Fig. 2.4, right hand side. In this situation, the valence bands are fully occupied, and separated from the conduction band by a band gap, E_gap. If E_gap is large (> 4 eV), partial occupation of conduction band states is negligible at ambient temperatures, and the material is classified as an electrical insulator. Partial occupation of con-

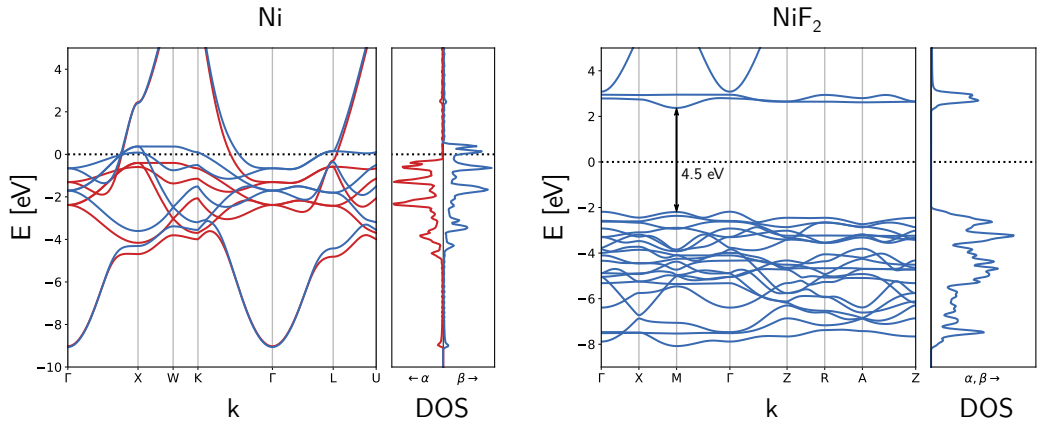

Figure 2.4: Band structures and DOS plots typical of a metal (Ni) and an insulator (NiF_2). Ni is ferromagnetic and with two non-symmetric spin channels labeled red for α bands and blue for β bands. The DOS is plotted with β and α states taking on positive and negative values, respectively. NiF_2 is antiferromagnetic and the spin channels are antisymmetric, why the total DOS here may be fully depicted using only β states ($DOS_\alpha(E) = DOS_\beta(E)$). In Ni, the valence and conduction bands cross at E_F (dashed line), predicting a metal. In NiF_2 valence and conduction bands are separated with a band gap of 4.5 eV at the $k = M$. Ni was calculated with PBE and NiF_2 with PBE+U ($U_{Ni^{2+}} = 5.3$ eV).

duction band states occurs at smaller values of E_{gap} (often around 0.5-2.5 eV), given sufficient thermal energy, and the material may show semiconductor properties. Note that there is currently no consensus of the exact E_{gap} limit that defines a semiconductor or an insulator, and the numbers above should be viewed as commonly found in the literature.

Since both Ni and NiF_2 contain unpaired electrons, DFT in the unrestricted formalism must be used, and two spin channels are depicted as bands with different colors in Fig. 2.4. The ferromagnetic phase of Ni[122] is reproduced as the α bands are occupied to a larger extend. The two unpaired electrons at the Ni^{2+} centers in NiF_2 show a weak antiferromagnetic coupling,[123] which is why the dispersion of the band eigenvalues in (reciprocal) space is equal between the α and β bands, and only one spin channel must be plotted. A more detailed description on the calculation of magnetic properties is given in Section 2.4.

2.2.2 Basis sets and pseudopotentials

To this point, I have separately treated band theory and quantum chemical methods. In Sections 2.1.1 and 2.1.2, the necessity of basis sets was discussed if the Schrödinger equation (for Hartree-Fock) or Kohn-Sham equations (for DFT) are to be practically

solved for any realistic system. Here, I discuss some characteristics of two types of basis sets that may be employed analogously in both Hartree-Fock and DFT. Since this thesis considers almost exclusively periodic systems, basis sets are discussed in the context of periodic calculations, although many points are transferable to non-periodic calculations.

In both Hartree-Fock and DFT, $u_n(\mathbf{r})$ in eq. (2.51) is expanded using a linear combination of basis functions, of which two types are often employed. First, the use of atom-centered Gaussian-type orbitals (GTO) as basis functions is directly equivalent to the LCAO approach and is more common in non-periodic calculations (see eq. (2.13).[124] Typically, core shells are represented by only one GTO per shell as these are unlikely to vary drastically for an element. Naturally, valence electrons are more sensitive towards chemical environments and these typically require more flexibility (variational freedom) through the inclusion of more GTOs. Each valence shell is split into several GTOs, which introduces the principle measurement of quality for an LCAO basis set as the ζ parameter; $\zeta = 2$ means including the double amount of GTOs per valence shell, $\zeta = 3$ includes the triple amount, and so on. Further GTOs are often added, such as polarization and diffuse functions.

Advantages with LCAO basis sets are the efficient treatment of electrons in both valence and core shells since AO-like basis functions provide a good representation of the core orbitals. Furthermore, implementations of (post-)Hartree-Fock or exact exchange as in hybrid DFT functionals are more efficient using the LCAO approach.[125] However, a general problem by using localized basis functions is the basis set superposition error, which causes overbinding due to the more complete basis set in bound systems.[126] In non-periodic calculations, the remedy for this is the use of larger basis sets. Unfortunately, periodic LCAO calculations suffer from numerical instabilities due to linearly dependent basis functions situated at different atoms, since the basis set constitutes a non-orthogonal basis.[127]

These shortcomings of LCAO basis sets are critical for periodic systems. Therefore, $u_n(\mathbf{r})$ is more commonly expanded in a set of delocalized plane waves (PW).

$$u_n(\mathbf{r}) = \sum_{\mathbf{G}}^{K} c_{n\mathbf{G}} e^{i\mathbf{G}\cdot\mathbf{r}} \tag{2.54}$$

where $\mathbf{G}$ is a reciprocal lattice vector and $c_{n\mathbf{G}}$ is the weighting coefficient of a PW with $\mathbf{G}$ in orbital n. The basis set size K is determined by including PWs of increasing energy taken from free particle theory. For an electron using atomic units

$$E_{\text{cut}} = \frac{1}{2}\mathbf{G}_{\text{max}}^2 \tag{2.55}$$

Since the elements of $\mathbf{G}$ are reciprocal lattice vectors scaled by integers, PWs in

a calculation are intrinsically consistent with the symmetry of the lattice. This also means that the basis set quality only depends on the energy cutoff E_{cut}; importantly, there is no BSSE bias towards bound structures. As $\mathbf{G} \to \infty$ the basis set approaches completeness, which means PW basis sets are easily systematically improvable and a large energy cutoff may be considered a complete basis set.[128] Furthermore, PWs always form an orthogonal basis and larger basis sets are not necessarily associated with numerical instabilities. The delocalized nature of PWs means a computationally very affordable basis set size is sufficient to describe delocalized electrons, such as the valence electrons of metals. On the other hand, a large number of plane waves is needed to correctly describe localized electrons such as in ions, lone pairs or in core shells. Especially demanding are core electrons with sharp nodal features, which is why core electrons often are not explicitly considered in a calculation but instead represented by an analytical, pre-optimized pseudopotential.[54] This frozen-core approximation is justified if core electron properties are not of interest, which is true for all calculations in this thesis.

The projector augmented-wave (PAW) method has become one of the most popular types of pseudopotentials.[129–131] First developed by Blöchl, the idea is a partitioning of the all-electron core states $|\psi_{\text{c}}\rangle$ into an explicit wave function outside an augmentation radius r_{aug} from the nucleus and a simplified part inside r_{aug} which is expanded in a radial function and spherical harmonics functions.[132] The partitioning takes the form

$$|\psi_{\text{c}}\rangle = |\tilde{\psi}_{\text{c}}\rangle + |\phi_{\text{c}}\rangle - |\tilde{\phi}_{\text{c}}\rangle \tag{2.56}$$

where the pseudo-wave function $|\tilde{\psi}_{\text{c}}\rangle$ is identical to the all-electron wave function outside r_{aug} but with a smooth (but unphysical) continuation within. The unphysical continuation is corrected for with $|\phi_{\text{c}}\rangle$ and $|\tilde{\phi}_{\text{c}}\rangle$ which are defined within r_{aug} and correspond to the spherical harmonics projection of the all-electron and pseudo-wave functions, respectively. Strictly speaking, this means that the PAW method is rather a method in which the inner parts of the orbitals are smoothed, unlike true pseudopotentials which add potential energy contributions from the core electrons to the Hamiltonian.

2.3 Strongly correlated systems

The shortcomings of LDA and GGA functionals to describe correlated systems, with respect to electron localization and band gaps, were discussed in Section 2.1.3.[133] A useful remedy for both problems are hybrid functionals (see Section 2.1.3 since the portion of exact exchange used reduces electron self-interaction (eq. (2.7)). DFT+U comprises methods that add a parameter U to the DFT energy, and is a more affordable alternative to hybrid functionals often with comparable accuracy.[37] The parameter U has its origin in the Hubbard model Hamiltonian of a periodic lattice of atoms[134]

$$H_{\text{Hub}} = -t \sum_{\langle i,j\rangle,\sigma} \left(c^{\dagger}_{i,\sigma} c_{j,\sigma} + c^{\dagger}_{j,\sigma} c_{i,\sigma} \right) + U \sum_{i} n_{i,\alpha} n_{i,\beta} \tag{2.57}$$

where $\langle i, j\rangle$ refers to a pair of neighboring atomic sites i and j, $c^{\dagger}_{i,\sigma}$ and $c_{i,\sigma}$ are creation and annihilation operators of an electron at site i with spin σ. t is the so-called hopping matrix and may be interpreted as the amplitude of electrons hopping between atomic sites. In other words, t is the contribution to the delocalization of electrons in the solid. If only the first sum of eq. (2.57) is included a Hamiltonian, we arrive at the tight binding approximation.[134] In fact, in this picture, t is directly proportional to the width of a band.[135]

In the Hubbard model, the second sum runs over all electron occupations $n_{i,\alpha}$ and $n_{i,\beta}$ of α and β spin, respectively, and corresponds to Coulomb repulsion between electrons at site i. U enters as the simple parameter for the repulsion between electrons (for which $U > 0$; for other particles this must not necessarily be the case). Larger values of U prohibit hopping of electrons to a given site due to the increase in repulsion from other electrons at that site. In other words, the Hubbard model U term introduces a simple description of electron correlation to the tight binding approximation. Furthermore, a negative term for exchange coupling J may also be included to account for interactions of electrons with parallel spins. Since this term takes a similar form as the U term, it is omitted here for clarity reasons.

The Hubbard model allows for some efficient qualitative analyses of the electronic structure of both metals and insulators. The negative hopping term corresponds to kinetic energy and hence delocalization of electrons. If this term dominates ($t \gg U$), electrons are weakly correlated and will tend to arrange in metallic bands, closer to an electron gas situation. From a chemist's point of view, this is naturally the case for crystals of atoms with partially filled valence shells and hence small on-site repulsion.

On the other hand, if the Coulomb term dominates ($U \gg t$), the strong on-site repulsion prohibits electrons from delocalizing and bands will show less dispersion. This situation corresponds to crystals with *e.g.* localized d or f electrons, or with full atomic valence shells, so that the hopping of an electron to an already filled site is

affiliated with a large repulsive penalty to the energy. Due to this, in contrast to the tight binding approximation, the Hubbard model is capable of qualitatively describing the opening of the band gap due to electron localization in strongly correlated transition metal oxides and fluorides.[136,137]

In KS DFT calculations, most of the kinetic energy is solved exactly (see eq. (2.24)) due to the lower complexity of this one-body contribution (the indices i and j in eq. (2.57) refer to two *atomic* sites, between which *one* electron hops). The energy due to two-body Coulomb repulsion, however, is accounted for by a much larger portion using approximate XC functionals. Consider a thought experiment of calculating a Hubbard-like system with DFT methods. Although local XC functionals (LDA, GGA) contain some description of the correlated Coulomb repulsion, U is generally underestimated, due to reasons already discussed. As the error in the first term of eq. (2.57) is smaller than that of the second term, DFT would generally overestimate the ratio $\frac{t}{U}$ and favor electron delocalization.

The U correction to DFT takes the general form[138]

$$E_{\mathrm{DFT+U}}[\rho_\sigma(\mathbf{r}), \{n_\sigma\}] = E_{\mathrm{DFT}}[\rho_\sigma(\mathbf{r})] + E_U[\{n_\sigma\}] - E_{\mathrm{dc}}[\{n_\sigma\}] \tag{2.58}$$

where the DFT energy E_{DFT} is a functional of the spin densities $\rho_\sigma(\mathbf{r})$. The inclusion of the Hubbard-like term E_U requires a double counting correction E_{dc}, which is an approximate of the on-site repulsions already contained in E_{DFT}. Note that the kinetic part of the Hubbard Hamiltonian is omitted in eq. (2.58) since the kinetic energy is sufficiently well described by DFT.[139]

In plane wave basis sets, the site occupancies $\{n_\sigma\}$ involve the projection of spherical harmonic functions at atomic sites onto the wave function, in order to extract local site occupancies from a wave function expanded in a delocalized basis. The projection scheme and the subsequent evaluation of the double counting energy are performed at each SCF cycle. Typically, this affects calculation effort negligibly and DFT+U calculation costs scale similarly to the underlying XC functional.[140]

The form of the E_U term varies in different implementations, of which the approaches of Liechtenstein *et al.*[139] and Dudarev *et al.*[138] are most popular. In both approaches, in addition to U, the exchange interaction parameter J is considered. The approach of Dudarev considers screened Coulomb interaction with the advantage that the two parameters are related through $U_{\mathrm{eff}} = U - J$ where only the effective Coulomb repulsion parameter U_{eff} is required.

Throughout this work, the Dudarev implementation of DFT+U is used due to its single parameter U_{eff} (simply called U from now on). The expression for the correction takes the form

$$E_U = \frac{U-J}{2} \sum_\sigma \left[\left(\sum_{m_1} n^\sigma_{m_1,m_1} \right) - \left(\sum_{m_1,m_2} n^\sigma_{m_1,m_2} n^\sigma_{m_2,m_1} \right) \right] \tag{2.59}$$

where m_i are spherical harmonic functions and n_{m_i,m_j} are the on-site occupancy matrix. In this formulation, E_U, may be thought of as a penalty function for non-idempotent occupancies.

Although U has a clear physical meaning in the Hubbard model, the simplified picture of discrete sites translates poorly to a quantum chemical one where electron density is inherently smeared out in space. Hence, in DFT+U, there exist no universal values for U, and results may depend drastically on the parameter. U is often chosen empirically by fitting a calculated observable to an experimentally measured one (e.g. the band gap[141] or magnetic phase stability[142]), with the disadvantage that the transferability of the parameter for calculation of other properties may be poor.[143]

Alternatively, U may be calculated without the use of experimental data using linear response theory, in the spirit of Cococcioni *et al.*.[144] In their methodology a small perturbation to the local potential is applied at a site of interest after a DFT calculation. By studying the response of projected site occupation numbers towards the perturbation, U may be calculated.

Due to its smaller calculation effort, the DFT+U method is efficiently employed for structure optimizations that possibly need many SCF calculations and are generally less sensitive to the U parameter.

2.4 Magnetic systems

Most systems considered in this thesis display various forms of magnetism. For example, metallic Ni displays collective magnetism in the form of a ferromagnetic (FM) phase below the critical temperature, T_{cr}, of 631 K (for ferromagnets, the "Curie temperature").[122] Although chemically very different from metals, transition metal fluorides such as MnF_3 or CoF_3 also have macroscopically ordered magnetic phases; both have antiferromagnetic (AFM) phases with $T_{\mathrm{cr}} = 43$ K (for antiferromagnets, the "Néel temperature") for MnF_3 and $T_{\mathrm{cr}} = 460$ K for CoF_3.[145] In this section, I describe the applied approaches to describe magnetic phenomena in crystals.

If we consider an atom with some unpaired electrons, the electrons exhibit a magnetic moment $\mathbf{m}_{\mathrm{s}}$ due to their spin

$$\mathbf{m}_{\mathrm{s}} = -g_{\mathrm{s}}\mu_{\mathrm{B}}\frac{\mathbf{S}}{\hbar} \tag{2.60}$$

where g_{s} is the Lande g factor of an electron, μ_{B} is the Bohr magneton and $\mathbf{S}$ is the total spin quantum number of the unpaired electrons ($\mathbf{S} = \frac{1}{2}, 1, \frac{3}{2}...$ for 1, 2, 3... electrons). μ_{B} is defined as $\frac{e\hbar}{2m_{\mathrm{e}}}$, or exactly $\frac{1}{2}$ atomic unit.[146] g_{s} is dimensionless, and has been measured to a value close to 2.000.[147] Therefore, the magnetic moment per electron is approximately one μ_{B}. Hence, electron magnetic moments are conventionally given in units of the Bohr magneton, and this practice is followed throughout this thesis.

Coupling between the magnetic moments due to electron spins give rise to ordered magnetic phases. The magnetic compounds considered in this work exhibit magnetic coupling by two different mechanisms. First, direct exchange coupling is depicted in Fig. 2.5a, and is characterized by the coupling between localized spin magnetic moments at adjacent magnetic centers. This is the case for metallic Ni. Ni is a typical band magnet, meaning the bands around E_{F} give rise to both conducting and magnetic properties. The occupied bands are largely hybridized, which gives rise to non-integer magnetic moments (in units of μ_{B}) per unit cell.[146] FM phases may be understood in terms of the Stoner criterion, which states that if, for the *para*magnetic phase

$$UD(E_{\mathrm{F}}) > 1 \tag{2.61}$$

holds, the system will spontaneously relax into a FM phase.[148] U is a Coulomb repulsion term related to the Hubbard Hamiltonian U and $D(E_{\mathrm{F}})$ is the DOS at the Fermi energy in the paramagnetic phase. In DFT calculations of weakly correlated systems, U is sufficiently well described (see Section 2.3) already at the GGA level and the magnetic structure of band magnets are typically correctly predicted with

respect to phase stability and $\mathbf{m}_s$. $\mathbf{m}_s$ is calculated by the degree of spin polarization

$$\mathbf{m}_s = n_\alpha - n_\beta \tag{2.62}$$

where n_α and n_β are calculated by integration over occupied states in the unrestricted DFT calculation.

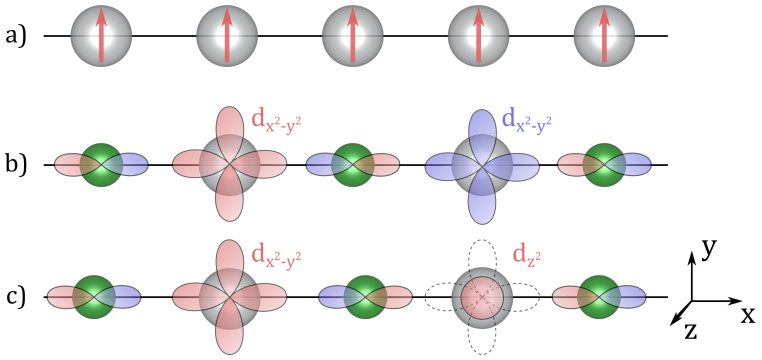

Figure 2.5: Schematic view of coupling mechanisms for unpaired electrons. Gray and green atoms denote metal centers and fluoride ions, respectively. Red and blue colors indicate electron densities α and β electrons. a) Direct exchange coupling. The orbitals are typically hybridized, which is why only the spins are included. b) AFM superexchange coupling between metal centers of configuration $(e_g)^2$ (d_{z^2} not depicted). Note that the magnetic fields of the surrounding metal centers induce magnetic dipole moments at the diamagnetic fluoride ions, which enhances the magnetic coupling strength. c) FM superexchange coupling between metal centers of configuration $(e_g)^1$. Occupations alternate between $(d_{z^2})^1$ and $(d_{x^2-y^2})^1$ along the x axis, resulting in a Jahn-Teller distortion.

The second mechanism under consideration is the superexchange coupling between two metal centers with highly localized magnetic moments separated by diamagnetic ions.[149] Therefore, superexchange coupling is predominantly a phenomenon of ionic crystals, such as transition metal fluorides or oxides. The local crystal-field environment at the metal center causes splitting of the d orbital levels. Generally, higher energy orbitals point directly towards the closed-shell ions. If such an orbital is singly occupied (spin-polarized), its spin magnetic moment induces a magnetic dipole at the anions (see Fig. 2.5). As a consequence, neighboring magnetic centers separated by the anions respond to the induced magnetic dipole.

The superexchange coupling mechanism is depicted in Fig. 2.5b and c. For clarity, the three-dimensional crystal has been reduced to one dimension or repeating metal centers (M) and bridging ions (I). The sign of the superexchange coupling is best understood for octahedral crystal field environments and when the coupling angles $\varphi_c = \angle(\mathrm{M-I-M}) = 180°$, since this aligns the high-energy e_g orbitals directly

towards the ions. In this case, the semi-empirical Goodenough-Kanamori rules are applicable:[150]

- If the metal has half-filled e_g shells, $(e_g)^2$, these orbitals must point directly towards the ions. The metal centers couple strongly antiferromagnetically in order to minimize Pauli repulsion (see Fig. 2.5b).

- If the metal has an unoccupied orbital, $(e_g)^1$, it undergoes weakly FM coupling (see Fig. 2.5c). The occupied e_g orbitals at neighboring metal centers alternate between $d_{x^2-y^2}$ and d_{z^2} to minimize overlap with the anions. This is often accompanied by a Jahn-Teller distortion of the lattice. The magnetic dipole at the anion stabilizes the FM coupling due to exchange interaction (*cf.* Hund's rule).[151]

Note that early transition metal fluorides with only the lower-energy t_{2g} orbitals occupied may also couple in a similar fashion, albeit weakly, as is manifested in the AFM phase of CrF_3 below 80 K.[145]

Jahn-Teller distortions that extend throughout the entire crystal are referred to as cooperative. Cooperative Jahn-Teller distortions may be drastic and largely energetically favorable, as is often the case with FM superexchange-coupling crystals.[152] Such static distortions may be experimentally observable at low enough temperature. Alternatively, Jahn-Teller distortions may be more subtle and only affiliated with a small energy decrease. If the energy decrease is in the order of or lower than the zero-point energies of the lattice phonons, only their superposition (typically the undistorted structure) is observable. Such a case is referred to as dynamical cooperative Jahn-Teller distortion.

Due to its rock-salt structure,[153] NiO is an ideal example of an antiferromagnet with superexchange coupling. Although such a structure is not found in any known magnetic 3d metal fluorides, the rutile-type MF_2 and distorted perovskite-type MF_3 all show octahedral ligand structures, albeit some distorted to various degrees.[154] Furthermore, for the fluorides, $\angle(\mathrm{M}-\mathrm{I}-\mathrm{M})$ deviates from 180° (see φ in Fig. 2.6), with the consequence of higher-order induced magnetic multipoles at the anions. At some small enough φ, the simple Goodenough-Kanamori rules break down.

Through DFT methods, we may model the magnetic polarization regardless of complexity, with the underlying XC functional as the limiting factor for accuracy. Furthermore, the coupling strength and T_{cr} may be calculated using a semi-classical Heisenberg model in the mean field approximation.[155] First, we divide the total energy of a system of some magnetic phase, $E_{\mathrm{tot}}^{\mathrm{phase}}$, into a non-magnetic part with all magnetic degrees of freedom expressed as the collinear Heisenberg model (Ising model). This means we neglect spin-orbit coupling.

$$E_{\text{tot}}^{\text{phase}} = E_{\text{nonmag}} - \frac{1}{2}\sum_{N}\sum_{l}(z_{N,l}^{\uparrow\uparrow} - z_{N,l}^{\uparrow\downarrow})J_{N,l}S_N^2 \tag{2.63}$$

where N refers to a magnetic site and l refers to a coupling type. Depending on the structural and magnetic anisotropy at N, several coupling types may be required. $z_{N,l}^{\uparrow\uparrow}$ and $z_{N,l}^{\uparrow\downarrow}$ are the number of parallel and anti-parallel spin configurations for the coupling l at N, in the magnetic phase under consideration. S_N^2 is the spin magnetic moment at N and may be taken either as the "ideal" half-integer value for the electrons, or calculated from DFT calculations, as the difference in local electron spin density, using *e.g.* the atoms in molecules theory.[156] The latter method is used throughout this work, as it is a better description the spin magnetic moment in real crystals, especially when the metal-ligand bonds display covalent character.[157] J_l is the coupling constant and corresponds to the coupling strength of l. Its sign determines the coupling type; $J_l > 0$ favors the parallel configuration where as $J_l < 0$ favors anti-parallel one.

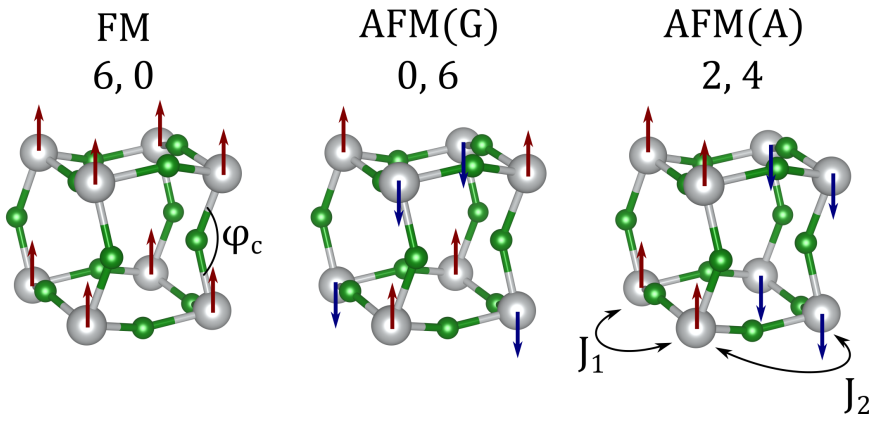

Figure 2.6: Magnetic phases of MF_3, represented as a pseudo-cubic half-unit cell. The number of parallel and anti-parallel couplings ($z_{\uparrow\uparrow}$, $z_{\uparrow\downarrow}$) per metal center is indicated for each phase. Spin up and down are represented as red and blue arrows. First nearest neighbor coupling proceeds with the coupling constants J_1 and J_2. If the metal centers are magnetically isotropic, $J_1 = J_2$.

Adequate magnetic phases are sampled, with the corresponding $E_{\text{tot}}^{\text{phase}}$ calculated using DFT. This gives a system of linear equations to solve, after which E_{nonmag} and the coupling constants are acquired. Three phases of MF_3 (M=Ti,V,...,Ni) are presented in Fig. 2.6. The metal centers are six-fold coordinated and for all M except Mn, the coupling is isotropic, yielding only one coupling constant J_1 for the first coordination sphere. Further distant couplings are disregarded. Hence, the FM and AFM(G) phases are sufficient to solve for J_1. In MnF_3, the coupling is anisotropic

due to reasons discussed above, and the AFM(A) phase is additionally required to solve for J_1 and J_2. The factor of $\frac{1}{2}$ is included to account for double counting.

With the coupling constants in hand, T_{cr} of a phase may be calculated analytically within the mean field approximation[116] (the sum over N is dropped as all metal centers are equivalent in this crystal)

$$T_{\mathrm{cr}} = \frac{S(S+1)}{3k_{\mathrm{B}}} \sum_{l} (z_l^{\uparrow\uparrow} - z_l^{\uparrow\downarrow}) J_l = \frac{2}{3} \frac{(1+\frac{1}{S})}{k_{\mathrm{B}}(E_{\mathrm{nonmag}} - E_{\mathrm{tot}}^{\mathrm{phase}})} \tag{2.64}$$

where k_{B} is Boltzmann's constant and the remaining quantities refer to the energetically most stable phase. Critical temperatures calculated with this approach suffer from the neglection of correlation, systematically leading to an overestimation of T_{cr}, often by a factor around 50 %.[158] At elevated temperatures, spin fluctuations play an important role and are an intrinsically correlated phenomenon.[146] The fluctuations lead to a decrease in net magnetic moment and an observed T_{cr} lower than the prediction by eq. (2.64). Nevertheless, the mean field approach may describe both Curie and Néel temperatures in magnetic ionic crystals qualitatively or semi-qualitatively, on the basis of DFT calculations.[40,157,159]

2.5 Surface models

In this section, I will describe the methods used for describing phenomena at surfaces of a crystal. Surfaces of NiF_2 with various fluorine coverages are used as examples. In principle, there is an endless amount of possible ways to cut a crystal to create a surface. In practice, however, certain surface facets dominate due to their lower surface energy, γ,

$$\gamma = \frac{E_{\text{surf}} - E_{\text{bulk}}}{A} \tag{2.65}$$

which is the energetic cost to cut a surface of area A from the corresponding crystal. Generally, surfaces with many irregularities, such as kinks and steps, are less stable because of higher amounts of non-saturated surface atoms. In contrast, more stable surfaces tend to involve flatter structures with well-packed surface atoms.

In order to discuss various surface cuts and their relation to the underlying bulk crystal, the concept of Miller indices is useful.[160] A Miller index, (hkl), defines a plane which is associated with the surface normal vector $[hkl]$, where h, k and l are integers and multiples of the real space lattice vectors $\mathbf{x}$, $\mathbf{y}$ and $\mathbf{z}$.

$$[hkl] \equiv h\mathbf{x} + k\mathbf{y} + l\mathbf{z} \tag{2.66}$$

Fig. 2.7 shows three examples of crystal planes and their associated Miller indices for the rutile NiF_2. The (100) and (110) indices give rise to planes where the surface Ni atoms reside directly in the plane, whereas the (120) index contains some Ni atoms either above or below the plane. In other words, (100) and (110) surfaces will be more efficiently packed than (120) surfaces, and are expected to have a lower surface energy.[161] Oftentimes, the low-energy surfaces of a compound involve Miller indices $h, k, l \leq 2$ and are labeled low-index surfaces. Since the $\mathbf{x}$ and $\mathbf{y}$ directions are chemically equivalent in the rutile structure, many indices give rise to identical surfaces; the pairs (100)/(010), (101)/(011) and (120)/(210) all correspond to the same structures.

In this work, quantum-chemical calculations of surfaces will consistently employ two-dimensional periodic boundary conditions. Alternatively, surfaces may be modeled as non-periodic clusters of atoms, with the disadvantage that a large number of atoms is required to avoid artificial finite size effects.[162,163] Let the two periodic dimensions be described by the vectors $\mathbf{a}$ and $\mathbf{b}$ (which correspond to $\mathbf{a_1}$ and $\mathbf{a_2}$ in eq. (2.45). The Bloch theorem is applied analogously for the periodicity in the $\mathbf{ab}$ plane, and as a consequence

$$E_{\text{slab}} = E_{\text{slab}}(\mathbf{k_a}, \mathbf{k_b}) \tag{2.67}$$

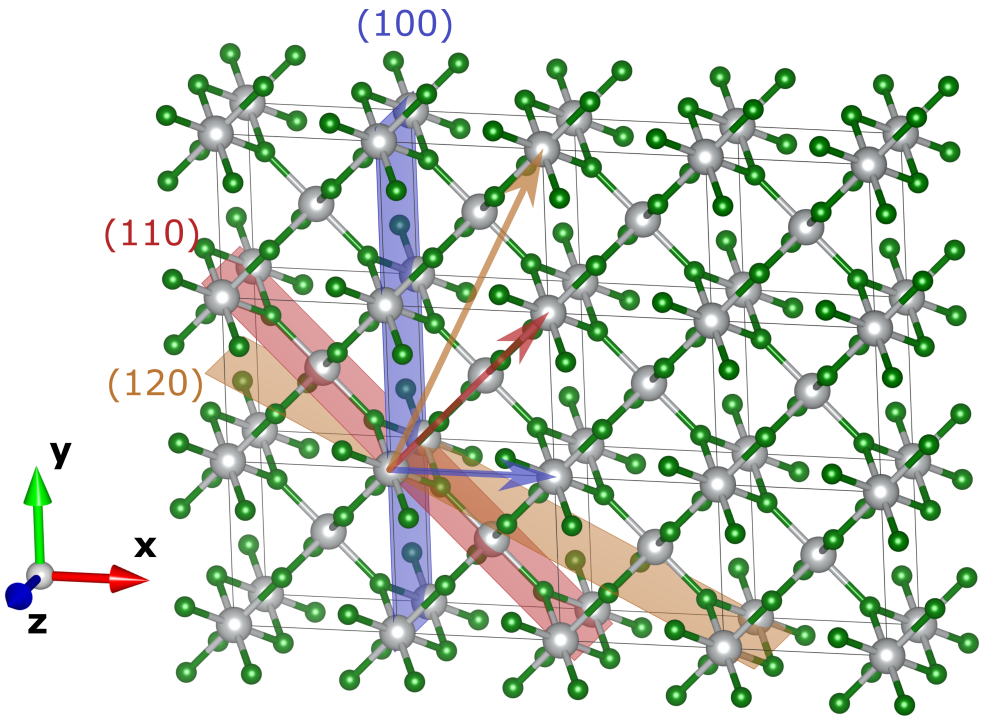

Figure 2.7: Planes described by the Miller indices (100) (blue), (110) (red) and (120) (orange) of NiF_2 in the rutile structure. The corresponding normal vectors [100], [110] and [120] are drawn in the same colors. The bulk crystal lattice is indicated in the figure, and is described by the lattice vectors **x**, **y** and **z**.

where E_{slab} is the energy of the two-dimensional periodic system (slab), and $\mathbf{k_a}$ and $\mathbf{k_b}$ are wave vectors that span the two-dimensional Brillouin zone. Let **c** be a vector pointing away from the **ab** plane. The slab is non-periodic in the **c** direction, and, as a consequence, it has a finite thickness and is terminated on two sides with surfaces.

An example slab for a NiF_2 surface is presented in Fig. 2.8a. The slab is divided into three parts: the "upper" surface, the "lower" surface, and the "bulk" region in the middle of that slab. If we are to properly model surfaces with slab models, the bulk region must be thick enough in order to avoid unwanted interaction between the two surfaces. For an infinitely thick slab, the energy per atom in the bulk region converges to the that of the bulk crystal.

Surface energies for a compound may be computed for slabs through

$$\gamma^{(hkl)} = \frac{1}{2A}\left[E_{\text{slab}}^{(hkl)} - N_{\text{s}}E_{\text{bulk}} - \sum_i N_i\mu_i\right] \tag{2.68}$$

where $E_{\text{slab}}^{(hkl)}$ is the energy of a slab with N_{s} stoichiometric units, and E_{bulk} is the

energy per unit of the bulk compound. N_i denotes the amount of atom i that is in excess ($N_i > 0$) or deficiency ($N_i < 0$) in the slab, relative to the stoichiometric compound. μ_i is the chemical potential of i in a reference state (*e.g.* hydrogen in H_2O or HF, or fluorine in HF). The excess or deficiency of an atom i is usually related to adsorption or desorption processes at the surface, and the extent to which this occurs depends on thermodynamical reservoirs of i. The factor of $(2A)^{-1}$ comes from the two surfaces that are included in the slab.

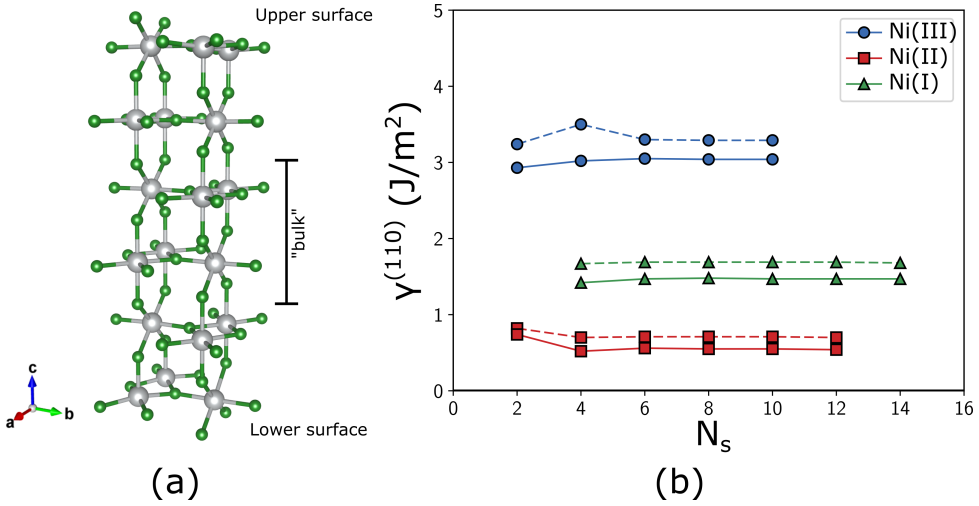

Figure 2.8: (a) Slab construction of the $NiF_2(110)$ surface (rutile structure). The slab extends periodically in the **ab** plane and is non-periodic in the **c** direction. The slab is terminated at both sides, inevitable leaving two surfaces (upper and lower). (b) Convergence of surface energies for increasing thicknesses of the $NiF_2(110)$ surface, as calculated with the PBE+U functional. Various oxidation states of the surface Ni ions are included. Solid (dashed) lines indicate relaxed (unrelaxed) slabs.

A requirement for eq. (2.68) to hold is that the upper and lower surfaces of the slab are chemically equivalent, *i.e.* symmetric with respect to inversion or an **ab** mirror plane. Importantly, this ensures that $\gamma^{(hkl)}$ refers to a single surface structure. Furthermore, if a plane wave basis set is used, the slab unit cell requires periodicity in the **c** direction, due to the periodic nature of plane waves. In this situation, a large enough **c** is needed to separate vertical slab images with a vacuum and avoid artificial interaction between slabs. Symmetric slabs decrease inter-slab interactions because of the elimination of intra-slab net dipole moments in the **c** direction.

Fig. 2.8b shows the behavior of γ for the $NiF_2(110)$ surface as the slab thickness is increased (higher N_s). Entries are included for three oxidation states of the surface Ni ions, due to varying fluorine coverages. In all cases, γ converges after a certain thickness, at $N_s \approx 8$ (*ca.* 12 Å).

For many crystal surfaces in inert environments (*e.g.* in vacuum), adsorptions of molecules do not occur, whereas desorption of atoms maybe neglected. Then the last term of eq. (2.68) may be omitted. On the other hand, if an external reservoir of some species i is present, its affinity for adsorption depends on the chemical potential of i in that reservoir under the given experimental conditions. *Ab initio* surface thermodynamics combines quantum chemical calculations with tabulated thermodynamical corrections in order to calculate surface structures as a function of *e.g.* temperature or partial pressure of an adsorbate.[164,165]

Generally, the chemical potential of a gas j is calculated according to

$$\mu_j(T, P_j) = E_j^{\mathrm{DFT}} + \Delta\mu_j^{\circ}(T)\Big|_{0\to T} + RT\ln\left(\frac{P_j}{P^{\circ}}\right) \tag{2.69}$$

with the assumption that j behaves as an ideal gas. E_j^{DFT} contains the electronic energy at 0 K, as well as zero-point vibrational energy. Extrapolations to temperature T and partial pressure P_j are performed by using tabulated data for the standard enthalpies and entropies (Shomate equation[166]).

If we consider the adsorption of fluorine onto NiF_2 surfaces, we express the chemical potential of F in equilibrium with the external reservoir containing F – in our case, liquid HF

$$\mu_{\mathrm{F}} = \mu_{\mathrm{HF,l}} - \mu_{\mathrm{H}} = \mu_{\mathrm{HF,l}} - \frac{1}{2}\mu_{\mathrm{H_2,g}} \tag{2.70}$$

where all equalities hold due to equilibria between HF, H and F, and between $^1/_2H_2$ and H. In section 2.6.1, I demonstrate how μ_{H_2} is a function of temperature, cell potential, H_2 partial pressure and acidity, in the equilibrium picture (see eq. (2.88)).

The liquid HF phase is challenging to model at the DFT level, due to its large conformational freedom. Therefore, we make the same assumption as in Section 2.6.1, that the Simons cell is an instantly equilibrating closed system, and disregard kinetic effects. This allows us to exploit the equilibrium

$$\mathrm{HF(l)} \rightleftharpoons \mathrm{HF(g)} \tag{2.71}$$

Anhydrous HF is used in Simons cells without considerable amounts of added electrolytes. If the mole fraction HF is close to unity, the vapor pressure of HF over the liquid phase is close to the vapor pressure of the pure compound (*cf.* Raoult's law).[167] It follows that

$$\mu_{\mathrm{HF,l}}(T) = \mu_{\mathrm{HF,g}}(T, P_{\mathrm{vap,HF}}) \tag{2.72}$$

where $P_{\mathrm{vap,HF}}$ is the vapor pressure of HF. DFT calculations of an HF molecule in the gas phase are trivial, and extrapolations of the gas-phase chemical potential to T

and $P_{\mathrm{vap,HF}}$ (which is a function of T; see the Antoine equation[168]) are possible with tabulated data.[169] Combining eq. (2.68) with the reference states for F adsorption – eqs. (2.69), (2.72) and (2.88) – we arrive at the total expression for the surface energy

$$\begin{aligned}\gamma(T,&P_{\mathrm{vap,HF}}, V, H_{0,\mathrm{HF}}) = \\ =&\frac{1}{2A}\Big[E_{\mathrm{slab}} - N_{\mathrm{s}}E_{\mathrm{bulk}} - N_{\mathrm{F}}\Big(\mu_{\mathrm{HF,g}}(T, P_{\mathrm{vap,HF}}) - \frac{1}{2}\mu_{\mathrm{H_2,g}}(T, V, H_{0,\mathrm{HF}})\Big)\Big]\end{aligned} \tag{2.73}$$

T and $P_{\mathrm{vap,HF}}(T)$ are set by the experimental conditions, typically around 0-15 °C.[8] The acidity of HF may for all practical purposes be assumed to be constant. Hence, the remaining thermodynamical variable is the cell potential V. With the surface energy reformulated for the single variable, the surface energy is expressed as

$$\gamma(V) = \gamma(V = 0) - \frac{N_{\mathrm{F}}eV}{2A} \tag{2.74}$$

where a linear correction term to $\gamma(V = 0)$ describes the cell potential dependence. The correction term is first introduced in eq. (2.86) and N_{F} refers to the number excess/deficiency F atoms per slab cell. Note that the surface energy of a stoichiometric surface (N_{F}) is independent of V, because no redox reactions are involved.

Fig. 2.9 shows the slab unit cells of the $NiF_2(110)$ surface: F-desorbed, stoichiometric and F-adsorbed. Periodic calculations require charge neutral cells, to avoid an infinite build-up of repulsive Coulomb interactions. Therefore, in the DFT calculation, formally a F atom is added to a Ni^{2+} site in a stoichiometric slab. After the electronic relaxation by the SCF procedure, electron density is spontanesouly transferred from the metal center, creating a Ni^{3+}–F^- surface motif. This effective oxidation of NiF_2 means we could view the addition of an F atom (the DFT picture) as the addition of F^- and removal of one electron (the electrochemical picture).

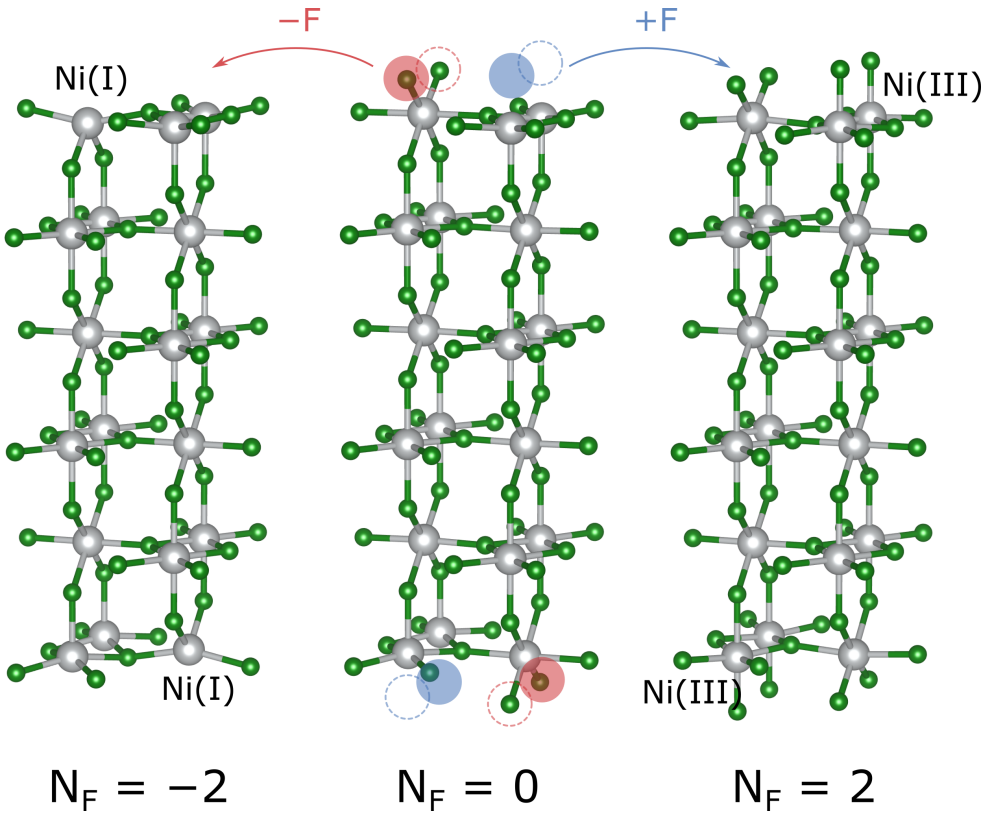

Figure 2.9: Unit cells for slabs of the $NiF_2(110)$ surface ($N_s = 12$). Note that, for a clearer representation of the structure, some symmetry-equivalent atoms are pictured twice, as they extend into the neighboring periodic image. A stoichiometric slab is shown in the middle. By removal of an F atom on each surface side, the oxidation state of Ni changes to Ni^+. The filled red circles denote the removed F atoms, and the dashed red rings denote the next periodic image of the removed atoms. Addition of F atoms to the free coordination site yields Ni^{3+} centers at the surfaces (blue circles and dashed rings).

2.6 Electrochemical models

The set-up of a typical Simons cell may be summarized as

$$\mathrm{Ni/Ni_xF_y/F^-, H^+/H_2/Ni} \tag{2.75}$$

where a slash denotes a phase boundary. The half-cell reactions are separated by a comma, which indicates that the electrolyte does not contain a phase boundary. The two Ni phases, as well as the anodic nickel fluoride film $\mathrm{Ni_xF_y}$, are solid, whereas the $\mathrm{F^-}$ and $\mathrm{H^+}$ ions are formed through the auto-protolysis of anhydrous HF. The solvation by HF means that the ionic species at the anode and cathode may be of the composition $[\mathrm{H_nF_{n+1}}]^-$ and $[\mathrm{H_{n+1}F_n}]^+$, respectively. The ion concentration, and consequently the electrolyte conductivity, is sometimes increased through addition of a fluoride salt, such as NaF.[18]

Electrochemical cells are inherently complex systems which must be understood at both microscopic and macroscopic scales. A key feature is the macroscopic electron transfer from anode to cathode, which establishes the coupled redox reactions associated with a cell. Hence, a real cell may not operate as an isolated half-cell reaction, and the flow of electric current is related to the relative potential difference between the electrodes.

$$V_{\mathrm{cell}} = V_{\mathrm{cat}} - V_{\mathrm{an}} \tag{2.76}$$

V_{cell}, multiplied by the elementary charge e, directly corresponds to the chemical energy extracted from a Galvanic cell (exergonic redox pair reactions) or transferred to an electrolytic cell via an applied potential (endergonic *dito*). V_{cell} is sometimes referred to as the electromotive force (emf) to stress the direction of the flowing current. The half-cell potentials, V_{an} and V_{cat}, are often expressed through the Nernst equation,[170] for example, for an anode

$$V_{\mathrm{an}} = V^0_{\mathrm{an}} + \frac{RT}{nF} \ln\left(\frac{a_{\mathrm{ox}}}{a_{\mathrm{red}}}\right) \tag{2.77}$$

where V^0_{an} is the half-cell potential of the anode at standard conditions, R is the ideal gas constant, n is the number of electrons transferred in the redox reaction, F is Faraday's constant, and a_{ox} and a_{red} are the activities of the oxidized and reduced species associated with the half-cell reaction (*e.g.* $\mathrm{Ni^{x+}}$ and $\mathrm{Ni^0}$ at the anode of a Simons cell).

The connection between cell potential and thermodynamics is clear by analysis of the potential-dependence of the Gibbs free energy for the reaction

$$\Delta G = -nFV \tag{2.78}$$

Note that this relation is commonly expressed for the total cell reaction, using the emf V_{cell}. However, this is not a restriction, and ΔG may refer to half-cell reactions and potentials, since $\Delta G_{\text{cell}} = \Delta G_{\text{cat}} + \Delta G_{\text{an}}$. From eq. (2.78), it is clear that the accessible thermodynamical work of a cell increases linearly with the potential difference of the electrodes.

In an electrolytic cell, an external potential V_{ext} is required to counter the negative redox potential of the cell (V_{redox}) such that

$$V_{\text{redox}} + V_{\text{ext}} > 0 \tag{2.79}$$

which yields $\Delta G_{\text{cell}} < 0$. Faraday's constant, F, is defined as the charge of one mol of electrons. Since V is an electric potential, an external potential may be understood as one unit of electric energy provided to the reaction per transferred electron. Such stoichiometric reactions involving redox pairs and transferred electrons are classified as faradaic processes. In Section 2.6.1, starting from thermodynamical arguments, I discuss the theoretical concepts used for modeling the faradaic part of the Ni_xF_y film formation.

In a real electrolytic cell, a multitude of *non*-faradaic electrochemical processes are present that involve current flowing without any occurring redox reactions. Two connected electrodes with a difference in electric potential will give rise to a polarization of the electrolyte through migration of charged species (anions, cations) through the solvent to the corresponding electrodes (anode, cathode).[171] As a consequence, electrode-electrolyte interfaces are formed as so called electric double layer (EDL) structures, as depicted for an ECF anode in Fig. 2.10.

The interface has a local electric potential, ϕ, at any point in space. Since we are interested in a two-dimensional surface, it is useful to average the local potential in xy planes (where xy is parallel to the surface), such that

$$\phi(z) = \iint \phi(x, y, z) dx dy \tag{2.80}$$

where z is the normal of the plane xy. A schematic of the function is plotted versus z in Fig. 2.10. At small values of z, the local potential approaches the electric potentials in pure Ni (with an external potential), whereas at large z, the electric potential is equal to that of the bulk electrolyte. These limiting values correspond to the electric potential difference in the thermodynamical equilibrium picture.

The polarization of the interface involves the formation of a charge density gradient from the metal surface to the bulk electrolyte, where the solvent acts as a dielectric. Some anions adsorb to the positively charged Ni surface (so called specific adsorption) and an inner Helmholtz plane (ihp) is formed. The roughly linear shape of $\phi(z)$ between the metal and the ihp indicates that the charge storage in this region behaves very much like a parallel-plate capacitor.[171]

$$C = \frac{q}{V} \tag{2.81}$$

where C is the capacitance affiliated with the double layer, q is the charge stored in the interface and V is the potential difference between metal and adsorbed ions.

Further away from the surface, the ion concentration drops continuously. This region is referred to as the diffuse layer, and is characterized by its non-capacitor-like charge storage and mobile ions.[172,173] The diffuse layer starts at the outer Helmholtz plane (ohp), which is the closest distance non-adsorbed anionic species approach the anode.[174] The layer may extend several nanometers from a metal surface, and its thickness is primarily governed by the ion concentration of the electrolyte (high concentrations enhance the dielectric screening which leads to a faster decay of $\phi(z)$).[175]

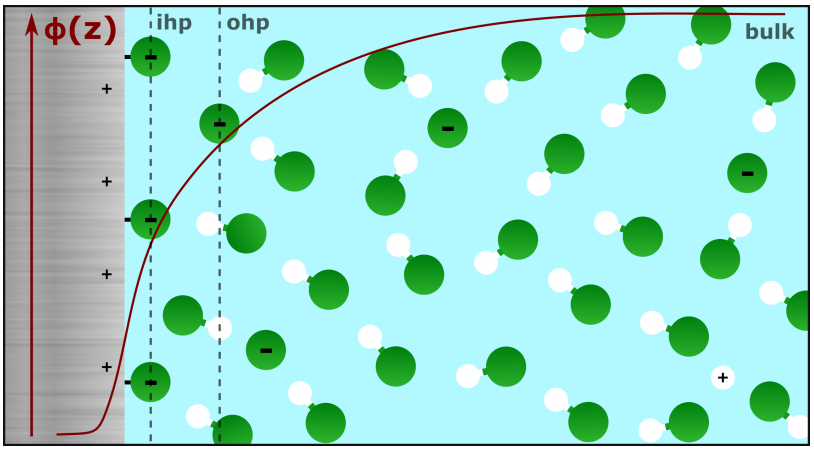

Figure 2.10: Schematic of the electric double layer structure of the anode in a Simons cell. The Ni surface is drawn to the left and H and F atoms colored white and green, respectively. The inner and outer Helmholtz planes mark the distance of specifically adsorbed F^- ions (ihp) and the start of the diffuse F^- layer (ohp). The plane-averaged local electric potential ($\phi(z)$) is plotted in red versus the distance from bulk Ni (z, not drawn). Its left boundary corresponds to the electrochemical potential of electrons in Ni and its right boundary the chemical potential of the bulk electrolyte. Due to the polarization, F^- ions at the ohp exhibit a lower potential difference than that of the pure Ni and electrolyte phases. Note that the extension of the various layers is not drawn to scale.

If an ion is to adsorb onto the metal surface, it needs to approach the surface at regions close to the ohp. Because of the potential gradient along z, the electric potential felt by the ion is lower than that of an ion in the bulk solution. Hence, it is less prone to adsorb to the surface than the standard potentials of the reaction would predict, since these are defined for the redox pairs in their pure phases.

EDL effects contribute to the so called overpotential of a cell, which is defined as the difference between the necessary potential required for the electrode reactions to take place and the thermodynamical minimal potential.[175] The thermodynamical interpretation discussed above and in Section 2.6.1 fails to describe the overpotential that arises from the EDL formation. Furthermore, it is by construction not intended for the description of the adsorption event at an electrode, since this involves explicit electron transfers, and possibly other kinetic effects from *e.g.* activation barriers. In Section 2.6.2, I discuss a model that is based on atomistic scale DFT calculations, which exploits an intrinsic flaw of periodic calculations (see Section 2.2) to describe the electron transfer event quantum-chemically. The potential dependence of adsorption is considered through the approximation of the electrode interface as a parallel-plate capacitor.

2.6.1 The computational hydrogen electrode

In electrochemical problems, one is mostly interested in a half-cell reaction. In principle, only information of the half-cell potential is required to study the thermodynamics of the half-cell reaction (eq. (2.78)). Unfortunately, half-cell potentials are not trivially measurable in experiments.

Therefore, potentials are mostly measured and reported *versus* a well-known reference electrode, such as the standard hydrogen electrode (SHE) or the saturated calomel electrode. An SHE is constructed according to

$$\mathrm{Pt/H_2/H^+} \tag{2.82}$$

where a Pt wire is placed in contact with a solution of 1 M H^+ (pH 0), and with a 1 bar pressure of H_2 bubbling through the solution. From international consensus, the half-cell potential of the SHE is defined as 0 V, to which all other half-cell potentials are defined as relative potentials. Standard potentials are available for many redox reactions, but are typically expressed for aqueous electrolytes.[98] However, standard potentials may vary significantly in other solvents,[176] which is especially problematic in strongly acidic anhydrous HF.

In order to express the thermodynamics of the faradaic processes in terms of cell potential, we consider the cathode reaction in a Simons cell

$$\mathrm{H^+ + ne^- \rightarrow \frac{1}{2}H_2} \tag{2.83}$$

First, we assume that the reaction is in equilibrium. This would imply that the cathode is constructed like an SHE with a 1 bar pressure of H_2 bubbling at the cathode interface. Note that the cathode material (SHE uses Pt, ECF uses Ni) does not participate stoichiometrically in the faradaic process, but rather acts as a catalyst

for hydrogen evolution. Hence, the choice of material influences the overpotential but not the redox potentials (eq. (2.78)).

In principle, the approximation deviates from real ECF experiments, where gaseous H_2 leaves the system (albeit at atmospheric pressure). Nevertheless, this assumption should be valid if the equilibrium is strongly shifted towards H_2 formation, such as in anhydrous HF where the chemical potential of H^+ is large.

From this approximation, we formulate the chemical potentials of the cathode species in equilibrium

$$\mu_{H^+} + \mu_{e^-} = \frac{1}{2}\mu_{H_2} \tag{2.84}$$

where μ_i is the chemical potential of species i. The complex quantities of the chemical potential of electrons within the cathode and protons in solution may be expressed simply in terms of molecular H_2.[177] The chemical potential at standard pressure is defined as

$$\frac{1}{2}\mu^\circ_{H_2}(T) = \frac{1}{2}E_{H_2} + \frac{1}{2}\Delta\mu^\circ_{H_2}(T)\Big|_{0\to T} \tag{2.85}$$

where E_{H_2} is the internal energy of a molecule, and $\Delta\mu^\circ_{H_2}(T)\Big|_{0\to T}$ is the change in chemical potential at temperature T relative to 0 K. E_{H_2} is calculated at 0 K including zero-point energy using DFT methods, whereas the enthalpy and entropy contributions are extrapolated to T using thermodynamical data tables for gaseous H_2.[178]

Since an external potential V simply shifts μ_{e^-} by 1 eV per transferred electron (eq. (2.78)), $\mu^\circ_{H_2}$ also has a linear dependence of V

$$\frac{1}{2}\mu^\circ_{H_2}(T,V) = \frac{1}{2}\mu^\circ_{H_2}(T,V=0) - eV \tag{2.86}$$

$\mu^\circ_{H_2}$ has been divided into one V-independent part as well as a correction term for the external potential.

The SHE is defined at pH 0, and this must be corrected for in anhydrous HF. The aqueous pH scale is only valid for when H_3O^+ is the dominant acidic species; in anhydrous HF, H_2F^+ dominates The Hammett acidity function H_0 provides a logarithmic scale of the chemical activity of H^+.[179]

$$H_0 = -\log\left(a_{H^+}\frac{\gamma_B}{\gamma_{HB^+}}\right) \tag{2.87}$$

where γ_i is the activity coefficient of species i. In our system, B = HF. In the range of low H^+ concentrations (pH 0-7), H_0 reduces to the pH scale, because γ_{HB^+} is close to unity. The use of H_0 allows for an extension of the pH scale to negative values,

and for anhydrous HF, $H_0 = -11$. Alternatively, omission of the H_0 correction yields a theoretical equivalent of the reversible hydrogen electrode (RHE), which is pH-independent.

With all corrections, $\mu^{\circ}_{\mathrm{H_2}}$ takes the shape

$$\frac{1}{2}\mu^{\circ,\mathrm{CHE}}_{\mathrm{H_2}}(T,V,H_0) = \frac{1}{2}\mu^{\circ}_{\mathrm{H_2}}(T,V,H_0=0) - RT\ln(10)H_0 \tag{2.88}$$

As presented in publication A3, the dominant term in $\mu^{\circ}_{\mathrm{H_2}}$ is the electronic energy, followed by the V-extrapolation term. In contrast, the temperature and acidity extrapolations only have a minor impact.

The superscript CHE in eq. (2.88) stands for the computational hydrogen electrode.[177,180] Studies employing the CHE formalism to study reactions at surfaces are manifold.[181–186] In Section 2.5, I describe how the CHE cell potential correction may be combined with *ab initio* surface thermodynamics to model electrochemical oxidation potentials for the chemical systems considered in this thesis.

2.6.2 Reaction modeling at absolute potentials

An alternative to expressing relative potentials is to completely disregard the counter or reference electrode and consider only the half-cell reaction of interest. Electron transfer processes must then be understood as functions of half-cell absolute potentials. Unfortunately, experimental measurements of absolute potentials are non-trivial. Efforts to measure the absolute potential of the SHE yield values between 4.2 and 4.5 V.[176,187,188] The reference state for such measurements is typically the electron ground state energy in vacuum.

Taking a fresh ECF anode as example, the absolute potential is equivalent to the electrochemical potential of electrons in Ni is defined as

$$\bar{\mu}^{\mathrm{Ni}}_{\mathrm{e}} = \mu^{\mathrm{Ni}}_{\mathrm{e}} - FV_{\mathrm{hc}} \tag{2.89}$$

where $\mu^{\mathrm{Ni}}_{\mathrm{e}}$ is the chemical potential of electrons in the Ni phase without an applied potential. V_{hc} is the applied half-cell potential bias at the anode, such that the total applied potential $V = V_{\mathrm{hc}} - V'_{\mathrm{hc}}$, where V'_{hc} is the half-cell potential bias of the counter or reference electrode. If the vacuum electric potential (ϕ_{vac}) is chosen as energy zero, then

$$\mu^{\mathrm{Ni}}_{\mathrm{e}} = E_{\mathrm{F}} - e\phi_{\mathrm{vac}} = -\Phi^{\mathrm{Ni}} \tag{2.90}$$

where E_{F} is the Fermi energy and Φ^{Ni} is the work function of Ni in contact with the electrolyte.[189] This choice of energy zero is particularly advantageous, since the quantities in eq. (2.90) are easily extracted from DFT calculations.

A key event in the half-cell reaction is the electron transfer from anode to cathode. This requires the number of electrons at an electrode to be variable and that an external reservoir of electrons is present (grand canonical ensemble).[190] This is not routinely possible in DFT SCF calculations, which are performed at constant number of particles, including electrons. Furthermore, periodic calculations require the unit cell to be charge-neutral. This means the removal of an electron is not possible without an added homogeneous background charge (jellium) which counters the positive charged cell.[191] A consequence of this is that ϕ_{vac} cannot be used as energy zero.

Nørskov and coworkers have presented a model for electrode reaction processes that exploits these shortcomings, and uses solely standard DFT calculations for the electronic structure.[189,192,193] Consider the adsorption of F^- on a Ni anode as an initial state (IS) and a final state (FS), as depicted in Fig. 2.11. Both states consist of a two-dimensional, periodic Ni slab which is covered by layers of explicitly solvating HF molecules (not specifically shown in the figure). The vacuum region separates the slab and is large enough so that ϕ_{vac} reaches a constant value, and Φ may be calculated.

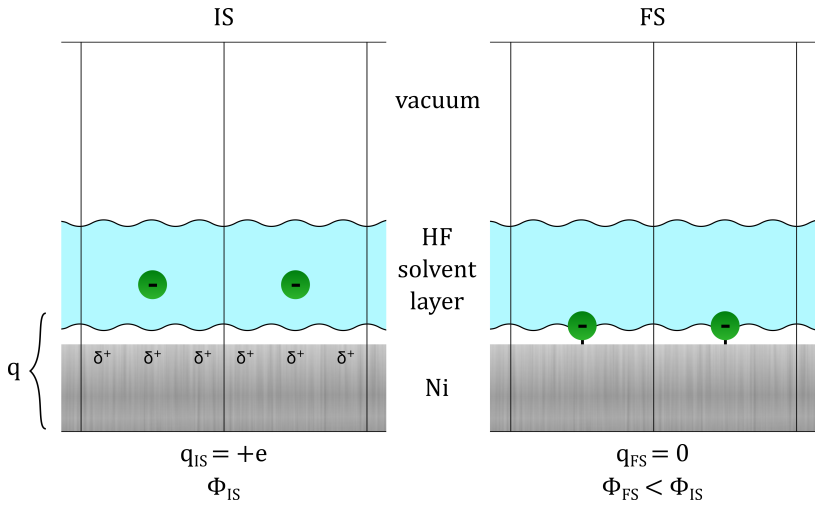

Figure 2.11: Schematic of the DFT supercells used to model the adsorption of F^- on a Ni anode. Two unit cells are depicted for the IS and FS, with one F^- per cell. The vacuum constitutes a common reference phase for the states. The ions are solvated in the HF solvent layer (blue). A slab is defined as Ni plus any specifically adsorbed species, and has the charge q. In the IS, the negative charge on F^- is countered by a delocalized positive charge on the Ni slab. In the FS, the slab is neutral. Φ_{IS} is significantly larger than Φ_{FS} due to the charged slab n the IS.

In the construction of the IS, the addition of an F atom to the HF solvent layer yields an electrified interface after the DFT calculation, where electron density is

transferred from the Ni slab, resulting in an F^- ion in the solvent layer and a positively charged Ni slab. The positive charge is delocalized close to the edge of the slab, whereas the negative charge is highly localized on F^-. Through this charge separation, we are able to describe the capacitor-like characteristics of the electric double layer in a DFT calculation. If we define the slab as Ni plus any specifically adsorbed species, we may quantify its charge q as a sum of the charge on all atoms belonging to the slab. Consequently, q is the charge stored in the capacitor. A positively charged slab has a depletion of occupied electronic states at the valence bands, which increases its work function Φ_{IS} (eq. (2.90)). By changing the concentration of F^- per Ni surface atom, we are able to indirectly shift Φ_{IS} to different values.

In the FS, F^- is specifically adsorbed and part of the charge-neutral slab. In other words, the capacitor has been discharged, since $q = 0$. Importantly, the work function changes significantly in going from the IS to the FS. This means a simple adsorption energy calculated from the DFT energies ($E_{\mathrm{DFT}} = E_{\mathrm{FS}} - E_{\mathrm{IS}}$) is a poor estimate to the adsorption energy in an electrochemical cell, since these operate at a constant potential ($\Phi_{\mathrm{IS}} = \Phi_{\mathrm{FS}}$). This error occurs due to the finite size of the supercell, and would vanish in the limit of an infinitely large cell; the shift in E_{F} is larger with a smaller pool of electrons in the Ni slab.

Rossmeisl *et al.* has shown that this limit may be reached using smaller supercells and an extrapolation scheme, with the H^+ adsorption on Pt(111) (aqueous solution) as model system.[189] In their methodology, the DFT energy of a state is divided into a "chemical part" and an "electrostatic" part

$$E_{\mathrm{DFT}} = E_{\mathrm{chem}} + E_{\mathrm{el}} \tag{2.91}$$

E_{el} is expressed as the energy of a parallel-plate capacitor – an assumption that is valid if there are not large rearrangements of dipole moments between the IS and FS

$$E_{\mathrm{cap}} = \frac{e^2\theta^2}{2C} \tag{2.92}$$

where e is the elementary charge and θ is the stored charge per unit cell, such that the unit of E_{cap} is consistent with E_{DFT}. C is the capacitance and is related to an applied potential V through

$$C = -\frac{e\theta}{V - V_{\mathrm{pzc}}} \tag{2.93}$$

where V_{pzc} is the potential of zero charge, *i.e.* potential at which the capacitor is uncharged. In experimental electrochemical cells, V_{pzc} is an electrode-specific quantity.[175] The difference in capacitor energy between the two states is expressed through eqs. (2.92) and (2.93)[192]

$$\Delta E_{\text{cap}} = E_{\text{cap,FS}} - E_{\text{cap,IS}} = e(q_{\text{FS}} - q_{\text{IS}}) \left[-(V_{\text{IS}} - V_{\text{pzc}}) - \frac{V_{\text{FS}} - V_{\text{IS}}}{2} \right] \tag{2.94}$$

which is defined as a unit energy per supercell (eq is the stored charge per supercell). The first term within the brackets refers to the extrapolation to potential V_{IS} from an uncharged interface. The second term corrects for the finite size of the cell.

We add the "chemical" energy on both sides of eq. (2.94)

$$\Delta E_{\text{chem}} + \Delta E_{\text{cap}} = \Delta E_{\text{chem}} - e\Delta q(V_{\text{IS}} - V_{\text{pzc}}) - \frac{e\Delta q \Delta V}{2} \tag{2.95}$$

where $\Delta q = q_{\text{FS}} - q_{\text{IS}}$ and $\Delta V = V_{\text{FS}} - V_{\text{IS}}$. The left hand side is simply the DFT reaction energy. Furthermore, we realize that the first two terms of the right hand side represent the adsorption energy at the constant potential of the IS, $\Delta E_{\text{ads}}(V_{\text{IS}})$. Since this is the sought-after unknown variable, knowledge about V_{pzc} is not required. By rearranging, and replacing the potential with the work function, we arrive at

$$\Delta E_{\text{ads}}(\Phi_{\text{IS}}) = \Delta E_{\text{DFT}} + \frac{\Delta q \Delta \Phi}{2} \tag{2.96}$$

where the first term is simply the difference in calculated DFT energy between the FS and IS, $\Delta E_{\text{DFT}} = E_{\text{FS}}(\Phi_{\text{FS}}) - E_{\text{IS}}(\Phi_{\text{IS}})$. Extrapolation to Φ_{FS} is possible by changing the sign of the last term. In principle, the two states are arbitrary, and other possible constant- and absolute-potential reaction energies may be acquired for transition states or reaction intermediates.

Finally, a simple linear relation of the Φ-dependence of ΔE_{ads} is possible by setting *e.g.* Φ_{IS} as a reference work function

$$\Delta E_{\text{ads}}(\Phi) = \Delta E_{\text{ads}}(\Phi_{\text{IS}}) - \Delta q(\Phi - \Phi_{\text{IS}}) \tag{2.97}$$

The slope of the function is simply $-\Delta q$, which is consistent with eq. (2.78) from Section 2.6.

The quantities in eqs. (2.96) and (2.97) may be calculated directly from two DFT calculations. Moreover, the cathode reaction may be modeled analogously. The total cell potential is the difference in work function

$$V_{\text{cell}} = \frac{\Phi_{\text{cat}} - \Phi_{\text{an}}}{e} \tag{2.98}$$

for which the total cell reaction energy is calculated

$$\Delta E_{\text{cell}}(V_{\text{cell}}) = \Delta E_{\text{an}}(\Phi_{\text{an}}) + \Delta E_{\text{cat}}(\Phi_{\text{cat}}) \tag{2.99}$$

Although the described method is grounded in well-established theories on electrode interfaces, limitations arise at the DFT level. Importantly, the self-interaction error (see Section 2.1.2) is an issue in electrified interfaces, since the delocalized charge at the metal surface is described more properly than the highly localized charge at the solvated ion (see Fig. 2.11). If this charge separation is to be described in a physically sound way using DFT, it is important that the frontier orbitals of the ion are well positioned relative to E_{F}.[194] Consider *e.g.* the anodic case, the eigenvalues of the frontier orbitals of F^- must be positioned so that

$$\varepsilon_{\mathrm{HOMO}}^{\mathrm{F}^-} < E_{\mathrm{F}} < \varepsilon_{\mathrm{LUMO}}^{\mathrm{F}^-} \tag{2.100}$$

where ε designates an orbital eigenvalue. If the HOMO orbital eigenvalue is too high, only a partial negative charge will be situated on the ion, and its eigenvalue will be situated at E_{F}. This problem is of higher significance if the metal has a high work function (low E_{F}), which is the case with Ni.[195] To avoid this problem, ions must be properly solvated so that the correct ionic state is reached. Alternatively, but at a higher computational cost, larger supercells may be used which shifts E_{F} to a smaller extent in the electrified interfaces.

Chapter 3

Publications

3.1 Paper A

"Density Functional Theory Calculations of Structural, Electronic, and Magnetic Properties of the 3d Metal Trifluorides MF_3 (M = Ti-Ni) in the Solid State"

Mattsson, S. and Paulus, B., *J. Comput. Chem.*, 2019, **40**, 1190–1197.

DOI: 10.1002/jcc.25777
URL: http://www.doi.org/10.1002/jcc.25777

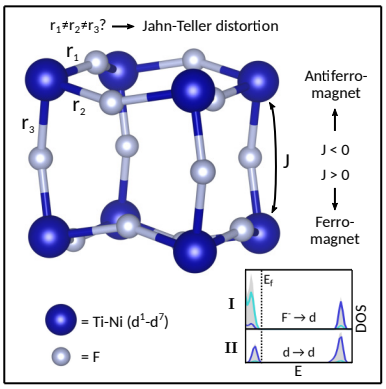

Graphical abstract of Paper A.

Contributions: The idea of a comparison study of the trifluorides was developed by Beate Paulus and me to similar extent. DFT calculations and analysis of the data were performed by me. Writing and revisions of the paper were done by me, with support from B.P.

3.2 Paper B

"A theoretical study on the binding and electrolytic splitting of hydrogen fluoride on Ni(111) and Ni(211)"

Mattsson, S. and Paulus, B., *Phys. Chem. Chem. Phys.*, 2020, **22**, 4407–4415.

DOI: 10.1039/c9cp06348j
URL: http://www.doi.org/10.1039/c9cp06348j

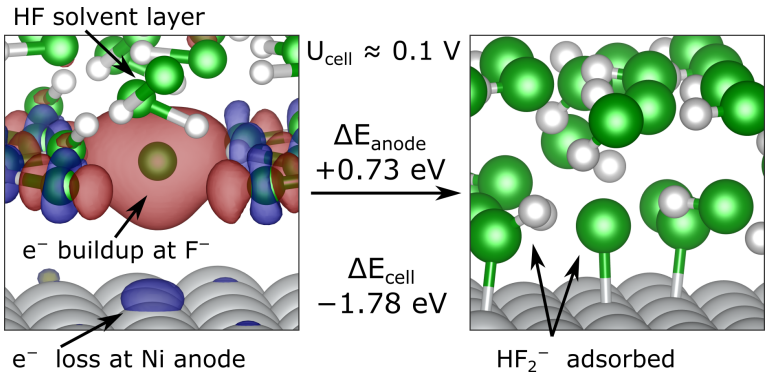

Graphical abstract of Paper B.

Contributions: The original idea of half-cell reaction modeling at constant potentials was a contribution from Beate Paulus. The setup including both electrodes was designed by me and I performed the DFT calculations. Writing of the manuscript, including revisions, was done by me, with support from B.P.

3.3 Paper C

"Combining theory and experiment to characterize the voltammetric behavior of nickel anodes in the Simons process"

Mattsson, S.; Senges, G.; Riedel, S. and Paulus, B., *Chem. Eur. J.*, accepted manuscript.

DOI: 10.1002/chem.202000881
URL: http://www.doi.org/10.1002/chem.202000881

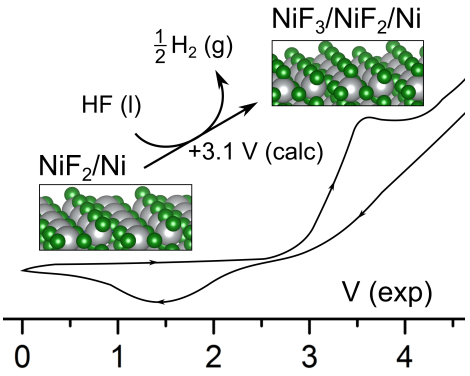

Graphical abstract of Paper C.

Contributions: The concept of using known nickel fluorides as starting point for disordered Ni_xF_y structures was developed by Beate Paulus and me in cooperation. The model for calculations of surface stabilities at typical experimental conditions was developed by me. DFT calculations and raw data analyses were performed by me. Experiments were conceptualized by Gene Senges and Sebastian Riedel, and the cyclovoltammetry experiments were performed by G.S. All authors were involved in the interpretation of the results. The manuscript was written by G.S. (experimental parts and introduction) and me (theoretical parts and discussion), with support from S.R. and B.P.

3.4 Paper D

"Ab initio molecular dynamics studies on the adsorption of hydrogen fluoride on Ni(111)"

Mattsson, S. and Paulus, B., manuscript submitted.

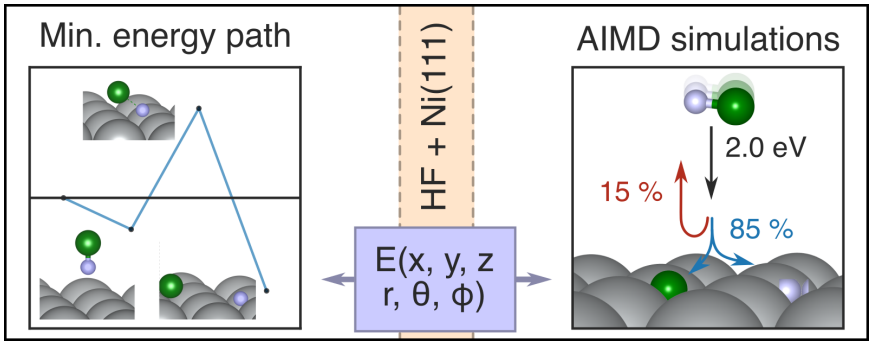

Graphical abstract of Paper D.

Contributions: The idea of a molecular dynamics treatment of HF adsorption on nickel was Beate Paulus'. DFT calculations were performed by me. Analysis of potential energy surfaces and trajectories was done by me. The manuscript was written by me, with support from B.P.

Ab initio molecular dynamics studies on the adsorption of hydrogen fluoride on Ni(111)

Stefan Mattsson* and Beate Paulus

Institute of Chemistry and Biochemistry, Physical and Theoretical Chemistry, Freie Universität Berlin, Arnimallee 22, 14195 Berlin, Germany

E-mail: stefan.mattsson@fu-berlin.de

Abstract

The formation of an insulating nickel fluoride film on a nickel surface in contact with hydrogen fluoride (HF) is predicted to cause the low-voltage passivation of Ni anodes used in the Simons process. In this work, we examine the energetics of the activation of a single HF molecule adsorbing onto a Ni(111) surface using density functional theory with periodic boundary conditions. First, we calculate structures and energies of the minimum energy path towards chemisorption: physisorption intermediates, transition states and chemisorbed products. The calculated energies of the transition states are in the order of 280 meV and the chemisorption is found to be exothermic by around –800 meV, suggesting a surmountable activation barrier for chemisorption. To learn more in detail about the mechanism of the chemisorption, we additionally consider the adsorption of HF as a simulation of a molecular beam experiment by using ab initio molecular dynamics. Through analysis of the trajectories, the position of the center of mass of the HF molecule, upon collision with the Ni surface, is the most important factor for the probability of chemisorption. By comparison of the chemisorpion probability of an incoming HF molecule with the minimum energy path, we find that favorable HF impact angles for chemisorption do not correspond to the minimum energy path, due

to the difference in mass between hydrogen and fluoride. The data points from the molecular dynamics simulations are fed into a neural network in order to fit potentials for the six-dimensional PES of HF on Ni(111), which are discussed.

Introduction

The Simons process is a popular method for the industrial synthesis of perfluorinated organic molecules, owing to its ability to avoid the use of hazardous, strongly oxidizing F_2.[1–3] A type of electrochemical fluorination, the Simons process utilizes anodic current for the oxidation of the organic substrate, which is dissolved in anhydrous hydrogen fluoride (HF). Anhydrous HF is used as electrolyte and constitutes the fluorine source. The method is known to only function with Ni or some alloys of Ni as the anode material.[3] A crucial step in the Simons process is the formation of a highly oxidized nickel fluoride film of unknown composition, which subsequently fluorinates the organic substrates.[4]

Cyclovoltammetry measurements of Ni electrodes in anhydrous HF are characteristic for a large onset of anodic current at high cell potentials around 3 V.[3,5–8] This is also the potential required for the perfluorination of organic substrates. Some polarization experiments show a smaller oxidation peak at lower cell potentials around 0.5 V, possibly from the oxidation of metallic Ni to NiF_2.[5,6] The small size of the peak may indicate that the formed species is insulating, which is likely if a NiF_2 film is formed. Dimitrov et al. found that the peak is absent if anodes were not thoroughly cleaned prior to usage, so that the metallic Ni surface is exposed.[8]

An electrochemical mechanism for the initial fluorination of the Ni(111) surface has been subject to previous theoretical work by us.[9] However, an alternative possibility is the spontaneous fluorination of Ni when the metal is in contact with anhydrous HF, leading to anodic passivation below 3 V. Since the stoichiometric formation of NiF_2 and H_2 from Ni and HF is exergonic by –552 meV at standard conditions,[10] the non-electrochemical fluorination of Ni is conceivable, at least from a thermodynamical point of view. This mechanism is also

supported by findings of metallic Ni to spontaneously form a NiF_2 film both under an atmosphere of HF but also when exposed to liquid anhydrous HF.[11]

Molecular dynamics calculations would be an ideal theoretical approach towards a better understanding of HF/Ni interfaces and the adsorption of molecules on the surface. Ab initio molecular dynamics (AIMD) would, in principle, be an excellent choice because of the explicit quantum chemical treatment which is crucial for the description of chemisorption of molecules and surface-catalyzed reactions between adsorbed atoms. However, AIMD simulations of large supercells with hundreds of atoms (Ni slab and HF solvent layers), at femtosecond resolution, are not realistic with today's computational capacities. Force field methods are an affordable alternative, and are applicable over longer simulation times. The liquid phase of anhydrous HF is well-understood and proper force fields exist which take into consideration hydrogen bonding and the polarity of the solvent.[12,13] However, although for example reactive force fields have been a developing subject in recent years,[14–17] transferability is still a problem, and oftentimes researchers develop accurate reactive force fields for their specific system. A solution for an HF/Ni interface is the division of the nuclear degrees of freedom where all HF–HF interactions are treated with classical force fields and all HF–Ni interactions are described at a higher level, for instance with potentials fitted to ab initio calculations using a neural network (NN).[18,19]

Before any complex interfaces involving liquid HF may be modeled in this way, we require a better understanding of the fundamental interactions between HF and Ni. More specifically, in this work, we want to elucidate the mechanism of the adsorption of a single HF molecule on the most commonly occurring Ni(111) surface. The adsorption reaction consists of two steps: 1) barrier-free physisorption of HF without bond breakage and 2) chemisorption of H and F over an energetic barrier. Points of interest are stable adsorption sites, HF physisorption and chemisorption, transition state (TS) structure and energy, as well as reactive channels towards chemisorption. To describe these processes, it is necessary to address all six nuclear degrees of freedom of the HF molecule. Density functional theory

(DFT) provides a formalism for electronic structure calculations where the electron density is treated explicitly quantum-mechanically, with approximate exchange-correlation functionals. Energies from DFT calculations are routinely used in various algorithms for location of saddle points or minimum energy paths on the PES.[20]

In this work, we study the interaction between HF and the Ni(111) surface using both electronic structure and molecular dynamics approaches. A minimum energy reaction profile for chemisorption is calculated with reactants, physisorbed intermediates, TSs and products. The method has previously been applied in similar studies on the activation of small molecules on metal surfaces.[21–26]

Furthermore, we explore the potential energy surface of the HF/Ni(111) system, specifically paths leading to chemisorption. For this, we perform AIMD simulations that mimic a molecular beam experiment of a Ni surface bombarded by gaseous HF molecules with a certain kinetic energy. Several previous studies have, in the same manner, considered such simulations with other small, less reactive molecules and metal surfaces, such as H_2 on Ni(111),[27] H_2 on Pt(111) and Pt(211),[28] HCl on Au(111),[26,29] H_2O on Ni(111)[30] and CHD_3 on Ni(111).[31,32] The trajectories are analyzed, and some structural features are identified for an HF molecule in close vicinity to the surface that impact the chemisorption probability. We also discuss similarities and differences between the minimum energy path and the AIMD trajectories of chemisorbed molecules. The data points from the AIMD simulations are fed into a neural network (NN) and used to fit a six-dimensional PES to further elucidate possible reaction channels towards chemisorption.

Computational methods

DFT calculations are performed using the plane-wave-based Vienna ab initio simulation package (VASP) version 5.4.1.[33,34] Pseudopotentials of the projector-augmented wave type are used for the description of core electrons.[35] Valence electron shells (H: 1s, F: 2s, 2p, Ni:

3d, 4s, 4p) are treated explicitly within the Kohn-Sham formalism of DFT. The orbitals are expanded in a basis set of plane-waves with kinetic energies up to a cutoff of 600 eV. The energy convergence criterion for the self-consistent field procedure is set to 0.001 meV. Convergence is accelerated by using Methfessel-Paxton smearing with a temperature factor of 0.1 eV. We employ the exchange-correlation functionals with the generalized-gradient approximation (GGA), according to Perdew, Burke and Ernzerhof (PBE),[36] the revised PBE functional (revPBE),[37] the Lundqvist dispersion functionals vdW-DF[38] and vdW-DF2,[39] as well as the PBE functional with empirical D3 dispersion correction and Becke-Johnson damping,[40,41] with the majority of the calculations utilizing the vdW-DF functional.

For HF+Ni systems, slabs based on a $p(3 \times 3)$ supercell of Ni(111) are used to decrease interaction between periodic images of HF. 4 layers of Ni are used and a vacuum of 20 Å separates the Ni slabs to decouple interactions between periodic images of the slabs. k point sampling of the first Brillouin zone is done using a Monkhort-Pack grid of $9 \times 9 \times 9$ for bulk Ni, $5 \times 5 \times 1$ for the slabs and $1 \times 1 \times 1$ for the isolated molecules HF, H_2 and F_2. With the energy cutoff, slab thickness and k point density, the binding energy of a single F atom adsorbed on Ni is converged within 1.5 meV.

All structure optimizations are performed until the atomic forces are no larger than 0.01 eV/Å. For bulk Ni, this results in a calculated lattice constant of 3.565 Å, in good agreement with the experimental value 3.52 Å.[42] In all structure optimizations of slabs, the supercell parameters are kept constant whereas the atoms are allowed to relax. Clean Ni(111) slabs are relaxed, after which they are kept frozen in systems with HF, H or F as adsorbates. Transition states are calculated with the DIMER method using an implementation part of the VASP transition state tools (VTST) program suite.[43–45] The method uses two slightly displaced images (a "dimer") of nuclear coordinates, from which energies and forces are calculated to approximate the curvature of the PES. The "dimer" is translated and rotated so that it approximately follows the flattest vibrational mode, while minimizing the energy with respect to the remaining steeper modes. Imaginary frequencies of transition states are

evaluated by frequency calculations.

AIMD calculations are performed as NVE ensembles with a time step of 0.5 fs. The Ni surface is static and initial forces on the H and F atoms are generated from the vibrational ground state and the supplied momentum of the molecule, in a quasi-classical picture.[46] The HF molecule is placed 8 Å from the surface. A molecule is considered chemisorbed if $r > 2.4$ Å and scattered if $z > 8.0$ Å (for the definition of the coordinate system, see Figure 1 below). Static single-point calculation scans of the r-z PESs used in the NN fit and fit accuracy evaluation are performed on a non-uniform grid with discrete values $r = \{0.4, 0.5, 0.6, ..., 1.9, 2.0, 2.2, 2.4, 2.8\}$ and $z = \{0.8, 1.0, 1.2, ..., 3.4, 3.6, 4.0, 4.5, 5.0, 6.0, 7.0, 8.0\}$.

Bader charges are calculated using an external program from the VTST suite.[47] Visualizations of molecular structures are produced with the VESTA 3.4.4 program.[48]

Results and discussion

A p(3×3) supercell of the Ni(111) surface is constructed and structurally relaxed. After this and throughout this work, the surface is treated as static (frozen-surface approximation) which reduces the number of degrees of freedom of the HF molecule on the Ni(111) surface to six. In Figure 1 the six dimensions are specified. (u, v) describe the horizontal position of the center of mass of the HF molecule as fractions of the Ni(111) surface unit cell. The two coordinates are defined relative to a reference Ni atom in the top layer

$$\begin{aligned} u &= \frac{x - x_{\text{ref}}}{|\vec{a}|} - \frac{v}{2} \\ v &= \frac{2(y - y_{\text{ref}})}{\sqrt{3}|\vec{b}|} \end{aligned} \tag{1}$$

where $\vec{a}$ and $\vec{b}$ are the lattice vectors of the Ni(111) surface unit cell. The high-symmetry points of the Ni(111) surface (Figure 1, left) are: the top $(0, 0)$, hcp $(\frac{1}{3}, \frac{1}{3})$, fcc $(\frac{2}{3}, \frac{2}{3})$ and bridge $(\frac{1}{2}, 0)$ sites. z is the vertical coordinate and is the distance between the HF center

of mass and the topmost Ni layer. The polar and azimuthal angles θ and φ describe the orientation of the HF molecule. The H–F distance is described by r.

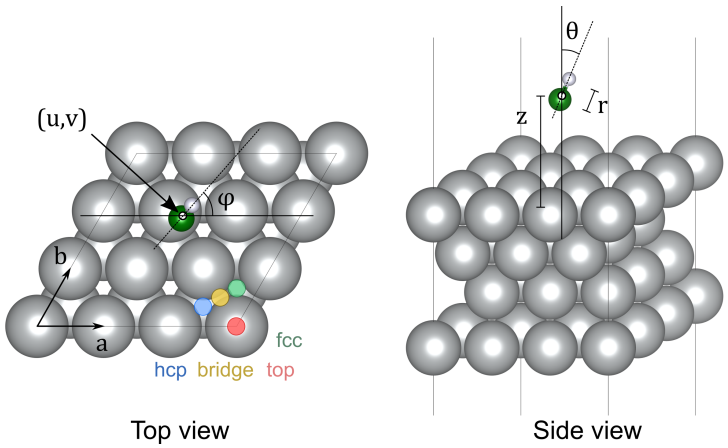

Figure 1: Coordinate system used for the HF molecule on p(3×3) Ni(111). The p(1×1) cell is described by the lattice vectors $\vec{a}$ and $\vec{b}$ in the surface plane. The position of the HF center of mass (white dot) is described by the fractional coordinates u and v, and the distance z. r denotes the bond length, θ the polar angle and φ the azimuthal angle of the molecule. Also presented are the four high-symmetry adsorption sites of Ni(111) as colored circles: fcc, hcp, bridge and top.

Adsorption reaction steps

To evaluate the quality of the different exchange-correlation functionals with respect to molecular properties, as well as the adsorption on Ni, various properties are determined and shown in Table 1. The calculated bond lengths (minimum of the PES along the bond coordinate r) and zero-point energies (E_{ZPE}) refer to of an HF molecule in vacuum. Anharmonicity effects of the ro-vibrational eigenvalues are taken into consideration by the discrete variable representation (DVR) formalism,[49] by diagonalization of the Hamiltonian matrix in the time-independent nuclear Schrödinger equation. The calculated ZPEs refer to the ro-vibrational ground state ($v=0$, $J=0$). The experimental ZPE is taken as the fundamental frequency of HF. All functionals give similar results with respect to r_{vac} and E_{ZPE}, with the

vdW-DF2 functional giving a slightly lower ZPE. The given results are in line with values reported in previous studies using GGA functionals.[50]

The physisorption energy (ΔE_{phys}) is defined as the energy of the bound HF/Ni system minus the energies of the isolated molecule and the clean Ni surface, neglecting the change in ZPE. Using all functionals, ΔE_{phys} is calculated for an HF molecule at the fcc site with the molecule perpendicular to the Ni surface, the hydrogen facing the fcc site (the global minimum for physisorption; see below). The binding shows some electrostatic characteristics, which are reflected in the negative sign of ΔE_{phys} in the PBE and rPBE functionals, which account for dispersive effects poorly. It is known that PBE tends to overestimate the binding energy of molecules at metal surfaces, whereas the revPBE functional tends to underestimate it.[51,52] Inclusion of the Lundqvist non-local dispersion functional in the revPBE functional gives vdW-DF, which increases binding by about a factor of around 2. vdW-DF2, which is based on the rPW86 exchange functional, gives a very similar physisorption energy. The inclusion of the semi-empirical atom-centered Grimme dispersion correction D3(BJ) to the PBE functional gives the strongest binding. However, it has previously been indicated that the Grimme-type correction schemes lead to overbinding in metal/small molecule interfaces.[52] Therefore, the vdW-DF functional is picked for all further DFT calculations due to the slightly more accurate E_{ZPE}.

Table 1: Evaluation of exchange-correlation functionals. Calculated bond lengths (r_{vac}) and zero-point energy (E_{ZPE}) refer to HF in the gas phase. In all cases, E_{ZPE} is calculated at the anharmonic level and refers to the ro-vibrational ground state. The physisorption energy is calculated for an HF molecule perpendicular to the surface, with H pointing down towards an fcc site. z_{phys} refers to the distance between the surface and the HF center of mass of these structures.

Functional	r_{vac} [Å]	E_{ZPE} [meV]	ΔE_{phys} [meV]	z_{phys} [Å]
PBE	0.938	235	–152	3.023
revPBE	0.937	235	–69	3.262
vdW-DF	0.937	235	–181	3.181
vdW-DF2	0.939	230	–184	3.156
PBE-D3(BJ)	0.938	235	–275	2.903
Exp.[53]	0.917	254	-	-

All structure optimizations in the physisorption region, $z \approx 3$, result in a perpendicularly ($\theta = 180°$) oriented HF molecule with the hydrogen end pointing towards a high symmetry site. This minimizes repulsion between the localized electron density at the fluorine end and the delocalized electron density of the valence band at the Ni surface. Furthermore, there is a small transfer of electron density from the Ni surface to the LUMO of the molecule. For the fcc physisorbed structure, the charge transfer is quantified to $-0.08e$ (e is the elementary positive charge) from a Bader analysis calculation, and is the reason for the elongated r in the physisorption structures, as presented in Table 2. This physisorption proceeds similarly at the fcc and hcp sites with binding energies of –181 meV that differs only in the first decimal place (–0.4 meV lower for fcc), and with similar elongated r. Physisorption at the top site also occurs with $\theta = 180°$ in a local minimum with the binding energy –154 meV. Due to the high symmetry of the Ni(111) surface (see Figure 1), the minima at the fcc and hcp sites may be considered two pseudo-degenerate global minima for physisorption within our system and calculation parameters.

The minimum energy path on the PES towards chemisorption provides first crucial information about the mechanism and energetics involved in the splitting of HF on Ni(111). The DIMER method provides an efficient way of acquiring saddle points on the PES without the need of structures of either the initial or the final conformation separated by the TS, unlike the nudged elastic bands (NEB) method.[43–45] A further advantage is that the method leaves out the calculation of second derivatives Hessian matrices, which are not numerically available for plane-wave basis sets. DIMER calculations are performed with all six degrees of freedom. Two TSs are found, depending on whether the fcc or hcp physisorption structure is used as starting point. Frequency calculations give one imaginary frequency for each TS which confirms that both are of first order. In both cases, the fluorine atom is positioned slightly off from a top position with the hydrogen atom pointing towards an fcc or hcp cavity (shown in Figure 2 for the fcc case). In previous DFT studies, this type of coordination is also found in the TSs of the first bond dissociation of H_2O and CH_4 on Ni(111).[30,31] In

these studies, the remaining hydrogen atoms point away from the surface and do not directly participate in the dissociation.

The r values are similar between the TSs. At 1.382 Å and 1.378 Å, the bond is elongated by 47 % relative to the gas phase value, which is fairly large and characteristic of a late TS. The energetic barriers, $E^{\ddagger}$, at 514 meV and 505 meV indicate that HF is relatively easily activated on Ni(111) via the calculated TSs. The catalytic capacity of the Ni surface is highlighted by comparison with the bond dissociation energy of an isolated HF molecule, 5.856 eV.[54] To the extent of our knowledge, no comparable metal-surface-mediated activation energies for HF adsorption exist in the literature. Kay et al. experimentally studied the desorption of HF from Au(111),[55] but their work was centered around the desorption of hydrogen-bonding HF layers, which is poorly comparable to single molecule adsorption. Desorption experiments of low-coverages of HF on Pt(111) were performed by Wagner et al. but the molecules were found to be only physisorbed, since no decomposition products were found.[56] The absence of chemisorption is conceivable for a noble metal like Pt.

Careful comparisons may be done with previous DFT calculations of $E^{\ddagger}$ of the first bond dissociation of water or methane on Ni(111). In a study by Jiang et al., $E^{\ddagger}$ of the analogous H_2O activation was calculated as 670 meV through a NN PES fit on the basis of PW91 DFT calculations.[30] Nattino et al. calculated the $E^{\ddagger}$ for CHD_3 at 1010 meV using the climbing image nudged elastic bands method and the vdW-DF functional.[32] Comparisons with NH_3 should be avoided since the molecule has a strong pre-dissociation adsorption minimum at the top site of Ni(111), unlike the primarily van der Waals-bound HF molecule.[57]

It should be noted that the energy of the reference state (HF in vacuum, clean Ni(111) surface) is defined in the same way as the mentioned water and methane adsorption studies.[30,32] This allows for direct comparison with those studies, and $E^{\ddagger}$ is more consistent with the molecular beam simulations further on, in which the HF molecule is initially placed far from the surface. For a molecule which is bound in the physisorption minimum, the barrier

is calculated according to

$$E^{\ddagger}_{\mathrm{phys}} = E^{\ddagger} - E_{\mathrm{phys}} \tag{2}$$

which gives increased barriers 695 meV (fcc TS) and 687 meV (hcp TS).

Additionally, the calculated ZPE may be added to the HF molecule. For the HF in vacuum reference state

$$E^{\ddagger}_{\mathrm{vib}} = E^{\ddagger} - E_{\mathrm{ZPE}} \tag{3}$$

We recall that E_{ZPE} is calculated at the anharmonic level. This decreases $E^{\ddagger}$ by 235 meV, giving the low barriers 279 meV (fcc TS) and 271 meV (hcp TS). Alternatively, the ZPE may be included for the physisorbed HF as reference state

$$E^{\ddagger}_{\mathrm{phys,vib}} \approx E^{\ddagger}_{\mathrm{phys}} - E_{\mathrm{ZPE}} \tag{4}$$

under the assumption that E_{ZPE} due to the HF stretching vibration changes only little between a physisorbed molecule and one in vacuum. Due to the slight increase in r for a physisorbed molecule, the ZPE is expected to be slightly smaller which would lead to a small underestimation of $E^{\ddagger}_{\mathrm{phys,vib}}$ by Eq. (4). The calculated values for $E^{\ddagger}_{\mathrm{phys,vib}}$ are 460 meV (fcc TC) and 452 meV (hcp TS).

Chemisorbed structures are acquired by displacement of the H and F atoms along the imaginary mode of the TS. The bond dissociation proceeds with the H atom remaining at the cavity to which it coordinated in the TS (see Figure 2 for the fcc case). The F atom migrates to the opposite site (the hcp site in the figure), so that the top Ni atom separates the chemisorbed atoms. This chemisorption mechanism centered around a top atom of the Ni(111) surface is analogous to the paths found for H_2O and CH_4.[30,31] Chemisorption is found to be exothermic over both TSs, by quite a significant amount. The hcp TS leads to an energetically slightly lower chemisorbed structure of –567 meV. The reverse reaction corresponds to the desorption of H and F and formation of gaseous HF. The calculated activation energy of desorption are 1.048 eV and 1.073 eV for the fcc and hcp TS paths,

respectively, indicating a large kinetic barrier.

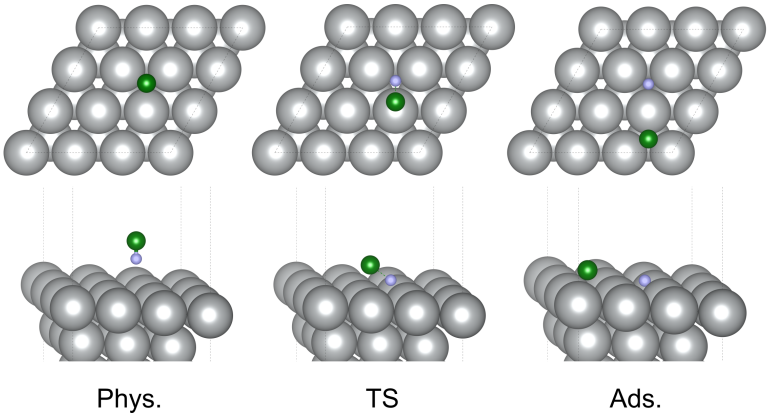

Figure 2: Reaction path to chemisorption of HF on Ni(111) via the fcc transition state ($\varphi = 90°$). The structural parameters are presented in Table 2. Calculated with vdW-DF.

Furthermore, we comment on the cases of F or H adsorbed on a Ni(111) surface, in the same p(3×3) supercell. This is, in effect, a sum of the reactions 1) adsorption of HF and 2) desorption of H (F) and formation of F (H) bound to the surface. The energy of the desorbed atom is calculated as the energy of gaseous H_2 and F_2 molecules. A description of the kinetics of the desorption reaction of the individual atoms is beyond the scope of this work, and the calculated values are referring to states in equilibirum. The single-atom binding energies are calculated according to

$$\Delta E_{\mathrm{at}} = E_{\mathrm{Ni+H(/F)}} + \frac{1}{2} E_{\mathrm{F_2(/H_2)}} - E_{\mathrm{Ni}} - E_{\mathrm{HF}} \tag{5}$$

where $E_{\mathrm{Ni+H(/F)}}$ refers to the energy of H (or F) adsorbed on Ni and $E_{\mathrm{F_2(/H_2)}}$ refers to the energy of an F_2 (or H_2) molecule.

In Table 3, ΔE_{at} values are listed for F and H adsorption at the minima found at the high-symmetry sites of the surface. Atoms at the bridge site always relax to the nearby fcc site upon structure optimization. Adsorption of H and creation of F_2 is, as expected, highly endothermic, due to the extreme oxidizing properties of F_2. Nevertheless, from the differences

Table 2: Structural parameters and reaction energies for the reaction step towards chemisorption via transition states over the fcc or hcp site. ΔE_{rxn} refers to the binding energy relative to the separate HF and Ni(111) species. Physisorption structures are acquired by structure optimization of an HF molecule on Ni(111). Transition states are calculated using the DIMER method. Chemisorption structures are acquired by relaxation of the TS with a small displacement along the imaginary frequency. Calculated with vdW-DF.

Step	ΔE_{rxn} [meV]	u	v	z [Å]	r [Å]	θ [°]	φ [°]
Reactants	0	-	-	-	0.937	-	-
Reaction via fcc TS							
Physisorbed	–181	–0.333	0.667	3.181	0.950	180.0	-
Transition state	514	–0.119	0.238	1.942	1.382	127.7	90.0
Chemisorbed (F hcp, H fcc)	–534	0.334	0.333	1.505	3.158	101.4	90.0
Reaction via hcp TS							
Physisorbed	–181	0.333	0.333	3.232	0.949	180.0	-
Transition state	506	0.745	0.128	1.962	1.378	128.4	150.0
Chemisorbed (F fcc, H hcp)	–567	0.978	0.682	1.479	3.089	101.2	150.0

between ΔE_{at}, we may deduce that the hollow sites are strongly favored for the adsorption of a single H atom, compared to the top site. Interestingly, the adsorption of F on the Ni fcc and hcp sites with subsequent H_2 formation is exothermic by a considerable amount. This suggests the formation of fluorinated Ni surfaces is likely to occur, which is consistent with previous findings of fluoride formation of Ni surfaces in contact with anhydrous HF.[11] Also for the adsorption of F, there is a clear preference for the hollow sites, with a slightly lower energy for the adsorption on the fcc site. The lower ΔE_{at} for F adsorption at the fcc site is the reason for the slightly lower energy of the chemisorption with F at the fcc site and H at the hcp site (see Table 2). The distance between adsorbed atom and the surface layer, z_{at}, is fairly correlated with the adsorption energy.

Molecular dynamics calculations

The simulation of a molecular beam experiment is useful for the data sampling of the PES, especially around reactive channels leading to chemisorption. Through AIMD, the dynamical motion of a molecule may be described on the basis of the Born-Oppenheimer approximation. Nuclear motion follows classical mechanics, in a point-for-point quantum-mechanical

Table 3: Adsorption energies and adsorbate-surface distance of single atoms adsorbed at the three local minima of the Ni(111) surface. The adsorption of a single atom from HF involves the formation of half a stoichiometric equivalent of gaseous H_2 or F_2. Calculated with vdW-DF.

Adsorption site	ΔE_{at} [meV]	z_{at} [Å]
Ni+F + $\frac{1}{2}$ H_2		
top	27	1.856
hcp	−233	1.525
fcc	−293	1.504
Ni+H + $\frac{1}{2}$ F_2		
top	2764	1.484
hcp	2282	0.914
fcc	2257	0.911

description of the electronic structure and its affiliated method, e.g. DFT. A total of 300 trajectories are prepared, each with an HF molecule positioned away from the Ni surface, at $z = 8$ Å. The initial angles θ and ϕ as well as the horizontal coordinates u and v are picked at random for all trajectories. The quantum-mechanical vibrational ground state is described quasi-classically: Initial r values are randomly sampled along the bond axis. Vibrational motion is included as classical forces initially acting on H and F, such that the stretch frequency is consistent with the frequency calculated with the DVR basis approach (see Table 1). The quasi-classical approach has been shown to be comparable to a quantum-dynamical treatment of the ro-vibrational levels in an AIMD study on H_2 adsorption on Cu(111), at least for the vibrational ground state.[46] Momentum corresponding to a kinetic energy of 2.0 eV is provided to the HF molecule to ensure that a large number of chemisorption events takes place. The momentum is applied along the normal vector of the Ni surface, corresponding to an idealized molecular beam experiment. With the frozen surface approximation, we neglect kinetic energy transfer from HF to surface phonons. This approximation has been found to slightly increase the chemisorption probability of HCl on Au(111) and CHD_3 on Cu(111).[26,58]

The AIMD trajectories are divided into chemisorbed (labeled C) and scattered (labeled S) cases. Our criterion for a C trajectory is that, at some point, the intramolecular distance of HF $r > 2.4$ Å. After the criterion has been met, the simulation is terminated. Therefore,

we are not sampling the PES at larger r values (i.e. chemisorbed structures) but rather focus on the PES from physisorption to the TS leading to chemisorption. In total, 255 trajectories lead to chemisorption. The criterion for an S trajectory is that $z > 8$ Å. For this to be fulfilled, the HF molecule must be scattered back from the surface without bond breakage and move back towards the vacuum. This is true for the remaining 45 trajectories. The sticking probability, P_{st}, is defined as the fraction of trajectories that result in chemisorption

$$P_{\mathrm{st}} = \frac{\#C}{\#C + \#S} \tag{6}$$

From the results, we calculate a P_{st} of 85 %. With a provided kinetic energy of 2.0 eV and the ZPE taken into consideration, the large P_{st} is reasonable. The calculated barriers with the ZPE included, $E^{\ddagger}_{\mathrm{vib}}$ (see Eq. (3)), are 279 meV (fcc TS) and 271 meV (hcp TS).

In order to discuss structural features of the incoming HF molecule that influence the probability of chemisorption, we use AIMD trajectories of the z coordinate, as depicted in Figure 3 for three different AIMD simulations. Two points are defined which correspond to different events during the simulations. First, at $z = 3$ Å, we consider the HF molecule to exit the physisorption region when approaching the surface. This point is marked as I in Figure 3. The second point, z', is defined when and if there is a change of sign in the derivative

$$\left.\frac{\mathrm{d}z}{\mathrm{d}t}\right|_{z'} > 0 \tag{7}$$

This criterion is met if the center of mass of the HF molecule at some point "rebounds" from the surface. Clearly, this happens for all 45 S trajectories, but also occurs in 103 of the 255 C trajectories. These 103 rebounding chemisorbed trajectories form the subset $C_{\mathrm{R}} \subseteq C$. In total, there are 148 ($\#S + \#C_{\mathrm{R}}$) rebounding trajectories. The remaining 152 trajectories are labeled "directly" chemisorbing, C_{D}, since the HF molecule chemisorbs very efficiently without rebounding (at all times, $\frac{\mathrm{d}z}{\mathrm{d}t} < 0$). Directly chemisorbing trajectories form the subset $C_{\mathrm{D}} \subseteq C$, with $C = \{C_{\mathrm{R}}, C_{\mathrm{D}}\}$. The second point defined by condition (7) is labeled

II. Examples of point II are given for one S and one C_{R} trajectory in Figure 3. Unlike point I, II is defined at different z values for each S and C_{R} trajectory. Point II is picked in this way because it is well defined, and, as we will show next, reveals different structural motifs enhancing chemisorption compared to conditions at point I.

The probability of chemisorption event is somewhat depending on the impact angle θ when HF approaches the surface. Figure 4a shows histograms of the θ and r values of the molecules at point I ($z = 3$Å). The histograms are divided for the C and S trajectories. There is no θ region where scattering is clearly more probable than chemisorption. θ values between 75° and 135° are most common for both C and S trajectories. Within this region, larger angles are more probable to result in scattering. As presented in the r histogram, there is no observable trend in r at point I, but the trajectories rather reflect a distribution caused by the molecular vibration.

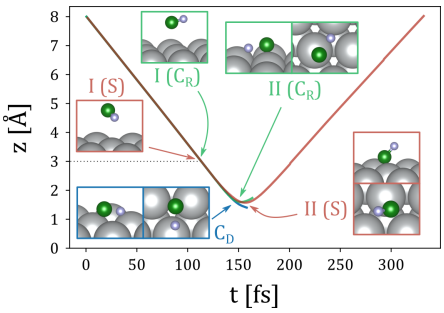

Figure 3: z-value of selected trajectories for a scattered HF molecule (S, red), a directly chemisorbing molecule (C_{D}, blue) and a molecule which chemisorbs after a rebound from the surface (C_{R}, green). Point I corresponds to the first step after which $z < 3$ Å, i.e. when the molecule leaves the physisorption minimum. Point II is defined when $\frac{\mathrm{d}z}{\mathrm{d}t} > 0$, corresponding to the HF center of mass moving away from the surface. II is defined for S and C_{R}, but not for C_{D}. Snapshots of the structures at points I and II are included and colored according to the plotted lines. The C_{D} snapshot is taken at $z = 1.588$ Å. Calculated with vdW-DF and a time step of 0.5 fs.

The increased scattering probability for $\theta \approx 130°$ at point I is somewhat counter-intuitive, as this is close to the calculated TS angle (see Table 2). However, this may be understood as a dynamical effect; if the molecule approaches the surface with the H end downwards

($\theta > 90°$), the small mass of the H atom easily rebounds from the surface before the F atom is within binding distance to the surface. As a consequence, θ drastically decreases at this point. In contrast, if HF approaches the surface with the F atom downwards ($\theta < 90°$), the atom remains close to the surface for a longer time, during which the H atom approaches the surface, which increases the angle and favors chemisorption. The S and C_{R} trajectories in Figure 3 are good examples of this θ dependence at point I, as seen in the structure insets at this point in the figure. The S trajectory has a $\theta = 115.6°$, closer to the TS (127.7° and 128.8°) than the C_{R} trajectory, $\theta = 75.5°$. The increased likelihood for scattering for an incoming molecule with large θ may be understood by studying θ and r at a point II in the simulation.

Figure 4 depicts θ and r histograms at point II for the 148 rebounding S and C_{R} trajectories. From the θ histogram, it is clear that molecules are likely to chemisorb if $\theta > 85°$ since this allows for the chemisorption channels to be accessed. This is also the case for the II (C_{R}) structure in Figure 3, with $\theta = 95.5°$. In contrast, for the scattered case at II (S), $\theta = 42.7°$. For the S trajectory, the larger angle at point I causes the H atom to rebound off the surface, making chemisorption channels inaccessible at point II.

There is also a notable difference in r between S and C_{R} trajectories at point II; S trajectories have a similar r distribution as the "unaffected" distribution at point I (Figure 4a). The C_{R} trajectories may have very large r values well above the TS r (1.382 Å and 1.378 Å, Table 2), but values close to the equilibrium bond length of a free HF molecule (0.937 Å) are less abundant, meaning the H–F bond should be somewhat stretched for a rebounding molecule to not scatter off the surface. Therefore, in the quasi-classical picture, the likelihood of chemisorption is depending on the actual elongation of the HF bond for rebounding trajectories. This is consistent with the late TS, which suggests that vibrational modes, rather than the kinetic energy, are predominantly involved in the reactive channel of the PES. Furthermore, we may conclude that the θ angle is crucial for the binding of HF to Ni(111), which is expected solely due to geometry reasons (for chemisorption, H must not

point away from the surface).

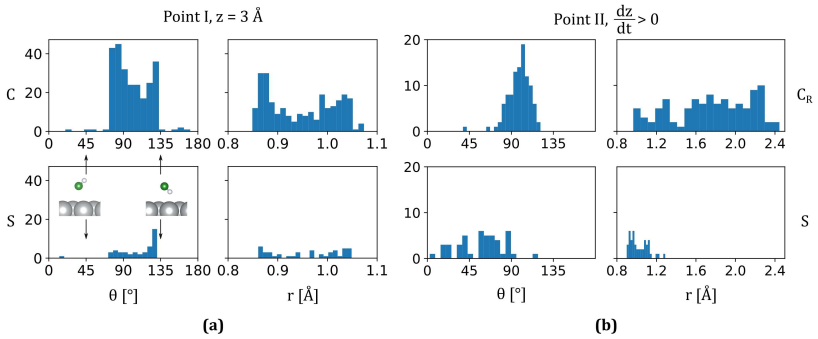

Figure 4: (a) Impact angle θ and H–F distance r when the HF molecules pass the physisorption region (point I, $z = 3$ Å). All 300 trajectories are included and divided into 255 chemisorbed (C) and 45 scattered (S) cases, giving a sticking probability of 85 %. (b) 148 "rebounding" trajectories are selected under the criterion that the HF center of mass at some point increases the distance to the surface ($\frac{dz}{dt} > 0$). The trajectories are divided into 103 chemisorbed (C_R) and 45 scattered (S) cases. θ and r are given at the z value where its derivative turns positive, i.e. point II (on average at $z' = 1.52$ Å). Calculated with vdW-DF.

Figure 5 depicts distributions of u and v at point I, projected on the surface unit cell of Ni(111). All 300 trajectories are included and divided into C and S cases, which are drawn in different color. There is a higher probability for scattering if the HF center of mass (which is strongly shifted towards F) is close to a top site. No S trajectories are found for u and v values around the hcp and fcc sites. Furthermore, a multitude of C trajectories are found at the bridge positions. Jiang et al. found a similar distribution in their DFT study on the chemisorption of H_2O on Ni(111), with chemisorption occuring most frequently at hollow and bridge sites, at similar high incidence kinetic energies.[30] At the top position, the

F atom is further away from the surface, which means a smaller range of θ angles lead to chemisorption. Therefore, trajectories with u and v corresponding to the top position are more likely to exhibit repulsion between HF and Ni.

In Figure 5, we also differentiate between rebounding trajectories $S + C_{\mathrm{R}}$ (solid border), and directly chemisorbing trajectories C_{D} (no border). Direct chemisorption occurs in most regions of the plot, but is more probable at the hollow sites. The rebounding feature is more prominent at the top site, as demonstrated in Figure 3. For the C_{R} and S trajectories, the rebounding point II occurs at $z \approx 1.58$ Å. Also included in Figure 3 is a snapshot of the C_{D} trajectory close to this z value. The C_{D} trajectory shows a molecule with the center of mass over the fcc site, leading to direct chemisorption. In contrast, in the C_{R} trajectory, the molecule rebounds off the more repulsive top site.

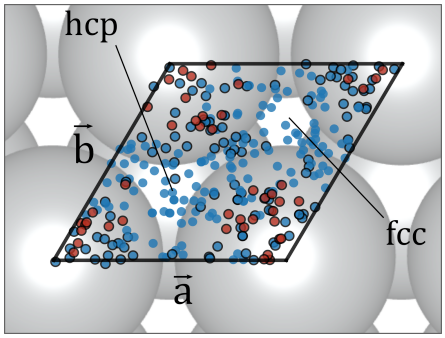

Figure 5: Distribution of u and v values of the AIMD trajectories when the molecules exit the physisorption region (point I, $z = 3$ Å) towards the surface. u and v are scalars of the lattice vectors $\vec{a}$ and $\vec{b}$. The trajectories which lead to chemisorption (C) are colored blue and the ones that lead to scattering (S) are colored red. Trajectories that at some point rebound from the surface ($\frac{\mathrm{d}z}{\mathrm{d}t} < 0$) are depicted with a solid border ($S + C\mathrm{R}$). Calculated with vdW-DF.

In order to fit a NN PES, we make use of the ca. 111000 SCF calculations from the AIMD trajectories. The points are divided into 61000 far ($z > 4$ Å) and 50000 near ($z \leq 4$ Å) points. Of the far points, 10 % are selected for the fit due to the flatter PES in all degrees of freedom except z and r. All near points are used. Due to a shown successful combination of AIMD points with static DFT points as dataset for NN PES fit,[26] we include 9000 single-point DFT

calculations at the four high-symmetry sites and some selected angles $\theta = \{0°, 45°, 90°\}$ and $\phi = \{0°, 30°, 90°\}$ (top, hcp, fcc) or $\{0°, 45°, 90°\}$ (bridge). The remaining degrees of freedom are sampled as non-uniform grids between 0.8-8.0 Å for z and 0.4-2.8 Å for r (the values are listed among the computational details).

The NN follows the structure: one input layer with 10 nodes, three hidden layers with 40 nodes each, one output layer with a single node. For any fit, a reference set is extracted from 10 % of the points, whereas the remaining points make up the training set. Points of lower energy predominantly contain r values close to the equilibrium bond length. By including larger values of r, as necessary for describing the bond breaking, there is a trade-off in that the root mean square error (RMSE) increases. By testing various cutoffs in the degrees of freedom, fits are reasonably accurate until $r = 1.7$ Å, which yields an RMSE of 59 meV. This is slightly above the limit of chemical accuracy (1.0 kcal/mol = 43 meV). In Figure 6, PES plots of the z and r degrees of freedom are compared for three cases of varying site and θ. From the results, it is clear that our NN fit reproduces the curvature of the DFT PES very well. For the molecules parallel to the surface ($\theta = 90°$), the curvature and energy levels fit until $r \approx 1.4$ Å. The TS in the top site PES is differing slightly in the curvature for $r > 1.5$ Å, where the fitted potential overestimates the TS bond length. However, in the hcp site PES, the energy and coordinate of the TS is very similar between fitted and DFT results. In this TS, the F atom is located at the hcp site whereas, at $r = 1.4$ Å, the H atom is located as close as possible to a neighboring top Ni atom. An increase in r means the H atom goes into the next hcp site on the Ni(111) surface ($\theta = 0°$; see Figure 6). The energy of the TS from the fitted PES for the hcp site is 1100 meV relative to the isolated reactants. Compared to our DIMER method TSs ($\theta = 127.7°$ and 128.4°, F slightly off the top site), the main structural difference is the smaller $\theta = 90°$.

We also compare the fitted PES of the case when the molecule is aligned perpendicularly to the surface with $\theta = 0°$ (see Figure 6). As expected, there is no saddle point for these parameters since the H atom points towards the vacuum. Furthermore, in contrast to the

horizontal orientation, the PES along r is relatively unchanged at the minimum around $z = 3.5$ Å, compared to the unbound case at $z = 8.0$ Å. This is consistent with the minor influence by the Ni surface on the HF bond when the F atom is pointing down, due the LUMO pointing away from the surface.

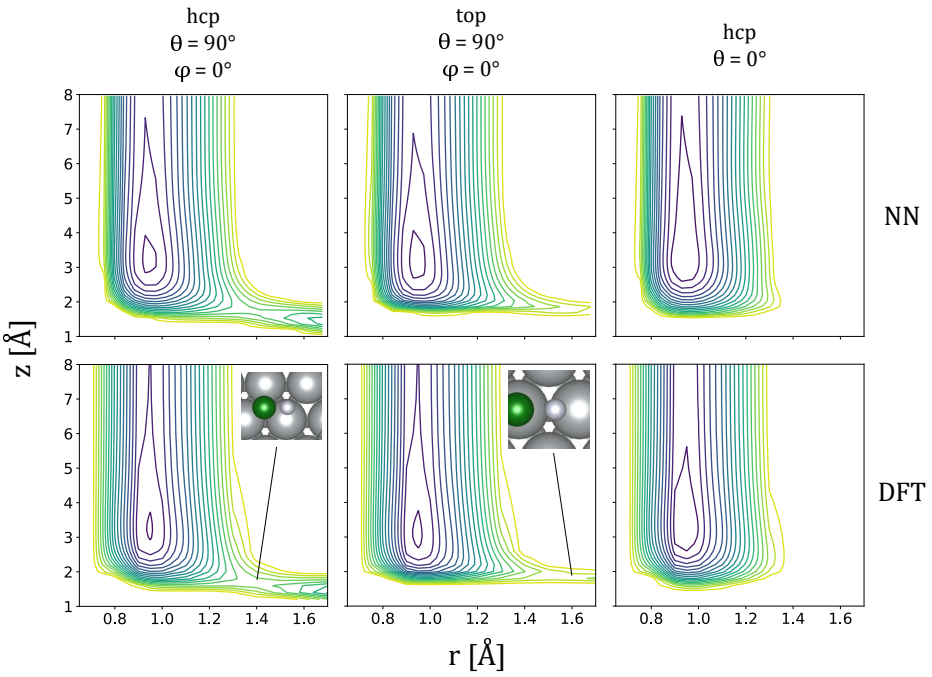

Figure 6: Comparison of r-z potential energy surfaces fitted by the neural network and calculated directy from static DFT calculations with the vdW-DF functional. The contour lines denote a difference of 100 meV. Lines are included up to 2 eV.

We finally evaluate the accuracy of the fitted PES at the u, v, θ and ϕ coordinates of the calculated DIMER TSs (presented in Table 2). Figure 7 shows the r-z PES plots for the two TSs. With θ at 127.7° and 128.4°, the path to chemisorption is energetically lower than for the $\theta = 90°$ discussed above, since this allows the H atom to approach the Ni surface more efficiently. Furthermore, with the F atom placed slightly off from the top site (see Figure 2), the larger θ angles mean that the H atom may point directly towards the hollow site. Because of the stronger binding between H and the Ni atoms, the minimum energy

path towards chemisorption is less steep (cf. Figure 6) with this orientation.

The fitted energy of the fcc TS, 547 meV, differs from the DFT energy by 33 meV which is within chemical accuracy. Moreover, the curvature of the fitted PES is reasonable with the coordinates of DIMER method TS fitting well along the reactive channel. For the hcp TS, the structural parameters are well described by the NN fit. Both plots show a flattening of the minimum energy path, at bond lengths expanding over 1.4 Å, which indicates a bond breaking close to this point. However, for the hcp TS, the minimum energy path in the two-dimensional PES along increasing r is somewhat steeper than for the fcc TS. The fitted PES energy of the hcp TS is 617 meV, an overestimation by 111 meV. This means the NN-fitted potential predicts an energetically lower path towards chemisorption over the fcc TS. This is in contrast to the DFT calculations, which puts the TSs in the same energy range. A higher number of data points of HF molecules for the NN would likely improve the fitted potential and give a quantitative description of the energy of the hcp TS. We therefore consider these PESs qualitatively or semi-quantitatively correct.

Finally, the rebounding point II for S and C_{R} trajectories discussed above may be understood from the presented PES plots. The calculated average z value of the turning point for the trajectories is 1.52±0.08 Å. All contour plots in Figs. 6 and 7 include energies until 2.0 eV (yellow contour lines) The kinetic energy applied to the incoming molecule is also 2.0 eV. Hence, the included contour lines represent the limits of each PES which are theoretically accessible with the provided kinetic energy. In all presented PES plots, a 2.0 eV contour line is positioned roughly along $z \approx 1.5$ Å for r values close to the equilibirum bond length, which fits the average z value at point II well. In this view, the initial vibrational ZPE of 235 meV is neglected since the vibrational energy enhances motion along the r coordinate.

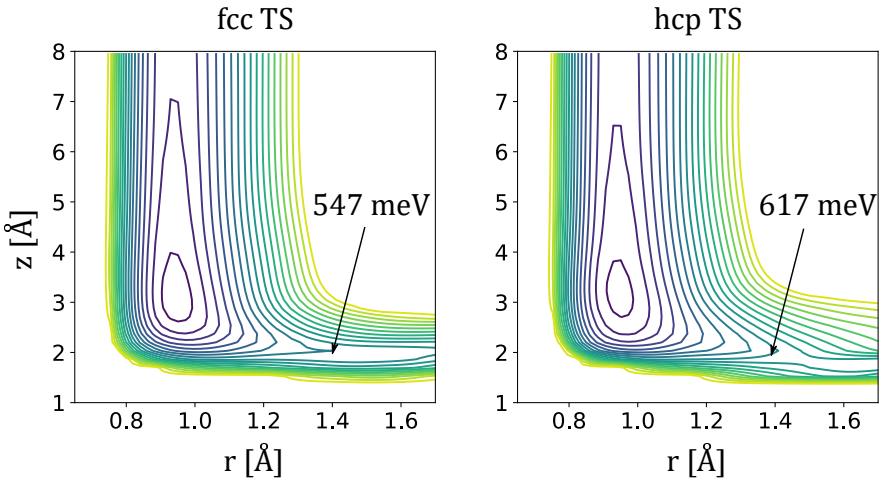

Figure 7: r-z potential energy surfaces fitted by the neural network. The remaining coordinates correspond to the fcc and hcp transition states calculated with the DIMER method. Arrows denote the parameters of the TSs calculated with the DIMER method, whereas the energies refer to the plotted NN PES. The contour lines denote a difference of 100 meV. Lines are included up to 2 eV.

Conclusions

By studying both minimum path reaction steps and the dynamical adsorption simulations we have investigated the activation of HF and its chemisorption on a Ni(111) surface. We find that the chemisorption of a single molecule is an exothermic process with a moderate binding energy. Moreover, the adsorption of an F atom on Ni from HF, with gaseous H_2 as a byproduct, is found to be exothermic relative to the isolated Ni(111) surface and gaseous HF. This is in line with previous findings of spontaneous fluorination of Ni in contact with an atmosphere of HF.[11]

Furthermore, the calculated TS energies are 279 meV and 271 meV relative to the isolated species, with vibrational ZPE taken into consideration. For a molecule trapped in the physisorption minimum, the barriers are increased to 460 meV and 452 meV. The calculated barriers are lower than previously calculated TS energies of the first dissociation in the activation of methane and water on Ni(111).[30,31] Two transition states of similar structure are

found, with the HF molecule situated over an fcc or hcp site, with the F atom positioned slightly off from a top Ni atom.

Trajectories from the dynamical scattering of HF with a kinetic energy of 2.0 eV show a large number of chemisorbed molecules (sticking probability 85%). Analysis of the trajectories shows that the impact angle θ when a molecule first approaches the surface (labeled point I) has an influence on the probability of chemisorption. A large θ (H down) for an incoming molecule is more probable to lead to scattered molecules since the lighter H atom rebounds off the surface before the F atom reaches the surface. Analysis of the trajectories indicates that chemisorption at the u and v coordinates of the calculated DIMER transition states are actually less likely than for molecules where the F atom approaches the surface closer to the hollow sites. With the F atom approaching the top position, it experiences a steeper repulsion, and is more likely to rebound from the surface upon impact (labeled point II). If this rebounding motion occurs, the molecule may still chemisorb to the surface for certain ranges of θ and r at point II.

Our data points were fed into a NN to fit a six-dimensional PES of HF on Ni(111) within the frozen surface approximation. The PES is qualitatively sound and reproduce the static TSs structurally well with errors in the energy of 33 meV and 111 meV, of which the latter falls short of chemical accuracy. For using the NN PES for classical MD simulations the fit has to be improved with more data points, but this first approach shows that we reach semi-quantitative agreement even with a limited amount of data points. Therefore we are optimistic that we can describe liquid HF on the Ni surface in the future, with an improved NN PES for the chemisorption, together with accurate force fields for the liquid HF interaction.

Acknowledgement

We gratefully acknowledge funding from the German Research Foundation (DFG) as part of the project SFB 1349: "Fluorine-Specific Interactions" (Gefördert durch die Deutsche Forschungsgemeinschaft (DFG), Projektnummer 387284271, SFB 1349). We also express our gratitude towards the Network of High Performance Computers in Northern Germany (HLRN) for the research grant providing computational resources through the research project bec00154. We thank the Central Computing Services of the Freie Universität Berlin (ZEDAT) for providing file systems and technical maintenance of our computers. We are grateful to Dr. Gernot Füchsel for theoretical and practical guidance in the dynamical calculations and neural network fitting procedures. We thank Hannah Eyre for careful proofreading of the manuscript.

References

(1) Simons, J. H. Production of Fluorocarbons: I. The Generalized Procedure and its Use with Nitrogen Compounds. *J. Electrochem. Soc.* **1949**, *95*, 47–52.

(2) Abe, T. The electrochemical fluorination as a locomotive for the development of fluorine chemistry. *J. Fluorine Chem.* **2000**, *105*, 181–183.

(3) Ignat'ev, N. V. In *Modern Synthesis Processes and Reactivity of Fluorinated Compounds*; Groult, H., Leroux, F., Tressaud, A., Eds.; Elsevier: London, 2017; pp 71–123.

(4) Ignatiev, N. V.; Welz-Biermann, U.; Heider, U.; Kucheryna, A.; von Ahsen, S.; Habel, W.; Sartori, P.; Willner, H. Carbon-chain isomerization during the electrochemical fluorination in anhydrous hydrogen fluoride–a mechanistic study. *J. Fluorine Chem.* **2003**, *124*, 21–37.

(5) Chang, B.; Yanase, H.; Nakanishi, K.; Watanabe, N. The electrochemical fluorination of n-propyl-, diethyl- and triethylamine. *Electrochim. Acta* **1971**, *16*, 1179–1196.

(6) Watanabe, N. Electrochemical application of fluorine chemistry. *J. Fluorine Chem.* **1983**, *22*, 205–230.

(7) Drakesmith, F. G.; Hughes, D. A. Electrochemical fluorination using porous nickel and foam nickel anodes. *J. Fluorine Chem.* **1986**, *32*, 103–134.

(8) Dimitrov, A.; Rüdiger, S.; Ignatiev, N. V.; Datsenko, S. Investigations on the electrochemical fluorination of amines. *J. Fluorine Chem.* **1990**, *50*, 197–205.

(9) Mattsson, S.; Paulus, B. A theoretical study on the binding and electrolytic splitting of hydrogen fluoride on Ni(111) and Ni(211). *Phys. Chem. Chem. Phys.* **2020**, *22*, 4407–4415.

(10) Lide, D. R., Ed. *Standard Thermodynamic Properties of Chemical Substances in CRC Handbook of Chemistry and Physics, Internet Version*; CRC Press: Boca Raton, FL, 2005.

(11) Totir, G. G.; Chottiner, G. S.; Gross, C. L.; Childs, W. V.; Scherson, D. A. X-Ray Photoelectron Spectroscopy and Morphological Studies of Polycrystalline Nickel Surfaces Exposed to Anhydrous HF. *J. Electrochem. Soc.* **2000**, *147*, 4212–216.

(12) Izvekov, S.; Voth, G. A. Effective Force Field for Liquid Hydrogen Fluoride from Ab Initio Molecular Dynamics Simulation Using the Force-Matching Method. *J. Phys. Chem. B* **2005**, *109*, 6573–6586.

(13) Mazack, M. J. M.; Gao, J. Quantum mechanical force field for hydrogen fluoride with explicit electronic polarization. *J. Chem. Phys.* **2014**, *140*, 204501.

(14) Liang, T.; Shin, Y. K.; Cheng, Y.-T.; Yilmaz, D. E.; Vishnu, K. G.; Verners, O.; Zou, C.; Phillpot, S. R.; Sinnott, S. B.; van Duin, A. C. T. Reactive Potentials for Advanced Atomistic Simulations. *Annu. Rev. Mater. Res.* **2013**, *43*, 109–129.

(15) van Duin, A. C. T.; Dasgupta, S.; Lorant, F.; Goddard III, W. A. ReaxFF: a reactive force field for hydrocarbons. *J. Phys. Chem. A* **2001**, *105*, 9396–9409.

(16) van Duin, A. C. T.; Strachan, J.; Stewman, S.; Zhang, Q.; Xu, X.; Goddard III, W. A. $ReaxFF_{SiO}$ Reactive Force Field for Silicon and Silicon Oxide Systems. *J. Phys. Chem. A* **2003**, *107*, 3803–3811.

(17) Liu, B.; Lusk, M. T.; Ely, J. F.; van Duin, A. C. T.; Goddard III, W. A. Reactive molecular dynamics force field for the dissociation of light hydrocarbons on Ni(111). *Mol. Simulat.* **2008**, *34*, 967–972.

(18) Behler, J. First Principles Neural Network Potentials for Reactive Simulations of Large Molecular and Condensed Systems. *Angew. Chem. Int. Ed.* **2017**, *56*, 12828–12840.

(19) Manzhos, S.; Dawes, R.; Carrington, T. Neural network-based approaches for building high dimensional and quantum dynamics-friendly potential energy surfaces. *Int. J. Quantum Chem.* **2015**, *115*, 1012–1020.

(20) Henkelman, G.; Jóhanesson, G.; Jónsson, H. In *Theoretical Methods in Condensed Phase Chemistry: Progress in Theoretical Chemistry and Physics*; Schwartz, S. D., Ed.; Springer: Dordrecht, Netherlands, 2002; pp 269–302.

(21) Henkelman, G.; Arnaldsson, A.; Jónsson, H. Theoretical calculations of CH_4 and H_2 associative desorption from Ni(111): Could subsurface hydrogen play an important role? *J. Chem. Phys.* **2006**, *124*, 044706.

(22) González, S.; Sousa, C.; Illas, F. Promoter and poisoning effects on NO-catalyzed dissociation on bimetallic RhCu(111) surfaces. *J. Catal.* **2006**, *239*, 431–440.

(23) Mei, D.; Xu, L.; Henkelman, G. Dimer saddle point searches to determine the reactivity of formate on Cu(111). *J. Catal.* **2008**, *258*, 44–51.

(24) Mei, D.; Xu, L.; Henkelman, G. Potential Energy Surface of Methanol Decomposition on Cu(110). *J. Phys. Chem. C* **2009**, *113*, 4522–4537.

(25) Gajewski, G.; Pao, C.-W. Ab initio calculations of the reaction pathways for methane decomposition over the Cu (111) surface. *J. Chem. Phys.* **2011**, *135*, 064707.

(26) Füchsel, G.; del Cueto, M.; Díaz, C.; Kroes, G. J. Enigmatic HCl + Au(111) Reaction: A Puzzle for Theory and Experiment. *J. Phys. Chem. C* **2016**, *120*, 25760–25779.

(27) Tchakoua, T.; Smeets, E. W. F.; Somers, M. F.; Kroes, G. J. Toward a Specific Reaction Parameter Density Functional for H_2 + Ni(111): Comparison of Theory with Molecular Beam Sticking Experiments. **2019**, *123*, 20420–20433.

(28) Nour Ghassemi, E.; Smeets, E. W. F.; Somers, M. F.; Kroes, G. J.; Groot, I. M. N.; Juurlink, L. F.; Füchsel, G. Transferability of the Specific Reaction Parameter Density Functional for H_2 + Pt(111) to H_2 + Pt(211). *J. Phys. Chem. C* **2019**, *123*, 2973–2986.

(29) Füchsel, G.; Zhou, X.; Jiang, B.; Juaristi, J. I.; Alducin, M.; Guo, H.; Kroes, G. J. Reactive and Nonreactive Scattering of HCl from Au(111): An Ab Initio Molecular Dynamics Study. *J. Phys. Chem. C* **2019**, *123*, 2287–2299.

(30) Jiang, B.; Guo, H. Dynamics of Water Dissociative Chemisorption on Ni(111): Effects of Impact Sites and Incident Angles. *Phys. Rev. Lett.* **2015**, *114*, 166101.

(31) Li, K.; Jiao, M.; Wang, Y.; Wu, Z. CH_4 dissociation on NiM(111) (M = Co, Rh, Ir) surface: A first-principles study. *Surf. Sci.* **2013**, *617*, 149–155.

(32) Nattino, F.; Migliorini, D.; Kroes, G. J.; Dombrowski, E.; High, E. A.; Killelea, D. R.; Utz, A. L. Chemically Accurate Simulation of a Polyatomic Molecule-Metal Surface Reaction. *J. Phys. Chem. Lett.* **2016**, *7*, 2402–2406.

(33) Kresse, G.; Furthmüller, J. Efficiency of ab-initio total energy calculations for metals and semiconductors using a plane-wave basis set. *Comput. Mater. Sci.* **1996**, *6*, 15–50.

(34) Kresse, G.; Furthmüller, J. Efficient iterative schemes for ab initio total-energy calculations using a plane-wave basis set. *Phys. Rev. B* **1996**, *54*, 11169–11186.

(35) Blöchl, P. E. Projector augmented-wave method. *Phys. Rev. B* **1994**, *50*, 17953–17979.

(36) Perdew, J. P.; Burke, K.; Ernzerhof, M. Generalized Gradient Approximation Made Simple. *Phys. Rev. Lett.* **1996**, *77*, 3865–3868.

(37) Zhang, Y.; Yang, W. Comment on "Generalized Gradient Approximation Made Simple". *Phys. Rev. Lett.* **1998**, *80*, 890.

(38) Dion, M.; Rydberg, H.; Schröder, E.; Langreth, D. C.; Lundqvist, B. I. Van der Waals Density Functional for General Geometries. *Phys. Rev. Lett.* **2004**, *92*, 246401.

(39) Lee, K.; Murray, E. D.; Kong, L.; Lundqvist, B. I.; Langreth, D. C. Higher-accuracy van der Waals density functional. *Phys. Rev. B* **2010**, *82*, 081101.

(40) Grimme, S.; Antony, J.; Ehrlich, S.; Krieg, S. A consistent and accurate ab initio parametrization of density functional dispersion correction (DFT-D) for the 94 elements H-Pu. *J. Chem. Phys.* **2010**, *132*, 154104–154119.

(41) Grimme, S.; Ehrlich, S.; Goerigk, L. Effect of the damping function in dispersion corrected density functional theory. *J. Comput. Chem.* **2011**, *32*, 1456–1465.

(42) Wyckoff, R. W. G. *Crystal Structures*; Wiley-Interscience: New York, 1963.

(43) Henkelman, G.; Jónsson, H. A. A dimer method for finding saddle points on high dimensional potential surfaces using only first derivatives. *J. Chem. Phys.* **1999**, *111*, 7010.

(44) Heyden, A.; Bell, A. T.; Keil, F. J. Efficient methods for finding transition states in chemical reactions: Comparison of improved dimer method and partitioned rational function optimization method. *J. Chem. Phys.* **2005**, *123*, 224101.

(45) Kästner, J.; Sherwood, P. Superlinearly converging dimer method for transition state search. *J. Chem. Phys.* **2008**, *128*, 014106.

(46) Díaz, C.; Olsen, R. A.; Auerbach, D. J.; Kroes, G. J. Six-dimensional dynamics study of reactive and non reactive scattering of H_2 from Cu(111) using a chemically accurate potential energy surface. *Phys. Chem. Chem. Phys.* **2010**, *12*, 6499–6519.

(47) Henkelman, G.; Arnaldsson, A.; Jónsson, H. A fast and robust algorithm for Bader decomposition of charge density. *Comput. Mat. Sci.* **2006**, *36*, 354–360.

(48) Momma, K.; Izumi, F. VESTA 3 for three-dimensional visualization of crystal, volumetric and morphology data. *J. Appl. Crystallogr.* **2011**, *44*, 1272–1276.

(49) Bačić, Z.; Light, J. C. Highly excited vibrational levels of "floppy" triatomic molecules: A discrete variable representation – Distributed Gaussian basis approach. *J. Chem. Phys.* **1986**, *85*, 4594–4604.

(50) Latajka, Z.; Bouteiller, Y. Application of density functional methods for the study of hydrogen-bonded systems: The hydrogen fluoride dimer. *J. Chem. Phys.* **1994**, *101*, 9793–9799.

(51) Klimeš, J.; Bowler, D. R.; Michaelides, A. Chemical accuracy for the van der Waals density functional. *J. Phys.: Condens. Matter* **2010**, *22*, 022201.

(52) Forster-Tonigold, K.; Groß, A. Dispersive interactions in water bilayers at metallic surfaces: A comparison of the PBE and RPBE functional including semiempirical dispersion corrections. *J. Comput. Chem.* **2012**, *33*, 695–701.

(53) Mann, D. E.; Thrush, B. A.; Lide, D. R.; Ball, J. J.; Acquista, N. Spectroscopy of Fluorine Flames. I. Hydrogen-Fluorine Flame and the Vibration-Rotation Emission Spectrum of HF. *J. Chem. Phys.* **1961**, *34*, 420–431.

(54) King, R. B.; Crabtree, C. M.; Lukehart, C. M.; Atwood, D. A.; Scott, R. A. *Encyclopedia of Inorganic Chemistry*; John Wiley & Sons, Ltd., 2006.

(55) Kay, B. D.; Lykke, K. R.; Creighton, J. R.; Ward, S. J. The influence of adsorbate-absorbate hydrogen bonding in molecular chemisorption: NH_3, HF, and H_2O on Au(111). *J. Chem. Phys.* **1989**, *91*, 5120–5121.

(56) Wagner, F. T.; Moylan, T. E. Identification of surface hydronium: Coadsorption of hydrogen fluoride and water on platinum (111). *Surf. Sci.* **1987**, *182*, 125–149.

(57) Kurten, T.; Biczysko, M.; Rajamäki, T.; Laasonen, K.; Halonen, L. Computational Study of the Adsorption Energetics and Vibrational Wavenumbers of NH_3 Adsorbed on the Ni(111) Surface. *J. Phys. Chem. B* **2005**, *109*, 8954–8960.

(58) Gerrits, N.; Shakouri, K.; Behler, J.; Kroes, G. J. Accurate Probabilities for Highly Activated Reaction of Polyatomic Molecules on Surfaces Using a High-Dimensional Neural Network Potential: CHD_3 + Cu(111). *J. Phys. Chem. Lett.* **2019**, *10*, 1763–1768.

Chapter 4

Summary

In this chapter, I will discuss the results of this work in the order of the included papers. Throughout, I will put the findings in the papers in the greater context of the Simons process and mechanistic considerations related to it. The focus has been on the structure and electrochemical formation of Ni_xF_y, as these features are key to a future understanding of the fluorination of any organic molecules. The overall approach to the problem, by using known compounds as a starting point for Ni_xF_y models, has been shown to provide theoretical explanations of several observed phenomena, such as onset potentials and anodic passivation in Simons cells. Furthermore, because the models are rooted in well-known compounds, the results could also be relevant for wider scientific communities concerned with *e.g.* electrochemistry in non-aqueous electrolytes or magnetic materials.

The growing consensus is that the Ni_xF_y film contains nickel centers of oxidation state +III or higher. NiF_2 is stable and not known to undergo any fluorination reactions with organic molecules on its own. The best candidate for a structurally known and reactive crystalline nickel fluoride is NiF_3. Žemva *et al.* have shown that the compound undergoes fluorination with perfluoropropene and even fluorinates Xe to XeF_4.[35] However, due to insufficient crystallinity, its crystal structure could not be completely determined, but, based on their diffractogram, the authors suggested a rhombohedral structure analogous to CoF_3.[196] Furthermore, discrepancies exist regarding the oxidation states of Ni in NiF_3, where a mixed valence of Ni^{2+} and Ni^{4+} is a possibility, other than the Ni^{3+} configuration, as was indicated by X-ray absorption spectroscopy measurements by Hector *et al.*[197] In **Paper A**, we perform calculations with the HSE06 hybrid functional on the series of magnetic 3d metal trifluorides MF_3, from M = Ti to M = Ni. This is done to understand the properties of NiF_3 in the context of the better characterized transition metal trifluorides. In a test of the predicative abilities of our methods, trends in band gap and magnetic

structure are reproduced for these trifluorides, M = Ti − Co.

The calculated electronic properties of NiF_3 are similar to FeF_3 and CoF_3. For NiF_3, we find an electronic structure without mixed valence character. Structural distortions from the $R\bar{3}c$ space group (which does not allow for mixed valence) to the lower-symmetry $R\bar{3}$ (which allows for mixed valence, like in PtF_3)[198] or $C2/c$ (which allows for Jahn-Teller distortion, like in MnF_3)[199] leads to relaxation to an FeF_3-like trivalent structure, using the PBE+U functional. Note that the calculated trivalent ground state should be viewed as the ground state with the applied DFT methods and their limitations, and the purpose is not to strictly dismiss a mixed valence phase. One possibility is an increase in mixed valence character in the solid at elevated temperatures. The aforementioned X-ray absorption spectroscopy experiment was performed at room temperature,[197] whereas the DFT calculations are done at 0 K.

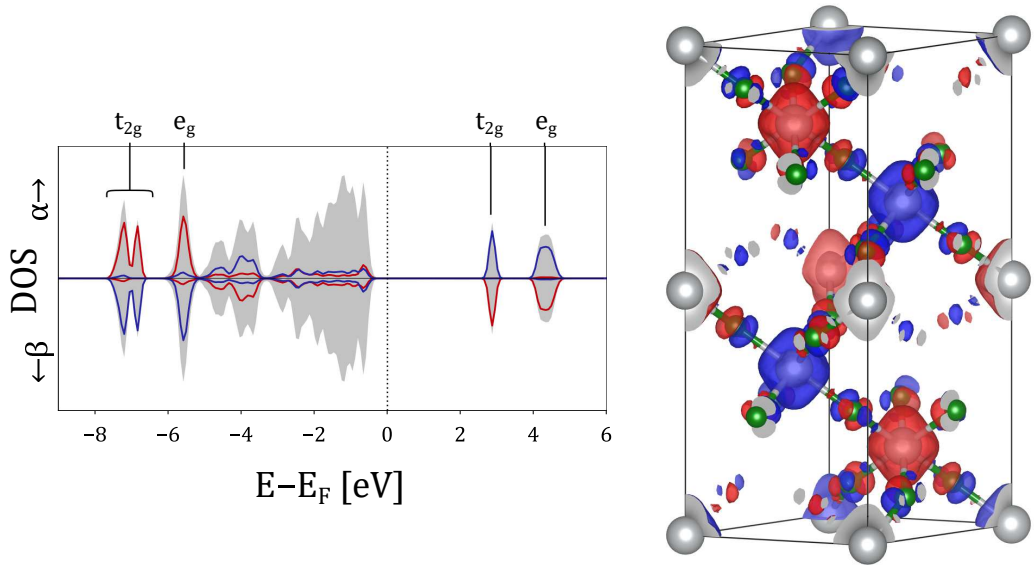

Figure 4.1: Left: Spin-polarized density of states plot of the antiferromagnetic phase of NiF_3. α and β states are plotted upwards and downwards, respectively. The gray filled area refers to the total density of states. Red and blue lines refer to Ni^{3+} centers of α and β majority spin. Right: Isosurface of the magnetization density, $\rho_\alpha - \rho_\beta$, (isovalue 0.005 Å^3) where the colors match the spins in the plot. Each Ni^{3+} center couples antiferromagnetically with six neighbors. Calculated with HSE06.

Fig. 4.1 depicts the DOS for NiF_3, calculated with the HSE06 functional. The electronic band gap is 3.28 eV and has a charge-transfer character, with the valence bands localized on the fluoride ions and the conduction bands on nickel. Like for FeF_3 and CoF_3, the ground state configuration of the d electrons is of the high-spin type. There is considerable hybridization between nickel e_g orbitals and fluoride 2p

orbitals, which decreases the local spin magnetic moment at Ni centers to 2.3 μ_B and indicates some covalent character in the Ni–F bonds. This hybridization is visible in the e_g peak around –5.6 eV in DOS plot. The Ni^{3+}–F^- bond length is 1.88 Å from the structures optimized with the PBE+U functional.

An antiferromagnetic ground state is found with a Néel temperature of 853 K using a collinear Heisenberg model for the spin coupling constants and a mean field theory treatment of the spin coupling. Note that these models typically overestimate critical temperatures, not seldom by as much as twice the experimental value (see Section 2.4). Nevertheless, this is an indication of strong magnetic coupling, which is predicted by the Goodenough-Kanamori rules for superexchange coupling.[150] The calculated Heisenberg model coupling constants J (see eq. (2.63)) are –9.8 meV using the HSE06 functional. This amounts to non-negligible energies differences between magnetic phases, especially for centers with higher coordination numbers and more couplings, and stresses the need for a careful assessment of spin configurations of Ni^{3+} ions in any further Ni_xF_y models.

The superexchange coupling may be understood by studying the magnetization density, *i.e.* the difference between spin densities, $\rho_\alpha - \rho_\beta$. An iso-surface of the magnetization density is plotted in Fig. 4.1. As expected, most of the magnetization density is localized on the Ni^{3+} centers (gray spheres). However, according to the superexchange coupling mechanism, the antiparallelly coupling metal centers on both sides of an F^- ion induce a magnetic multipole moment at the diamagnetic F^- ion, which enables the relatively strong AFM coupling.[150] For the ideal case of a 180° Ni–F–Ni angle, this would means a simple magnetic dipole moment is induced in the direction of the bonds. In the NiF_3 structure, the angle is smaller (146°), meaning the induced magnetic moment has a more complex shape, which is reflected in the magnetization density at the F^- ions (green spheres). Note that the *total* magnetization of an F^- ion is zero.

With a better understanding of the bulk properties of NiF_3, I will now shift the focus towards various surface systems, in order to acquire a better understanding of the Ni_xF_y film. Cyclovoltammetry experiments on Simons cells have shown some inconsistencies, where adsorbates on the metallic Ni surface may play a role in the passivation of the anode at low and intermediate potentials.[18,22–24] Dimitrov *et al.* reported that extensively cleaned Ni anodes show anodic current at cell potentials as low as 0.1 V.[18] On the other hand, if the anode has been previously used, the peak is absent. One possible explanation for these findings is a facile oxidation of the metallic Ni surface occurring already at low potentials during the polarization of the cell. A likely end product is a passivating NiF_2 film which covers the Ni surface. This is consistent with the sum reaction

$$Ni + 2HF \rightarrow NiF_2 + H_2 \tag{4.1}$$

having a change in standard Gibbs free energy of –552 meV, revealing an exergonic process, at least for the bulk compounds.[200]

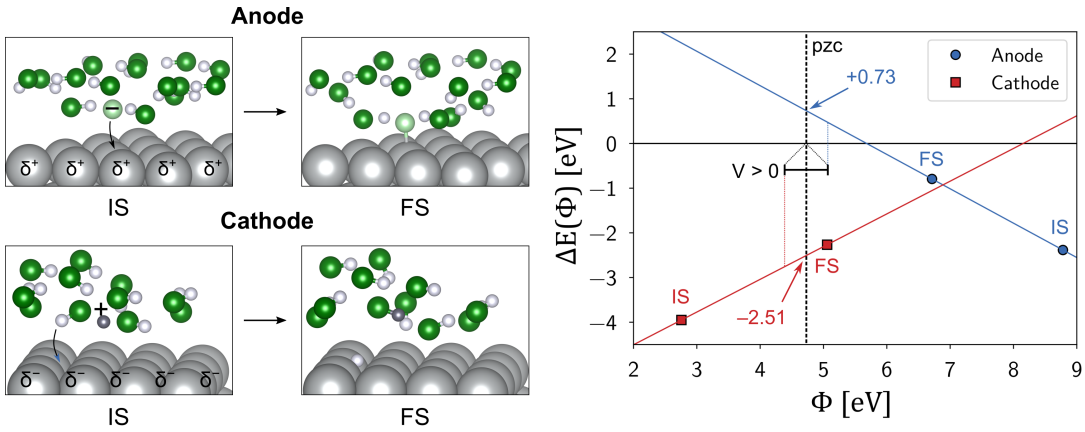

Figure 4.2: Left: Structures of anode and cathode interfaces. The adsorption starts with an initial state (IS) and ends in a final state (FS). For the anode, the solvated F^- is highlighted in light green, and for the cathode, the solvated H^+ is highlighted in black. Right: Half-cell reaction energies from the reaction depicted on the left. The point of zero charge (pzc) is the calculated electrode potential without an external voltage ($V = 0$). Calculated with PBE-D3(BJ).

DFT models for atomistic-scale electrode interfaces have been developed in recent years, based on various H_2O/metal systems.[181,189,190,192,193,201–203] However, no studies have been reported with HF as the electrolyte. **Paper B** considers the electrolytic splitting of HF as adsorptions of H^+ and F^- ions on Ni cathodes and anodes, respectively. Both reactions are modeled at the atomistic scale using the PBE functional with D3(BJ) dispersion correction, and interfaces are constructed to resemble the electric double layer structure at electrodes. Structures used at depicted in Fig. 4.2 Solvent effects are considered explicitly, by including a layer of HF over a Ni(111) surface, where the H^+ and F^- ions are solvated by the HF molecules. Through the capacitor model described in Section 2.6.2, potential-dependent reaction energies of both half-cell reactions are calculated. Already in the absence of a cell potential, the half-cell adsorption energies are –2.51 eV (cathode) and +0.73 eV (anode), as presented in Fig. 4.2. By summing the half-cell reaction energies, we find an exothermic total reaction with a reaction energy of –1.78 eV. This means that the facile initial fluorination at even minimal cell polarization is plausible. Interestingly, the results suggest that, at this point, the reaction is energetically driven by the cathode reaction.

As already discussed, anodic current at low potentials most likely results in the formation of a NiF_2 film. From the absence of current in the CV experiments at inter-

mediate cell potentials (0.5-3 V), the NiF_2 film likely passivizes the anode, preventing further corrosion of the Ni material. Hackerman *et al.* employed cyclovoltammetry techniques to study the potential-dependent corrosion in anhydrous HF of various transition and main-group metals as anode material, and found that resistance to corrosion was a distinct property of Ni in this system.[204] Several other metals (*e.g.* Fe, Co and Cu) also resisted corrosion but did not feature any anodic peaks at higher potentials, characteristic for Ni anodes, in the measured potential window until 10 V *vs.* a Hg/Hg_2F_2 reference electrode.

In **Paper C**, we aim to characterize the anodic peak with an onset at cell potentials around 3 V, as observed in Simons cells.[8,18,22–24] The assumption is made that, until the onset of current, the Ni anode is covered with NiF_2. We approximate the surface structure of the film as crystalline surfaces of NiF_2 and calculate the surface energies (see Section 2.5) of the five low-index surfaces using the HSE06 functional. The PBE+U functional is used for structure optimizations. The (110), (100) and (101) surfaces form a set of more stable surfaces (0.62-0.73 J/m^2) whereas the (001) and (111) surfaces are significantly higher in energy (0.95-1.13 J/m^2, depending on termination). Huesges *et al.* and Kaawar *et al.* performed hybrid functional calculations on the low-index surfaces of the structurally analogous rutile crystals MgF_2 and ZnF_2, respectively, and found same orderings in surface energy, also characterizing the (110), (100) and (101) surfaces as lower in energy.[205,206] The surface energy calculations of NiF_2 require the energy of the bulk crystal (see eq. (2.68)). Therefore, in the paper, we also include the calculated band gap of 5.9 eV of bulk NiF_2 at the HSE06 level. This is in good agreement with the experimental electronic band gap of about 5 eV.[207]

From the five surfaces in hand, Ni_xF_y models are constructed with the addition or removal of F^- at the uppermost surface layers, corresponding to oxidation or reduction of surface Ni^{2+} ions. From stoichiometric fluorine coverages of the NiF_2 surface, addition (removal) of surface fluorine atoms yield Ni^{3+} (Ni^+) centers. In Fig. 4.3, structures of the (110) and (100) surfaces are depicted. Stoichiometric fluorine coverages are included as well as the higher coverage yielding coordinatively saturated Ni^{3+} centers. The newly formed Ni–F bond length is 1.74 Å for (110) and 1.73 Å for (100), smaller than the calculated 1.88 Å for bulk NiF_3, which is attributed to the exposed terminal F^- ion. From Bader analysis, the oxidized Ni centers have localized spin magnetic moments 2.2 μ_B. Similar to bulk NiF_3, there is a significant localization of magnetization density on the terminal F^- ions: 0.5 μ_B and 0.4 μ_B for (110) and (100). Addition of the magnetic moments give values close to the formal oxidation state of high-spin Ni^{3+}, +III.

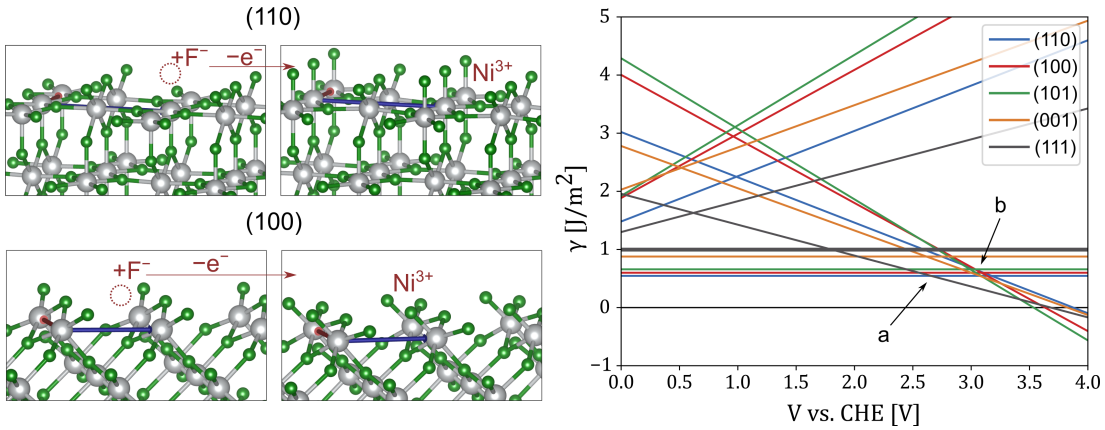

Figure 4.3: Left: Structures of the NiF_2 (110) and (100) surfaces with stoichiometric (Ni^{2+}) and higher fluorine coverages (Ni^{3+}). For the stoichiometric surfaces, the adsorption site of F^- is marked with a red circle. For the oxidized surfaces, the formed Ni^{3+} site is marked. Right: Potential-dependent surface energies calculated according to eq. (2.68) for all NiF_2 surfaces. The surface oxidation state is given by the slope of the curve. Ni^+: $\gamma' > 0$, Ni^{2+}: $\gamma' = 0$, Ni^{3+}: $\gamma' < 0$. The label a marks the point where the oxidized (111) surface becomes the most stable one. Label b marks where *all* oxidized surfaces become more stable than any stoichiometric ones. Calculated with the HSE06 functional using structures optimized with the PBE+U functional.

Using *ab initio* thermodynamics[164,165,208] for surface coverages and the computational hydrogen electrode method[177,180] for the electrochemical potentials of F^- adsorbates, potential-dependent surface energies γ may be calculated for surfaces with different fluorine coverages (*i.e.* different surface Ni oxidation states). The methodology is described in Sections 2.5 and 2.6.1. The potential-dependent surface energies of the five investigated surfaces are plotted in Fig. 4.3. Stoichiometric surfaces only include Ni^{2+} centers, why γ is independent of the potential. Non-stoichiometric surfaces are characterized by their slope, $\gamma' = \mathrm{d}\gamma/\mathrm{d}V$, where oxidized surfaces are stabilized by the anodic potential ($\gamma' < 0$). As expected, reduced Ni^+ surfaces ($\gamma' > 0$) are never more stable than stoichiometric ones. At $V = 0$ V vs. CHE, the stoichiometric surfaces (110), (100) and (101) are predicted to dominate. By studying crossing points of γ for oxidized surfaces at higher V, the model proposes necessary potentials needed to thermodynamically stabilize surface Ni^{3+} centers over Ni^{2+}. At 2.7 V, the oxidized (111) surface becomes the most stable. However, this surface is less likely to be formed, since the parent stoichiometric (111) surface is improbable in the NiF_2 film, due to its high surface energy (see above). The onset potential for the oxidation of Ni^{2+} is found to be around 3.1 V, since, at this point, all oxidized surfaces become more stable than the stoichiometric ones. At potentials above 3.5 V, γ turns negative for all oxidized surfaces. Although the model is inappropriate for an explicit

description of structural changes to the film, the negative surface energy indicates that an increase in surface area is likely, which may be interpreted as a break-up of the underlying NiF_2 crystal to enable further fluorination.

Finally, **Paper D** considers the fluorination of metallic Ni by HF, but in a non-electrochemical mechanism, since this could be a further path towards the passivation of Ni. The purpose of the study is two-fold: The first point of interest is the mechanism of the HF adsorption itself, including *e.g.* activation barriers. The second point is the evaluation of a potential energy surface fitting procedure for an HF/Ni surface system, which could be used in future molecular dynamics simulations. I have already mentioned the exergonic standard Gibbs free energy for the formation of NiF_2 from Ni and HF.[200] Furthermore, Totir *et al.* have reported that Ni surfaces in contact with HF are spontaneously fluorinated, leading to a nickel fluoride film which was proposed to be NiF_2.[209] Exposure to gaseous HF lead to thicker films, but also liquid anhydrous HF was found to fluorinate Ni, forming very thin nickel fluoride films. A crucial step for the understanding is the initial adsorption of an HF molecule on a Ni surface, including reaction intermediates, activation barriers and chemisorbed H and F atoms.

In the paper, we consider the adsorption of a single HF molecule on a Ni(111) surface, employing DFT with the vdW-DF functional. For a more intuitive expression of the potential energy surface, it is beneficial to represent the six dimensions as molecular coordinates: x, y, z, r, θ and ϕ (see Paper D, Fig. 1 for the definition). Chemisorption is found to be exothermic with reaction paths over two different transition states, centered over an fcc or an hcp site. The transition states are acquired by a saddle point search using the DIMER algorithm.[210] Frequency calculations show that these transition states are first order, by yielding one imaginary frequency.

Fig. 4.4 shows the reaction energy versus the molecule in vacuum. The activation barrier is ca. 510 meV for both transition states. The impact angles (θ) of the transition states are 127.7° and 128.4°, which allows both atoms to efficiently chemisorb if the HF bond length (r) is elongated (see Fig. 4.4). Furthermore, there are physisorption minima of –181 meV at both hollow sites. Considering a molecule in the vacuum phase, the calculated zero-point energy amounts to 235 meV. This lowers the activation barriers to two surmountable values of ca. 275 meV. For comparison, in two DFT studies on the first chemisorption step of H_2O on Ni(111) and CH_4 on Ni(111), the activation barriers were calculated to 670 meV and 1010 meV, respectively.[211,212]

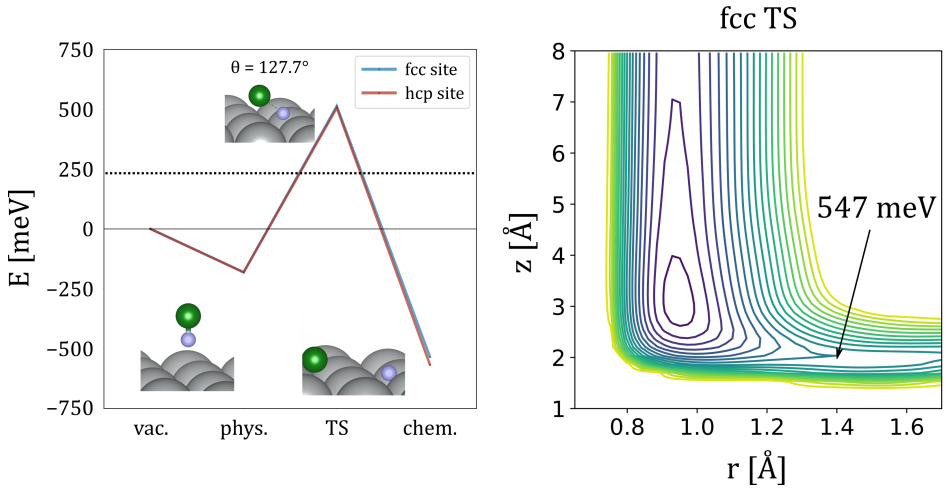

Figure 4.4: Left: Minimal energy path towards chemisorption of HF on Ni(111). The reference state is an HF molecule in vacuum (not drawn). The vibrational zero-point energy (235 meV) of HF in vacuum is depicted as a dashed line. Two energetically and structurally similar paths are found, where the molecule is situated over either an fcc or an hcp hollow site. Physisorption intermediates are found, with the H end of the molecule pointing towards the surface. Transition states are calculated with the DIMER method and show one imaginary vibrational frequency. Chemisorbed structures are characterized by H and F atoms adsorbed at hollow sites. Right: Potential energy surface of the r (H–F distance) and z (HF–surface distance) degrees of freedom. The remaining coordinates, u, v, θ and ϕ are kept at the values of the fcc transition state (depicted to the left). The potential energy surface is fitted using a neural network algorithm with around 65000 single point DFT calculations (vdW-DF functional) as input.

In addition to these reaction steps, the adsorption is modeled as a molecular beam experiment using *ab initio* molecular dynamics. With a kinetic energy of 2.0 eV and a vibrational zero-point energy 235 meV, 85 % of the trajectories lead to chemisorption. In the remaining trajectories, the molecule is scattered back from the surface towards the vacuum. The high probability for chemisorption is consistent with the low activation barrier above and the much larger provided kinetic plus vibrational energy. Through analysis of the trajectories at different points during the simulation, molecules approaching the surface with the center of mass (largely centered on F) close to a top site are more likely to scatter back, compared to the hollow sites, which reflects the more repulsive potential at the top site. If the molecule is repelled by the surface, *i.e.* if it starts moving back towards the vacuum, only impact angles (θ) close to the transition state

Furthermore, the data points from the trajectories are fed into a neural network algorithm in order to fit a six-dimensional potential energy surface for the adsorption

processes of HF on Ni(111). An example two-dimensional cut is shown in Fig. 4.4, where the fitted energy is plotted versus r and z (the HF–Ni surface distance). The remaining four dimensions are set according to the fcc site transition state (Fig. 4.4, left). After a physisorption minimum at $r \approx 0.95$ Å, $z \approx 3$ Å, elongation of the H–F bond increases the energy until $r \approx 1.4$ Å, after which the curve flattens, indicating a bond breaking. This matches the r and z parameters of the DIMER transition state very well (see the arrow in the plot). The fitted energy for the fcc transition state (547 meV) matches the DFT energy (514 meV) well. However, for the hcp transition state, although the structural parameters are well described, the fitted energy (506 meV) deviates more from the reference DFT calculation (617 meV) by a larger amount. Hence, the fit is considered to be semi-quantitatively correct.

To improve the quality of the fit, more calculation points are required. Since the neural network potential is built entirely on *ab initio* calculated data points, it is capable of describing the reactive events necessary for the chemisorption of HF, unlike classical force-field methods. For further studies involving a Ni(111)–liquid HF interface, a feasible calculation setup is to treat the Ni–HF degrees of freedom with neural network potentials, while using well established classical force fields for the HF–HF interactions,[213,214] since these do not involve bond breaking. This would enable affordable molecular dynamics simulations on larger supercells and longer simulation times, while allowing H–F bond breakages on Ni(111).

The work presented is the first reported quantum-chemical study on the Ni_xF_y film which occurs in electrochemical fluorination reaction in the Simons process. In the computational hydrogen electrode scheme, thermodynamical arguments were used to characterize the typical anodic peak in cyclovoltammetry experiments as the faradaic oxidation of a surface NiF_2 film, from Ni^{2+} to Ni^{3+}. The model employed is quite general, and may be use to calculate redox potentials of surface of other nickel fluorides, such as NiF_3 or Ni_2F_5, or even other metal fluorides, such as cobalt fluorides or copper fluorides. Furthermore, secondary effects on the surfaces from the HF solvent may, in future work, be included thermodynamically, where one might expect some degree of stabilization of unsaturated surface Ni centers (*e.g.* Ni^{2+}) by coordination of HF.

Due to the explicit treatment of electron transfers and atomistic surface structures, the capacitor model for the reaction is capable of describing also kinetic effects. Also this method is extendable to different surfaces of Ni, where a more detailed look into the fluorination of *e.g.* stepped Ni surfaces would be of interest. In addition, the effects of higher fluorine coverages on the HF or F^- adsorption on Ni are highly interesting for an explicit description of the low cell potential film formation and subsequent passivation of the Ni anode.

Future considerations for the topic involve the mechanism for the fluorination

reaction of organic molecules by the Ni_xF_y film. Sartori and Ignatiev, with coworkers, reported side product in Simons cells due to competing isomerization reactions, or only partial fluorination of the organic molecules.[21,26,27] The observations were explained by assumptions on the structure of the film. For instance, two reactive fluorinating nickel centers (Ni^{3+} or Ni^{4+}) in close proximity at the surface were assumed to enhance isomerization side reactions.[21] The fundamental parts in such model systems are a plausible representation of the Ni_xF_y surface structure, an organic molecule (possibly with a functional group) and an explicit, or possibly implicit, treatment of the HF solvent. Quantum-chemical methods could, in principle, suffice in the reaction modeling between the named chemical species. However, the limitations still lie at the uncertainty regarding the structure of the Ni_xF_y film. For this, I consider further studies on the Ni_xF_y film structure necessary.

Bibliography

[1] `https://www.merriam-webster.com/dictionary/fluorine`, Online; accessed 29-March-2020.

[2] Higelin, A. and Riedel, S., *High Oxidation States in Transition Metal Fluorides. In: Modern Synthesis and Reactivity of Fluorinated Compounds, Groult, H., Leroux, F. R. and Tressaud, A. Eds.*, Elsevier, Inc., London, 2017.

[3] Christe, K. O., *Chem. Commun.*, 2013, **49**, 4588–4590.

[4] O'Hagan, D., *Chem. Soc. Rev.*, 2008, **37**, 308–319.

[5] Groult, H.; Leroux, F. R. and Tressaud, A. E., *Modern Synthesis and Reactivity of Fluorinated Compounds*, Elsevier, Inc., London, 2017.

[6] Banks, R. E.; Smart, B. E. and Tatlow, J. C. E., *Organofluorine Chemistry: Principles and Commercial Applications*, Springer Science+Business Media, New York, 1994.

[7] Lemal, D. M., *J. Org. Chem.*, 2004, **69**, 1–11.

[8] Ignatiev, N. V., *Electrochemical Fluorination: A Powerful Tool for the Preparation of Organofluorine Compounds. In: Modern Synthesis and Reactivity of Fluorinated Compounds, Groult, H., Leroux, F. R. and Tressaud, A. Eds.*, Elsevier, Inc., London, 2017.

[9] Fowler, R. D.; Burford, W. B.; Hamilton, J. M.; Sweet, R. G.; Weber, C. E.; Kasper, J. S. and Litant, I., *Ind. Eng. Chem.*, 1947, **39**, 292–298.

[10] Simons, J. H., *J. Electrochem. Soc.*, 1949, **95**, 47–52.

[11] Simons, J. H.; Francis, H. T. and Hogg, J. A., *J. Electrochem. Soc.*, 1949, **95**, 53–55.

[12] Simons, J. H. and Harland, W. J., *J. Electrochem. Soc.*, 1949, **95**, 55–59.

[13] Simons, J. H.; Pearlson, W. H.; Brice, T. J.; Wilson, W. A. and Dresdner, R. D., *J. Electrochem. Soc.*, 1949, **95**, 59–64.

[14] Simons, J. H. and Dresdner, R. D., *J. Electrochem. Soc.*, 1949, **95**, 64–67.

[15] Abe, T., *J. Fluorine Chem.*, 2000, **105**, 181–183.

[16] Simons, J. H., *Fluorine Chemistry*, Vol. 1, Academic Press, New York, 1950.

[17] Gramstad, T. and Haszeldine, R. N., *J. Chem. Soc.*, 1956, pages 173–180.

[18] Dimitrov, A.; Rüdiger, S.; Ignatiev, N. V. and Datsenko, S., *J. Fluorine Chem.*, 1990, **5**0, 197–205.

[19] Gambaretto, G. P.; Napoli, M.; Conte, L.; Scipioni, A. and Armelli, R., *J. Fluorine Chem.*, 1985, **27**, 149–155.

[20] Sartori, P.; Ignatiev, N. and Datsenko, S., *J. Fluorine Chem.*, 1995, **75**, 157–161.

[21] Ignatiev, N. V.; Welz-Biermann, U.; Heider, U.; Kucheryna, A.; von Ahsen, S.; Habel, W.; Sartori, P. and Willner, H., *J. Fluorine Chem.*, 2003, **124**, 21–37.

[22] Chang, B.; Yanase, H.; Nakanishi, K. and Watanabe, N., *Electrochim. Acta*, 1971, **16**, 1179–1196.

[23] Watanabe, N., *J. Fluorine Chem.*, 1983, **22**, 205–230.

[24] Drakesmith, F. G. and Hughes, D. A., *J. Fluorine Chem.*, 1986, **32**, 103–134.

[25] Bartlett, N.; Chambers, R. D.; Roche, A. J.; Spink, R. C. H. and Chacón, L., *Chem. Commun.*, 1996, **9**, 1049–1050.

[26] Sartori, P.; Ignatiev, N. and Jüschke, R., *J. Fluorine Chem.*, 1997, **81**, 115–121.

[27] Sartori, P. and Ignatiev, N., *J. Fluorine Chem.*, 1998, **87**, 157–162.

[28] Koch, W. and Holthausen, M. C., *A Chemist's Guide to Density Functional Theory*, WILEY-VCH Verlag GmbH, Weinheim, Germany, 2nd ed., 2000.

[29] Nørskov, J. K.; Abild-Pederson, F.; Studt, F. and Bligaard, T., *Proc. Natl. Acad. Sci. U.S.A.*, 2011, **108**, 937–943.

[30] Liu, Z.-P. and Hu, P., *Top. Catal.*, 2004, **28**, 71–78.

[31] Catapan, R. C.; Oliveira, A. A. M.; Chen, Y. and Vlachos, D. G., *J. Phys. Chem. C*, 2012, **116**, 20281–20291.

[32] Mohsenzadeh, A.; Bolton, K. and Richards, T., *Surf. Sci.*, 2014, **627**, 1–10.

[33] Füchsel, G.; del Cueto, M.; Díaz, C. and Kroes, G.-J., *J. Phys. Chem. C*, 2016, **120**, 25760–25779.

[34] Costa, M. M. R.; Paixão, J. A.; De Almeida, M. J. M. and Andrade, L. C. R., *Acta Crystallogr. B*, 1993, **49**, 591–599.

[35] Žemva, B.; Lutar, K.; Chacóm, L.; Fele-Beuermann, M.; Allman, J.; Shen, C. and Bartlett, N., *J. Am. Chem. Soc.*, 1995, **117**, 10025–10034.

[36] Tramsek, M. and Žemva, B., *Acta Chim. Slov.*, 2002, **49**, 209–220.

[37] Verma, P. and Truhlar, D. G., *Theor. Chem. Acc.*, 2016, **135**, 182.

[38] Schrön, A.; Rödl, C. and Bechstedt, F., *Phys. Rev. B*, 2010, **82**, 165109.

[39] Gillen, R.; Clark, S. J. and Robertson, J., *Phys. Rev. B*, 2013, **87**, 125116.

[40] Logsdail, A. J.; Downing, C. A.; Catlow, C. R. A. and Sokol, A. A., *Chem. Phys. Lett.*, 2017, **690**, 47–53.

[41] Ferrari, A. M. and Pisani, C., *J. Chem. Phys.*, 2007, **174711**, 127.

[42] Patel, M.; Mallia, G.; Liborio, L. and Harrison, N. M., *Phys. Rev. B*, 2012, **86**, 045302.

[43] Shojaee, K.; Haynes, B. S. and Montoya, A., *Mater. Chem. Phys.*, 2015, **141-149**, 156.

[44] Kaawar, Z.; Müller, C. and Paulus, B., *Surf. Sci.*, 2017, **656**, 48–53.

[45] Schrödinger, E., *Phys. Rev.*, 1926, **28**, 1049–1070.

[46] Born, M. and Oppenheimer, R., *Ann. Phys.*, 1927, **84**, 457–484.

[47] Mulliken, R. S., *Phys. Rev.*, 1932, **41**, 49–71.

[48] Pauli, W., *Z. Phys.*, 1925, **31**, 765–783.

[49] Slater, J. C., *Phys. Rev.*, 1929, **34**, 1293–1322.

[50] Fock, V., *Z. Phys.*, 1930, **51**, 126–148.

[51] Slater, J. C., *Phys. Rev.*, 1951, **81**, 385–390.

[52] Roothaan, C. C. J., *Rev. Mod. Phys.*, 1951, **23**, 69–89.

[53] Hall, G. G., *Proc. R. Soc. Lond.*, 1951, **205**, 541.

[54] Jensen, F., *Introduction to Computational Chemistry*, John Wiley & Sons Ltd, Chichester, England, 2nd ed., 2007.

[55] Löwdin, P.-O., *Phys. Rev.*, 1955, **97**, 1509–1520.

[56] Szabo, A. and Ostlund, N. S., *Modern Quantum Chemistry: Introduction to Advanced Electronic Structure Theory*, Dover Publications, Inc. Mineola, New York, 1st ed., 1996.

[57] Møller, C. and Plesset, M. S., *Phys. Rev.*, 1934, **46**, 618–622.

[58] Bartlett, R. J., *Phys. Rev.*, 1989, **93**, 1697–1708.

[59] Sherrill, C. D. and Schaefer, H. F., *Adv. Quant. Chem.*, 1999, **34**, 143–269.

[60] Maschio, L.; Usvyat, D.; Manby, F. R.; Casassa, S.; Pisani, C. and Schütz, M., *Phys. Rev. B*, 2007, **76**, 075101.

[61] Marsman, M.; Grüneis, A.; Paier, J. and Kresse, G., *J. Chem. Phys.*, 2009, **130**, 184103.

[62] Thomas, L. H., *Proc. Camb. Phil. Soc.*, 1927, **23**, 542–548.

[63] Fermi, E., *Z. Phys.*, 1928, **48**, 73–79.

[64] Hohenberg, P. and Kohn, W., *Phys. Rev.*, 1964, **136**, B864.

[65] Kohn, W. and Sham, L. J., *Phys. Rev.*, 1965, **140**, A1133.

[66] Becke, A. D., *Phys. Rev. A*, 1988, **38**, 3098–3100.

[67] Lee, C.; W., Y. and Parr, R. G., *Phys. Rev. B*, 1988, **37**, 785–789.

[68] Becke, A. D., *J. Chem. Phys.*, 1993, **98**, 5648.

[69] Perdew, J. P.; Tao, J.; Staroverov, V. N. and Scuseria, G. E., *J. Chem. Phys.*, 2004, **120**, 6898.

[70] Perdew, J. P.; Burke, K. and Ernzerhof, M., *Phys. Rev. Lett.*, 1996, **77**, 3865.

[71] Tao, J.; Perdew, J. P.; Staroverov, V. N. and Scuseria, G. E., *Phys. Rev. Lett.*, 2003, **91**, 146401.

[72] Vosko, S. J.; Wilk, L. and Nusair, M., *Can. J. Phys.*, 1980, **58**, 1200.

[73] Sawatzky, G. A. and Allen, J. W., *Phys. Rev. Lett.*, 1984, **53**, 2339.

[74] Fernandez, V.; Vettier, C.; de Bergevin, F.; Giles, C. and Neubeck, W., *Phys. Rev. B*, 1998, **57**, 7870.

[75] Rohrbach, A.; Hafner, J. and Kresse, G., *Phys. Rev. B*, 2004, **69**, 075413.

[76] Boese, A. D. and Handy, N. C., *J. Chem. Phys.*, 2001, **114**, 5497.

[77] Perdew, J. P.; Chevary, J. A.; Vosko, S. H.; Jackson, K. A.; Pederson, M. R.; Singh, D. J. and Fiolhais, C., *Phys. Rev. B*, 1992, **46**, 6671.

[78] Wu, Z. and Cohen, R. E., *Phys. Rev. B*, 2006, **73**, 235116.

[79] Perdew, J. P., *Phys. Rev. B*, 1986, **33**, 8822.

[80] Perdew, J. P.; Ruzsinszky, A.; Csonka, G. I.; Vydrov, O. A.; Scuseria, G. E.; Constantin, L. A.; Zhou, X. and Burke, K., *Phys. Rev. Lett.*, 2008, **100**, 136406.

[81] Zhang, Y. and Yang, W., *Phys. Rev. Lett.*, 1998, **80**, 890.

[82] Hammer, B.; Hansen, L. B. and Nørskov, J. K., *Phys. Rev. B*, 1999, **59**, 7413.

[83] Staroverov, V. N.; Scuseria, G. E.; Tao, J. and Perdew, J. P., *Phys. Rev. B*, 2004, **69**, 075102.

[84] Scholl, D. S., *Applications of Density Functional Theory to Heterogeneous Catalysis, in: Chemical Modelling: Applications and Theory, ed. Hinchliffe, A.*, The Royal Society of Chemistry, Cambridge, UK, 2006.

[85] Sabbe, M. K.; Reyniers, M.-F. and Reuter, K., *Catal. Sci. Technol.*, 2012, **2**, 2010–2024.

[86] Adamo, C. and Barone, V., *J. Chem. Phys.*, 1999, **110**, 6158.

[87] Zheng, H. and Wagner, L. K., *Phys. Rev. Lett.*, 2015, **114**, 176401.

[88] Krukau, A. V.; Vydrov, O. A.; Izmaylov, A. R. and Scuseria, G. E., *J. Chem. Phys.*, 2006, **110**, 224106.

[89] Müller, C.; Usvyat, D. and Stoll, H., *Phys. Rev. B*, 2011, **8**3, 245136.

[90] Halo, M.; Casassa, S.; Maschio, L. and Pisani, C., *Chem. Phys. Lett.*, 2009, **4**67, 294–298.

[91] Erba, A.; Maschio, L.; Salustro, S. and Casassa, S., *J. Chem. Phys.*, 2011, **1**34, 074502.

[92] Ivlev, S. I.; Karttunen, A. J.; Hoelzel, M.; Conrad, M. and Kraus, F., *Chem. Eur. J.*, 2019, **2**5, 3310–3317.

[93] Mattsson, S.; Paulus, B.; Redeker, F. A.; Beckers, H.; Riedel, S. and Müller, C., *Chem. Eur. J.*, 2019, **2**5, 3318–3324.

[94] Geatches, D.; Rosbottom, I.; Marchese Robinson, R. L.; Byrne, P.; Hasnip, P.; Probert, M. I. J.; Jochym, D.; Maloney, A. and Roberts, K. J., *J. Chem. Phys.*, 2019, **1**51, 044106.

[95] Tereshchuk, P. and Da Silva, J. L. F., *J. Phys. Chem. C*, 2012, **1**16, 24695–24705.

[96] He, Y. B.; Jia, J. F. and Wu, H. S., *Appl. Surf. Sci.*, 2015, **3**27, 462–469.

[97] Christmann, K., *Introduction to Surface Physical Chemistry*, Steinkopff-Verlag, Heidelberg, Germany, 1991.

[98] Atkins, P. and de Paula, J., *Elements of Physical Chemistry*, W. H. Freeman and Company: New York, 5th ed., 2009.

[99] Eisenschitz, E. and London, F., *Z. Phys.*, 1930, **6**0, 491–527.

[100] Grimme, S., *J. Comput. Chem.*, 2006, **2**7, 1787–1799.

[101] Grimme, S.; Antony, J.; Ehrlich, S. and Krieg, H., *J. Chem. Phys.*, 2010, **1**32, 154104.

[102] Grimme, S.; Ehrlich, S. and Goerigk, L., *J. Comput. Chem.*, 2011, **3**2, 1456–1465.

[103] Johnson, E. R. and Becke, A. D., *J. Chem. Phys.*, 2006, **1**24, 174104.

[104] Reckien, W.; Janetzko, F.; Peintinger, M. F. and Bredow, T., *J. Comput. Chem.*, 2012, **3**3, 2023–2031.

[105] Hujo, W. and Grimme, S., *J. Chem. Theory Comput.*, 2011, **7**, 3866–3871.

[106] Goerigk, L., *A Comprehensive Overview of the DFT-D3 London-Dispersion Correction, in: Non-Covalent Interactions in Quantum Chemistry and Physics, eds. Otero de la Roza, A.; Dilabio, G. A.*, Elsevier Inc., Amsterdam, Netherlands, 2017.

[107] Sherkunov, Y., *Phys. Rev. A*, 2009, **7**9, 032101.

[108] Gohr, S.; Grimme, S.; Söhnel, T.; Paulus, B. and Schwerdtfeger, P., *J. Chem. Phys.*, 2013, **1**39, 174501.

[109] Schröder, E.; Cooper, V. R.; Berland, K.; Lundqvist, B. I.; Hyldgaard, P. and Thonhauser, T., *The vdW-DF Family of Nonlocal Exchange-Correlation Functionals, in: Non-Covalent Interactions in Quantum Chemistry and Physics, eds. Otero de la Roza, A.; Dilabio, G. A.*, Elsevier Inc., Amsterdam, Netherlands, 2017.

[110] Dion, M.; Rydberg, H.; Schröder, E.; Langreth, D. C. and Lundqvist, B. I., *Phys. Rev. Lett.*, 2004, **9**2, 246401.

[111] Berland, K.; Cooper, V. R.; Lee, K.; Schröder, E. Thonhauser, T.; Hyldgaard, P. and Lundqvist, B. I., *Rep. Prog. Phys.*, 2015, **7**8, 066501.

[112] Klimeš, J.; Bowler, D. R. and Michaelides, A., *J. Phys.: Condes. Matter*, 2010, **2**2, 022201.

[113] Reimers, J. R.; Li, M.; Wan, D.; Gould, T. and Ford, M. J., *Surface Adsorption, in: Non-Covalent Interactions in Quantum Chemistry and Physics, eds. Otero de la Roza, A.; Dilabio, G. A.*, Elsevier Inc., Amsterdam, Netherlands, 2017.

[114] Lebègue, S.; Harl, J.; Gould, T.; Ángyán, J. G.; Kresse, G. and Dobson, J. F., *Phys. Rev. Lett.*, 2010, **1**05, 196401.

[115] Laue, M., *Ann. Phys.*, 1913, **41**, 989–1002.

[116] Kittel, C., *Introduction to Solid State Physics*, John Wiley & Sons Ltd, Hoboken, NJ, United States, 8th ed., 2005.

[117] Bloch, F., *Z. Phys.*, 1928, **52**, 555–.

[118] de Broglie, L., *Found. Phys.*, 1970, **1**, 5–15.

[119] Heisenberg, W., *Z. Phys.*, 1927, **43**, 172–198.

[120] Monkhorst, H. J. and Pack, J. D., *Phys. Rev. B*, 1976, **13**, 5188–5192.

[121] Dirac, P. A. M., *Proc. R. Soc. Lond. A*, 1926, **112**, 661–677.

[122] Connelly, D. L.; Loomis, J. S. and Mapother, D. E., *Phys. Rev. B*, 1971, **3**, 924–934.

[123] Richards, P. L., *J. Appl. Phys.*, 1963, **34**, 1237–1238.

[124] Towler, M. D.; Zupan, A. and Causà, M., *Comput. Phys. Comm.*, 1996, **98**, 181–205.

[125] Corà, F.; Aldredsson, M.; Mallia, G.; Middlemiss, D. S.; Mackrodt, W. C.; Dovesi, R. and Orlando, R., *The Performance of Hybrid Density Functionals in Solid State Chemistry. In: Principles and Applications of Density Functional Theory in Inorganic Chemistry II, Kaltsoyannis, N. and McGrady, J. E. Eds.*, Vol. 113, Springer, Berlin, Germany, 2004.

[126] Dovesi, R.; Causà, M.; Orlando, R.; Roetti, C. and Saunders, V., *J. Chem. Phys.*, 1990, **92**, 7402–7411.

[127] Silvi, B.; Causà, M.; Dovesi, R. and Roetti, C., *Mol. Phys.*, 1989, **67**, 891–901.

[128] Aissing, G. and Monkhorst, H. J., *Int. J. Quantum Chem.*, 1992, **43**, 733–745.

[129] Kresse, G. and Joubert, D., *Phys. Rev. B*, 1999, **59**, 1758–1775.

[130] Enkovaara, J.; Rostgaard, C.; Mortensen, J. J.; Chen, J.; Dułak, M.; Ferrighi, L.; Gavnholt, J.; Glinsvad, C.; Haikola, V. and Hansen, H. A., *J. Phys. Condens. Matter*, 2010, **22**, 253202.

[131] Torrent, M.; Jollet, F.; Bottin, F.; Zérah, G. and Gonze, X., *Comput. Mater. Sci.*, 2008, **42**, 337–351.

[132] Blöchl, P. E., *Phys. Rev. B*, 1994, **50**, 17953–17979.

[133] Levy, M., *Phys. Rev. B*, 1996, **53**, 3764–3774.

[134] Hubbard, J., *Proc. R. Soc. Lond.*, 1963, **276**, 238–257.

[135] Bluhm, H.; Brückel, T.; Morgenstern, M.; von Plessen, G. and Stampfer, C., *Electrons in Solids*, Walter de Gruyter GmbH, Berlin, 2019.

[136] McKay, J. M. and Henrich, V. E., *Phys. Rev. Lett.*, 1984, **53**, 2343–2346.

[137] Zaanen, J.; Sawatzky, G. A. and Allen, J. W., *Phys. Rev. Lett.*, 1985, **55**, 418–421.

[138] Dudarev, S. L.; Botton, G. A.; Savrasov, S. Y.; Humphreys, C. J. and Sutton, A. P., *Phys. Rev. B*, 1998, **57**, 1505–1509.

[139] Liechtenstein, A. I.; Anisimov, V. I. and Zaanen, J., *Phys. Rev. B*, 1995, **52**, 5467–5471.

[140] Cococcioni, M., *The LDA+U Approach: A Simple Hubbard Correction for Correlated Ground States, in: Correlated Electrons: From Models to Materials, eds. Pavarini, E.; Koch, E.; Anders, F. and Jarrell, M.*, Forschungszentrum Jülich, Zentralbibliothek, Verlag, Jülich, Germany, 2012.

[141] Hu, Z. and Metiu, H., *J. Phys. Chem. C*, 2011, **115**, 5841–5845.

[142] Zhou, L.; Körmann, F.; Holec, D.; Bartosik, M.; Grabowski, B.; Neugebauer, J. and Mayrhofer, P. H., *Phys. Rev. B*, 2014, **90**, 184102.

[143] Loschen, C.; Carrasco, J.; Neyman, K. M. and Illas, F., *Phys. Rev. B*, 2007, **75**, 035115.

[144] Cococcioni, M. and de Gironcoli, S., *Phys. Rev. B*, 2005, **71**, 035105.

[145] Wollan, E. O.; Child, H. R.; Koehler, W. C. and Wilkinson, M. K., *Phys. Rev.*, 1958, **112**, 1132–1136.

[146] Nolting, W. and Ramakanth, A., *Quantum Theory of Magnetism*, Springer-Verlag Berlin Heidelberg, Germany, 2009.

[147] Odom, B.; Hanneke, D.; D'Urso, B. and Gabrielse, G., *Phys. Rev. Lett.*, 2006, **97**, 030801.

[148] Stoner, E. C., *J. Phys. Radium*, 1951, **12**, 372–388.

[149] Anderson, P. W., *Phys. Rev.*, 1950, **79**, 350–356.

[150] Goodenough, J. B., *Annu. Rev. Mater. Sci.*, 1998, **28**, 1–27.

[151] Kataoka, M., *J. Phys. Soc. Jpn.*, 2002, **71**, 172–174.

[152] Gehring, G. A. and Gehring, K. A., *Phys. Rev. B*, 1975, **38**, 1–89.

[153] Cairns, R. W. and Ott, E., *J. Am. Chem. Soc.*, 1933, **55**, 527–533.

[154] Babel, D. and Tressaud, A., *Crystal Chemistry of Fluorides. In: Inorganic Solid Fluorides, Chemistry and Physics, Hagenmuller, P. Ed.*, Academic Press, Orlando, Florida, 1985.

[155] Heisenberg, W., *Z. Phys.*, 1928, **49**, 619–636.

[156] Bader, R. F. W., *Acc. Chem. Res.*, 1985, **18**, 9–15.

[157] Schrön, A.; Rödl, C. and Bechstedt, F., *Phys. Rev. B*, 2010, **82**, 165109.

[158] Nabi, H. S.; Harrison, R. J. and Pentcheva, R., *Phys. Rev. B*, 2010, **81**, 214432.

[159] Toyoda, M.; Yamauchi, K. and Oguchi, T., *Phys. Rev. B*, 2013, **87**, 224430.

[160] Miller, W. H., *A Treatise on Crystallography*, J. & J. J. Deighton, London, 1839.

[161] Lin, H.; Li, L.; Zhao, M.; Huang, X.; Chen, X.; Li, G. and Yu, R., *J. Am. Chem. Soc.*, 2012, **134**, 8328–8331.

[162] Erdogan, R.; Ozbek, O. and Onal, I., *Surf. Sci.*, 2010, **604**, 1029–1033.

[163] Li, L.; Larsen, A. H.; Romero, N. A.; Morozov, V. A.; Glinsvad, C.; Abild-Pedersen, F.; Greeley, J.; Jacobsen, K. W. and Nørskov, J. K., *J. Phys. Chem. Lett.*, 2013, **4**, 222–226.

[164] Wang, X.-G.; Weiss, W.; Shaikhutdinov, S. K.; Ritter, M.; Petersen, M.; Wagner, F.; Schlögl, R. and Scheffler, , *Phys. Rev. Lett.*, 1998, **81**, 1038–1041.

[165] Batyrev, I.; Alavi, A. and Finnis, M. W., *Faraday Discuss.*, 1999, **114**, 33–43.

[166] Sherwood, D. and Dalby, P., *Modern Thermodynamics for Chemists and Biochemists*, Oxford University Press, UK, 2018.

[167] Raoult, F.-M., *C. R. Acad. Sci.*, 1886, **104**, 1430–1433.

[168] Witcherle, I. and Linek, J., *Antoine Vapor Pressure Constants of Pure Compounds*, Academia, Prague, Czechoslovakia, 1971.

[169] `https://webbook.nist.gov/cgi/cbook.cgi?ID=C7664393&Mask=1#Thermo-Gas`, Online; accessed 18-December-2019.

[170] Nernst, W., *Z. Phys. Chem.*, 1889, **4**, 129–181.

[171] Helmholtz, H., *Ann. Phys.*, 1853, **1**65, 211–233.

[172] Gouy, L. G., *Ann. Chim. Phys.*, 1903, **2**9, 145–241.

[173] Chapman, D. L., *Philos. Mag.*, 1913, **2**5, 475–481.

[174] Stern, O., *Z. Elektrochem.*, 1924, **3**0, 508–516.

[175] Bard, A. J. and Faulkner, L. R., *Electrochemical Methods. Fundamentals and Applications*, Vol. 2, John Wiley & Sons, Inc.: New York, 2001.

[176] Isse, A. A. and Gennaro, A., *J. Phys. Chem. B*, 2010, **1**14, 7894–7899.

[177] Nørskov, J. K.; Rossmeisl, J.; Logadottir, A.; Lindqvist, L.; Kitchin, J. R.; Bligaard, T. and Jónsson, H., *J. Phys. Chem. B*, 2004, **1**08, 17886–17892.

[178] `https://webbook.nist.gov/cgi/cbook.cgi?Name=h2&cTG=on`, Online; accessed 18-December-2019.

[179] Hammett, L. P. and Deyrup, A. J., *J. Am. Chem. Soc.*, 1932, **5**4, 2721–2739.

[180] Peterson, A. A.; Abild-Pedersen, F.; Studt, F.; Rossmeisl, J. and Nørskov, J. K., *Energy Environ. Sci.*, 2010, **3**, 1311–1315.

[181] Rossmeisl, J.; Nørskov, J. K.; Taylor, C. D.; Janik, M. J. and Neurock, M., *J. Phys. Chem. B*, 2006, **1**10, 21833–21839.

[182] Valdes, A.; Qu, Z. W.; Kroes, G.-J.; Rossmeisl, J. and Nørskov, J. K., *J. Phys. Chem. C*, 2008, **1**12, 9872.

[183] Gossenberger, F.; Roman, T. and Groß, A., *Electrochim. Acta*, 2016, **2**16, 152–159.

[184] Saravanan, K.; Basdogan, Y.; Dean, J. and Keith, J. A., *J. Mater. Chem. A*, 2017, **5**, 11756–11763.

[185] Rendón-Calle, A.; Builes, S. and Calle-Vallejo, F., *Curr. Opin. Electrochem.*, 2018, **9**, 158–165.

[186] Oberhofer, H., *Electrocatalysis Beyond the Computational Hydrogen Electrode, in: Handbook of Materials Modeling, eds. Andreoni, W.; Yip, S.*, Springer International Publishing AG, Basel, Switzerland, 2018.

[187] Hansen, W. N. and Hansen, G. J., *Phys. Rev. A*, 1987, **3**6, 1396–1402.

[188] Donald, W. A.; Leib, R. D.; O'Brien, J. T.; Bush, M. F. and Williams, E. R., *J. Am. Chem. Soc.*, 2008, **1**30, 3371–3381.

[189] Rossmeisl, J.; Skúlason, E.; Björketun, M. E.; Tripkovic, V. and Nørskov, J. K., *Chem. Phys. Lett.*, 2008, **4**66, 68–71.

[190] Holmberg, N. and Laasonen, K., *J. Phys. Chem. C*, 2015, **1**19, 16166–16178.

[191] Bruneval, F.; Crocombette, J.-P.; Gonze, X.; Dorado, B.; Torrent, M. and Jollet, F., *Phys. Rev. B*, 2014, **8**9, 045116.

[192] Chan, K. and Nørskov, J. K., *Chem. Phys. Lett.*, 2015, **6**, 2663–2668.

[193] Chan, K. and Nørskov, J. K., *Chem. Phys. Lett.*, 2016, **7**, 1686–1690.

[194] Björketun, M. E.; Zeng, Z.; Ahmed, R.; Tripkovic, V.; Thygesen, K. S. and Rossmeisl, J., *Chem. Phys. Lett.*, 2013, **5**55, 145–148.

[195] Lide, D. R., *Eectron Work Function of the Elements in CRC Handbook of Chemistry and Physics, Internet Version*, CRC Press, Boca Raton, FL„ 2005.

[196] Hepworth, M. A.; Jack, K. H.; Peacock, R. D. and Westland, G. J., *Acta Crystallogr.*, 1957, **10**, 63–69.

[197] Hector, A. L.; Hope, E. G.; Levason, W. and Weller, M. T., *Z. Anorg. Allg. Chem.*, 1998, **624**, 1982–1988.

[198] Tressaud, A.; Wintenberger, M.; Bartlett, N. and Hagenmuller, P., *C. R. Acad. Sci. Paris, Serie C*, 1976, **282**, 1069–1072.

[199] Hepworth, M. A. and Jack, K. H., *Acta Crystallogr.*, 1957, **10**, 345–351.

[200] Lide, D. R., Ed., *Standard Thermodynamic Properties of Chemical Substances in CRC Handbook of Chemistry and Physics, Internet Version*, CRC Press, Boca Raton, FL, 2005.

[201] Assowe, O.; Politano, O.; Vignal, V.; Arnoux, P.; Diawara, B.; Verners, O. and van Duin, A. C. T., *J. Phys. Chem. A*, 2012, **116**, 11796–11805.

[202] Björketun, M. E.; Zeng, Z.; Ahmed, R.; Tripkovic, V.; Thygesen, K. S. and Rossmeisl, J., *Chem. Phys. Lett.*, 2013, **555**, 145–148.

[203] Sakong, S.; Forster-Tonigold, K. and Groß, A., *J. Chem. Phys.*, 2016, **144**, 194701.

[204] Hackerman, N.; Snavely, E. S. and Fiel, L. D., *Corros. Sci.*, 1967, **7**, 39–50.

[205] Huesges, Z.; Müller, C.; Paulus, B.; Hough, C.; Harrison, N. and Kemnitz, E., *Surf. Sci.*, 2013, **609**, 73–77.

[206] Kaawar, Z. and Paulus, B., *AIP Conf. Proc.*, 2015, **1653**, 020051.

[207] Olalde-Velasco, P.; Jiménez-Mier, J.; Denlinger, J. D.; Hussain, Z. and Yang, W. L., *Phys. Rev. B*, 2011, **83**, 241102.

[208] Bailey, C. L.; Mukhopadhyay, S.; Wander, A.; Searle, B. G. and Harrison, N., *J. Phys. Chem. C*, 2009, **1**13, 4976–4983.

[209] Totir, G. G.; Chottiner, G. S.; Gross, C. L.; Childs, W. V. and Scherson, D. A., *J. Electrochem. Soc.*, 2000, **1**47, 4212–216.

[210] Henkelman, G. and Jónsson, H. A., *J. Chem. Phys.*, 1999, **111**, 7010.

[211] Jiang, B. and Guo, H., *Phys. Rev. Lett.*, 2015, **1**14, 166101.

[212] Nattino, F.; Migliorini, D.; Kroes, G. J.; Dombrowski, E.; High, E. A.; Killelea, D. R. and Utz, A. L., *J. Phys. Chem. Lett.*, 2016, **7**, 2402–2406.

[213] Izvekov, S. and Voth, G. A., *J. Phys. Chem. B*, 2005, **1**09, 6573–6586.

[214] Mazack, M. J. M. and Gao, J., *J. Chem. Phys.*, 2014, **1**40, 204501.

Acknowledgments

First and foremost, I would like to express the sincerest gratitude towards Beate Paulus, for her supervision, involvement in my work and inclusion into the working group (AG). Working with her means great opportunities to fulfill your own ideas, while maintaining excellent scientific guidance. I would also like to thank Beate Paulus for the identification of such a scientifically interesting and otherwise rich topic for my thesis.

I am also very grateful towards Sebastian Riedel for, first of all, being the second reviewer of this thesis, but also for introducing me to fluorine chemistry in general, as well as participating in helpful discussions on many scientific topics, which helped a lot in finding directions for this project.

Throughout my work in the AG Paulus, I also received great tutoring by Carsten Müller on a side project, but also including helping me out early with general quantum chemical questions. From Gernot Füchsel, I have also received excellent guidance, both theoretical and practical, on the topic of molecule-metal interfaces and *ab initio* molecular dynamics. His proficiency on the topic was a great factor contributing to the fourth publication in this work.

I would like to thank my experimental colleague, Gene Senges, with whom heated discussions about the Simons process were a driving force behind the project. Oftentimes, Helmut Beckers and Simon Steinhauer took part in the conversations, for which I am very happy. Moreover, I am delighted for conversations with Nikolai Ignatiev, who is behind very important experimental work on the Simons process.

I am very thankful towards the students who have worked with me throughout these years: Benjamin Schröder, Shreya Sinha, Deniz Meyer and Hana Zupan. Answering your questions regarding theory or methodologies certainly helped in my own understanding of many concepts. An addition, I would like to thank Andreas Achazi for first introducing me to DFT calculations and guiding me while getting into the topic.

Importantly, I want to express my gratitude for having worked with such friendly colleagues in the theoretical chemistry groups. I am happy to have shared office with Zeinab Kaawar and Yasmeen Qawasmeh, who both contributed to a warm working

environment. Further on, I was delighted to share office with Jingjing Shao, who always, along with sharing her positive spirit, would give excellent yoga advice. Others I would like to mention are Hannah Eyre, Simon Ghysbrecht and Tim Küllmey, all with whom I have become dear friends. I am also thankful due to the proofreading of paper manuscripts by Hannah Eyre; I certainly think, that this improved my usage of commas in English.

This work was made possible through the support of the German Research Foundation (DFG), as parts of the research training network GRK 1582, "Fluorine as a Key Element" (2016-2018) and collaborative research center SFB 1349, "Fluorine-Specific Interactions" (2019-2020). For this, I express my gratitude towards the DFG. Calculation time was generously granted for the supercomputer clusters at the High Performance Computing in Northern Germany (HLRN) facilities, as part of the project bec00154, "Modeling electrochemical fluorination using first principles". I would also like to thank the Central Computing Services of the Freie Universität Berlin (ZEDAT) for excellent day-to-day maintenance of computers and filesystems.

Finally, I would like to thank my family for their roles in the greater picture. You have always approached me with encouragement, but also offered leisure at times needed. A few other people have or have had a major positive influence on my life the last years. These people – (without specific order) Adriaan, Agnes, Celia, David, Emma, Johanna and Kevin – are all unique and amazing in their own way.